OPTIMAL ENERGY MANAGEMENT AND CONTROL OF MICROGRIDS IN MODERN ELECTRICAL POWER SYSTEMS

By

ANUSHKA MADUSHAN DISSANAYAKE RALALAGE

Bachelor of Science in Electrical and Electronic Engineering
University of Peradeniya
Peradeniya, Sri Lanka
2014

Submitted to the Faculty of the
Graduate College of the
Oklahoma State University
in partial fulfillment of
the requirements for
the Degree of
DOCTOR OF PHILOSOPHY
May, 2020

OPTIMAL ENERGY MANAGEMENT AND CONTROL OF MICROGRIDS IN MODERN ELECTRICAL POWER SYSTEMS

Dissertation Approved:

Dr. Nishantha C. Ekneligoda

Dissertation Adviser

Dr. Rama G. Ramakumar

Dr. Gary G. Yen

Dr. Rushikesh L. Kamalapurkar

ACKNOWLEDGEMENTS

I would like to express my sincere gratitude to Dr. Nishantha C. Ekneligoda for his constant support, guidance, and encouragement as my advisor throughout this study. Then, I would like to thank Dr. Rama G. Ramakumar, Dr. Gary G. Yen, and Dr. Rushikesh L. Kamalapurkar for serving on my committee. The comments and the guidance offered by the committee members are sincerely appreciated. Next, I would like to thank Dr. Jeffery Young, the department chair, Electrical and Computer Engineering and all the faculty and staff members for their support provided during my study period. Further, I would like to express my gratitude to Electrical and Computer Engineering department and Airplane Transporting System (ATS) for providing financial assistance for the study period. Last but not least, I wish to thank my parents and my family for their never-ending support and encouragement.

Acknowledgements reflect the views of the author and are not endorsed by committee members or Oklahoma State University.

Name: ANUSHKA MADUSHAN DISSANAYAKE RALALAGE

Date of Degree: MAY, 2020

Title of Study: OPTIMAL ENERGY MANAGEMENT AND CONTROL OF MICROGRIDS IN MODERN ELECTRICAL POWER SYSTEMS

Major Field: ELECTRICAL ENGINEERING

Abstract: Microgrids (MGs) are becoming more popular in modern electric power systems owing to their reliability, efficiency, and simplicity. The proportional-integral (PI) based droop control mechanism has been widely used in the MG control domain as the setpoint generator for the primary controller which has several drawbacks. In order to mitigate these issues, and to enhance the transient and steady-state operations in islanded MGs, advanced control and intelligent optimization methodologies are presented in this dissertation. First, to improve the existing PI-based droop relationship in DCMGs, a multi-objective optimization (MOO) based optimal droop coefficient computation method is proposed. Considering the system voltage regulation, system total loss minimization, and enhanced current sharing among the distributed generators (DGs), the Pareto optimal front is obtained using the Elitist non dominated sorting genetic algorithm (NSGA II). Then, a fuzzy membership function approach is introduced to extract the best compromise solution from the Pareto optimal front. The drawbacks of PI-based droop control cannot be entirely mitigated by tuning the droop gains. Hence, a droop free, approximate optimal feedback control strategy is proposed to optimally control DGs in islanded DCMGs. Further, to gain the fully optimal behavior, and to mitigate constant power load (CPL) instabilities, a decentralized optimal feedback control strategy is also introduced for the active loads (ALs) in the MG. In both algorithms, the approximate dynamic programming (ADP) method is employed to solve the constrained input infinite horizon optimal control problem by successive approximation of the value function via a linear in the parameter (LIP) neural network (NN). The NN weights are updated online by a concurrent reinforcement learning (RL) based tuning algorithm, and the convergence of the unknown weights to a neighborhood of the optimal weights is guaranteed without the persistence of excitation (PE). Finally, a local optimal control strategy is presented to path optimization of islanded ACMGs to enhance the transient operations while mitigating the voltage and frequency deviations caused by the traditional droop control. Optimal state and control transient trajectories in the d-q reference frame are obtained by Pontryagin's minimum principle which drives each DG from a given initial condition to their steady-state manifold. Both simulation and experimental results are presented to validate the concepts.

TABLE OF CONTENTS

Chapter Page

Chapter Page

LIST OF TABLES

LIST OF FIGURES

LIST OF ABBREVIATIONS

AC	Alternating Current
ADP	Adaptive/Approximate Dynamic Programming
AL	Active Load
CPL	Constant Power Load
DC	Direct Current
DER	Distributed Energy Resource
DG	Distributed Generator
LIP	Linear in the Parameter
LS	Least Square
MG	Microgrid
MOEA	Multi-Objective Evolutionary Algorithm
MOO	Multi-Objective Optimization
NN	Neural Network
NSGA II	Elitist Non Dominated Sorting Genetic Algorithm
PE	Persistence of Excitation
PEI	Power Electronic Interface
PI	Proportional-Integral
RL	Reinforcement Learning
s.s	Steady-State

CHAPTER I

INTRODUCTION

1.1 Small Scale Power Systems and Microgrids

With the development of technological and conceptual arenas in power engineering, smart grids have become an exciting part of modern electric power systems [1, 2]. The integration of small scale power systems (SSPS) in these smart grids carries fascinating features in terms of power system design and controls [3–5]. As a subcategory of SSPS, microgrids (MGs) are equipped with its own premium, reliable and flexible power system operations rather than in the conventional large scale macro power systems [6–9]. Distributed generation, decentralized control, and high penetration of renewable energy are some significant aspects that can be recognized in these MGs [10–12].

The traditional macro or large scale power system is a combination of large, high inertial generators and bulky loads connected through long transmission lines [13,14]. It is a centralized power system architecture that has a small number of power injections, high maintenance cost, and complex transmission network [13]. Due to its size and centralized control, load balancing, voltage, and frequency regulation are difficult to achieve [13,14]. Further, the large thermal generation units produce air pollutants that make fatal environmental hazards. The emerging issues such as increasing demand, limitations of centralized power system planning, lack of high reliability, limited power quality urge the need of decentralized, small scale power systems such as MGs [13, 15, 16].

The MG concept was initially introduced in [17] as a methodology to integrate

distributed energy resources (DERs) along with the architecture, control and protection and energy management of the system. It also discussed the satisfaction of customer needs such as, enhance local reliability, reduce feeder losses, support local voltages, provide increased efficiency through use waste heat, voltage sag correction or provide uninterruptible power supply functions. There exist different definitions for the MG and the U.S Department of Energy defines the MG as *"a group of interconnected loads and distributed energy resources within clearly defined electrical boundaries that act as a single controllable entity with respect to the grid. A microgrid can connect and disconnect from the grid to enable it to operate in both grid-connected or island-mode"* [18]. Simply, a MG is a group of DGs, and energy storage systems (ESSs) collectively operate to supply energy demand to the customers reliably and efficiently even without the aid of the main grid [19]. As stated, one of the main aspects of MGs is the integration of distributed generators (DGs) or DERs. A definition of DG resources is given as, *"Distributed resources are demand and supply-side resources that can be deployed throughout an electric distribution system (as distinguished from the transmission system) to meet the energy and reliability needs of the customers served by that system. Distributed resources can be installed on either the customer side or the utility side of the meter"* [20].

The MGs can be classified into different sections according to their number of phases, voltage level, application type, system structure, control structure, and connection method of DGs [13, 14]. Table 1.1 summarized the main classes of MGs.

Table 1.1: Classes of Microgrids.

Type	MG Class
Phases	Three-phase, Single-phase
Voltage level	Medium voltage (1-35 kV), Low voltage (below 1 kV)
Voltage type	DCMGs, ACMGs, Hybrid DC/AC MGs
Application type	Utility MGs, Commercial, Industrial or Residential MGs, Military MGs
Control	Centralized, Decentralized, Distributed
DG connection	Electronically coupled, Conventionally coupled.

There are numerous advantages of MGs over the traditional macro power grids. Some of the advantages are listed below [13, 14, 18].

- Improve the reliability and make the grid more resilient by islanding from the main grid during any fault or outage.

- Effective energy supply for critical loads even under main grid failures.
- Provide local support for efficient, low-cost, and clean energy.
- Reduce losses by locating generation near demand.
- Reduce grid congestion and peak loads.
- Demand-side management and customer involvement in electricity generation.
- Avoid the expensive and inefficient long-distance transmission of power.

However, the MGs have many disadvantages too. Some of these drawbacks and challenges are discussed in the subsequent sections.

1.2 Motivation

Even though MGs carry fascinating features over the large scale power systems, integration of DG units in MGs introduces a number of operational challenges in terms of control and protection [13, 19, 21]. Some of these can be summarized as [19],

- Stability issues in regular operation and transition between modes of operation.
- Low inertia and spinning reserve.
- Control challenges such as power balance, frequency and voltage regulation.
- Bidirectional power flows and reverse power problems.
- Modeling issues due to variety of loads and distribution line properties.
- Communication problems in coordination among DG units.
- Uncertainty of load profiles and system parameters.

The simplified structure of an islanded MG is shown in Figure 1.1. Isolation switch decouples the physical connection between the MG and the main grid. A salient feature of a MG is most of the sources are renewable such as solar, wind, geothermal, battery energy storage, etc. Both sources and loads are distributed across the MG, and they are connected

to a common bus through a power electronic interface (PEI). This type of MG is called a parallel-connected bus system since sources and loads are connected in parallel to the common bus. There is another type of MGs called meshed MGs [22]. In the meshed MGs, the common bus is absent and each active component has its own bus interconnected to other buses through distribution lines. Sources in MGs are referred to as DGs which are typically renewable sources followed by PEI. The PEI plays a significant role in the MG control as it is responsible for the behavior of the active component connected to it. The PEI can be any isolated or non-isolated converter such as buck, boost, buck-boost, flyback, VSI, matrix converter, dual active bridge, rectifiers, .etc. Control of the MG implies control of these PEIs individually or collectively.

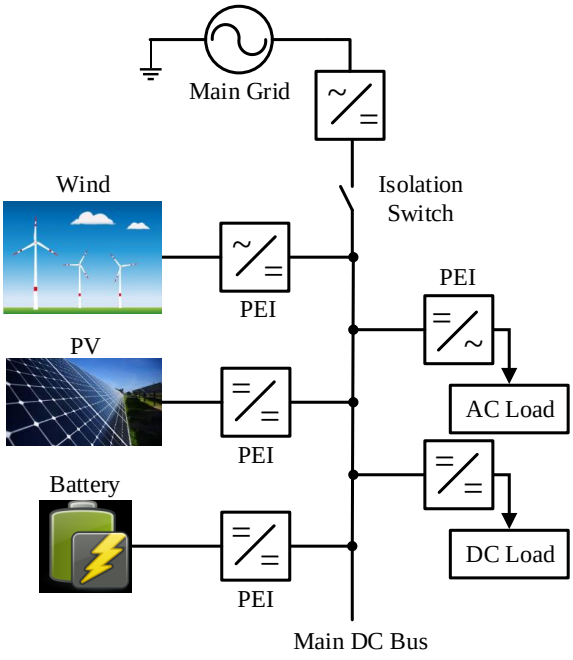

Figure 1.1: Schematic structure of a simplified islanded DCMG. © [2020] IEEE.

Since all the generation sources and loads are directly connected to the MG through a PEI, there is no inertial element directly connected to the system. Moreover, renewable energy sources and small scale power generation units dominate in these systems, low spinning reserve, generation inertia, and damping exist in contrast to the large scale power systems [3, 11]. These issues make the MG a low inertial dynamical system which is difficult to control and prone to instabilities. Therefore, new modeling tools and control algorithms are required

to analyze and control these future power systems. This dissertation mainly focuses on the optimization, control, and stability issues in the islanded MGs and methodologies to overcome them. Control and optimization of MGs in both centralized and decentralized domains are widely discussed in recent times [11, 23]. Among the MG control methods which have been proposed recently, the most prominent primary control methodology is the proportional-integral (PI) controller based droop control [24, 25]. Even though the PI controller is the most simple and convenient algorithm, it has poor transient performances [26], sensitivity to controller gains, and sluggish response to sudden disturbances [27]. Further, the droop mechanism suffers from high load-dependent voltage deviations, poor load sharing, and circulating current issues [28]. Therefore, advanced control mechanisms and modifications are required to replace PI loops and droop control in MGs to operate active resources efficiently.

In any type of a MG, the control of DGs is primarily done by the droop control [25]. In the DC droop control, the load sharing is achieved by properly varying the DG output voltage according to the measured output current [25]. The droop relationship comprises two constant droop coefficients, namely the virtual resistance and the output voltage reference at no load [25]. In AC droop control, DG output voltage and frequency are adjusted by the measured active and reactive power respectively [25, 29]. Here, droop relationships are characterized by the parameters called active and reactive power droop coefficients, nominal frequency, and voltage set point [25, 29]. Optimization of these droop coefficients to gain desired characteristics is an elegant method to improve the traditional droop mechanism. The application of various techniques to compute optimal droop coefficients can be found in the literature [30–37].

In most cases, optimal droop coefficient computation requires to solve several conflicting objectives. When there is more than one objective to satisfy, a single-objective optimization problem becomes a multi-objective optimization (MOO) problem. Most of the existing approaches mentioned above use the weighted sum approach to convert multi-objective to a single objective. Improving only one objective would degrade the quality of the other objectives due to their conflicting nature. In order to obtain the best results, this requires the knowledge of optimum weighting factors which are generally unknown. Further, a small change in weights may result in significant changes in the objective vectors, and significantly different weights may produce nearly similar objective vectors [38]. Moreover, weighted sum

approaches generate a single solution that does not provide flexibility to the decision-maker to select a compromise solution out of a pool of equally good solutions. Hence, the best way to attack a MOO problem is obtaining the corresponding Pareto optimal front [39] by simultaneous minimization of the objectives and then extracting a compromise solution as shown in this dissertation.

The drawbacks of PI-based droop control cannot be completely mitigated by merely optimizing the droop gains. Therefore, improvements to the conventional droop relationship are achieved by introducing novel control algorithms and appending secondary control mechanisms to compensate for the errors introduced by the primary controller. In order to enhance the load current sharing accuracy and to restore the local DC output voltage of droop based DCMGs, a low-bandwidth communication based distributed control method is proposed in [40]. Further, to achieve the same goals, an adaptive droop based distributed secondary controller is proposed in [41] for DCMGs with cooperative voltage and the current regulators. Moreover, the introduction of a robust adaptive control mechanism to adjust droop characteristics to maintain proper current sharing and bus voltage stability of DCMGs can be found in [42]. An improved secondary control methodology for DCMGs under fast-changing load current conditions is proposed in [43] to remove the DC voltage deviation and to improve the current sharing accuracy of the conventional droop method through voltage shifting and slope adjusting approaches. The main limitations of the alternative droop mechanisms are, many of these algorithms require offline tuning, communication among the other DGs in the MG and the dependency on the primary level control actions. Moreover, optimal control, model predictive control (MPC), multi-agent distributed control and game theoretic based control have introduced to control DGs in MGs to overcome the issues related to PI-based droop control [3, 11, 44, 45]. Besides, reinforcement learning (RL) inspired various adaptive or approximate dynamic programming (ADP) methods have been developed to solve optimal control problems in MG control domain [46–51]. The main limitation of most of the proposed ADP based feedback optimal control methods is that those require persistence of excitation (PE) condition to guarantee the parameter convergence [52]. Usually, the PE condition is satisfied by adding a small probing noise to the control input [53, 54]. Since there is no exact information on the required amount of noise power and the number of frequencies to guarantee PE, adding noise is always problematic. Moreover, injecting unnecessary noise

to the control input can make the whole system unstable and it is uncertain to know when it is sufficient to remove the probing signal [55]. Specially, in DCMGs, the control input is the duty cycle which is bounded between zero and one and hence, even adding a small noise to the duty cycle can make undesirable large variations in output voltage and current. Motivated by these facts, an approximate optimal feedback control method is proposed in this dissertation which eliminates the aforementioned constraints. The controller discussed here is an online, nonlinear feedback controller, which does not require any offline training. Hence, the proposed controller is very suitable for efficiently control DGs in DCMGs.

Nonlinear load profiles such as constant power loads (CPLs) often introduce instabilities to the power system due to their negative impedance characteristics, lack of damping and generation inertia [56–58]. Mitigation of CPL instabilities has been addressed in the literature to some extent [56, 57, 59, 60]. Among them, hardware-oriented methods focus on the addition of resistive loads, the inclusion of filters, load shedding, and placement of energy storage devices [56, 61]. However, these approaches are costly, require more space, and lossy which make them neither efficient nor effective. In contrast, control-oriented methodologies have been developed such as linear controllers [62], boundary controllers [63], game-theoretic controllers [3, 51], and sliding mode controllers [64, 65]. The power buffer is an effective method of mitigating instabilities caused by nonlinear load profiles, which has been introduced in [66] and discussed in [3, 51, 67–69]. The main drawback of all the existing power buffer approaches is they either provide open-loop numerical solutions or require communication among neighboring active loads. Motivated by the lack of decentralized feedback optimal stabilization control approaches to optimally control active loads such as power buffers, this dissertation introduces a novel control algorithm inspired by the ADP approach.

Transient optimization of MGs and parallel inverter systems has been discussed in the literature [32, 33, 70, 71]. However, most of the approaches assume the small-signal model of the system which makes the controller vulnerable to large-signal disturbances. Even though a transient improvement is considered in the aforementioned approaches, most of them do not focus on the optimum transient response or the path optimization of the individual DGs. Generation of optimum control and state trajectories that drive the system from a given initial condition to the desired steady-state equilibrium is beneficial in MG control and it has not been thoroughly addressed in the ACMGs domain yet. Therefore, a local optimal

control approach is introduced in this dissertation to transient path optimization of the individual inverters in an islanded ACMG. In the proposed local optimal control approach, each individual DG attempts to minimize its own dynamic cost by maneuvering their local control inputs. In this modeling, the optimal trajectories of the control inputs which minimize a performance index are generated in the d-q reference frame which fulfills the state of the art of d-q reference frame local optimal control in ACMGs.

1.3 Proposed Approaches and Contributions

The overall objectives of the proposed approaches are, to enhance the performances of the existing droop control, to mitigate the drawbacks of traditional PI-based droop control by introducing droop free optimal control approaches, to introduce advanced control architecture to control active loads in MGs. More stable and efficient transient and steady-state MG operations are the primary outcomes of the proposed concepts in this dissertation.

1.3.1 Multi-Objective Optimization of Droop Controlled Distributed Generators in Islanded DC Microgrids

The autonomous control of DCMG is primarily based on the droop control [25]. Typically, the droop coefficients of each DG are fixed and assigned based on their capacity which leads to poor current sharing and voltage regulation. Recognizing the advantages and superior performances of the nature-inspired MOO techniques, this dissertation presents a MOO based intelligent computation approach to derive the optimal droop coefficients for DGs in an islanded MG. The proposed method takes into consideration not only the capacities of the DGs, but also the system voltage regulation, system total loss minimization and enhanced current sharing among the DGs. The Pareto optimal front of the constructed MOO problem is obtained using the Elitist non dominated sorting genetic algorithm (NSGA II) [72]. The best compromise solution is extracted from the generated Pareto optimal front by employing a fuzzy membership function approach. Moreover, a state feedback linearization based controller is introduced to facilitates the control actions to experimentally validate the effectiveness and the applicability of the generated optimal droop relationships. The proposed approach was tested with a parallel-connected DC 9 bus system, IEEE 30 bus system and experimentally validated on a five bus system.

1.3.2 Approximate Optimal Feedback Control of Islanded DC Microgrids

There are two contributions to this section.

1. Droop Free Optimal Feedback Control of DGs in Islanded DC Microgrids.

2. Decentralized Optimal Stabilization of Active Loads in Islanded DC Microgrids.

As an alternative to the traditional PI-based droop control, this dissertation introduces a droop free, approximate optimal feedback control strategy to optimally control DGs in islanded DCMGs. Each DG is modeled as a control affine dynamical system and constrained input of each DG is designed to minimize the infinite horizon cost. Further, this dissertation also proposes a decentralized, online optimal feedback control strategy to optimally stabilize active loads in the DCMG. Each active load is modeled as a control affine dynamical system with an interconnected coupling term in the energy and admittance domain [73]. Then the decentralized, constrained input of each active load is obtained online in the feedback form to minimize the infinite horizon cost. In both cases, the ADP [54] method is employed to solve the infinite horizon optimal control problem by successive approximation of the value function via a LIP NN. The NN weights are updated online by a RL based tuning algorithm and the convergence of the unknown wights to a neighborhood of the optimal weights is guaranteed without the PE. Both simulation and experimental results are presented to demonstrate the effectiveness and applicability of the proposed concept.

1.3.3 Transient Optimization of Islanded AC Microgrids

In order to enhance the transient operations in islanded ACMGs, this dissertation presents a transient path optimization of a parallel-connected inverter-based DG system in an islanded ACMG. Optimal state and control transient trajectories are obtained which drive each DG from a given initial condition to their desired steady-state manifold. This transient trajectory optimization is an offline process that generates the open loop, local optimal control signals of the inverters. To generate the optimal state and control transient trajectories, Pontryagin's minimum principle is employed. The dynamic model of each DG, MG network and the optimum trajectories are generated in the d-q reference frame. An example microgrid system with three inverters was used to demonstrate the effectiveness and the performance of the proposed concept.

CHAPTER II

REVIEW OF LITERATURE

2.1 Control of Microgrids

A MG comprises DGs which supply the energy demand and loads who consume this energy. Both the sources and loads are treated as active components in a MG which can be controlled to have desired operations. The main control variables in a MG are voltage, current, frequency, active and reactive power. There are two modes of operations in MGs namely the grid-connected mode and the islanded mode. In each mode of operation, the control objectives are slightly different. In the grid-connected mode of operation, the MG frequency and the voltage at the point of common coupling are dominated by the main grid. Hence the main objective of the MG controllers in this mode is active and reactive power control of the DGs and demand-side management [14, 19]. In the islanded mode of operation, the MG is disconnected from the main grid and thus operates independently. Therefore, DGs must control the system voltage and frequency by themselves while balancing the energy supply and demand which is more challenging than the grid-connected mode [14, 19]. Thus, the main control objectives in the islanded mode are [74],

- System voltage and frequency regulation.
- Power balancing between supply and demand.
- Maintaining acceptable power quality.
- Communication among the other MG component to collectively achieve the objectives.

In the literature, different control architectures have been introduced to control MGs in both modes of operation. The control objectives such as voltage and frequency control, active and reactive power control can be categorized under centralized, decentralized and distributed control. Main control categories are discussed in the next subsections.

2.1.1 Hierarchical Control

Hierarchical control is the widely discussed control architecture in the MG domain [9,25,75,76]. There are three main levels in the hierarchical control which are primary control, secondary control, and tertiary control. The main functions of each level are summarized below.

1. Level 1 (primary control): Controls of this level are based on local measurements without any communication. This level features the fastest response among all the other levels. Objectives include islanding detection, frequency control, output voltage, and current control and power-sharing control. The droop based control methods are often utilized at this level. Any nonlinear, linear, or optimal controls can be employed at this level to achieve the control goals.

2. Level 2 (secondary control): This level ensures that the electrical quantities in the MG are within the required values such as the voltage and frequency. It corrects whatever the deviations caused by the primary level and try to keep the electrical variables near the nominal values. Moreover, it can include the mechanism to seamlessly disconnect or reconnect the MG from the main grid.

3. Level 3 (tertiary control): This level responsible for the economic and high-level energy management operations among multiple MGs and the main grid. Objectives of this level include coordination of operations of multiple MGs which interact with each other, provide reliable communication and supply requirements to or from the main grid to voltage support, frequency regulation and energy exchange.

2.1.2 Centralized Control

The centralized control approach is suitable for the smaller size MGs where the owners of DGs and loads have common goals and seek cooperation to meet their objectives [14]. A

high-speed communication link carries the state variable information from component level sensors to the MG central controller (MGCC) [14]. The MGCC processes the information and produces the decisions (control actions or setpoints) to the local controllers of each active component via the communication link. Centrally controlled MGs are relatively easier to handle since a single operator decides the entire operation of the system. However, this method is not reliable since a failure of the MGCC can cause shut down of the entire MG. Applications of centralized controllers in MGs can be found in [77–81].

2.1.3 Decentralized Control

The decentralized control approach takes decisions at the component level. It uses locally available measurements with a predefined control algorithm to make control decisions. In MG literature this method usually referred to as the autonomous control [14, 19]. The decentralized control is suitable for the complex MG networks with a large number of DGs and when active components have different goals. In such a network, the centralized control structure would fail since it requires high data handling capacity and processing power. The decentralized control architecture is more flexible and reliable [24]. However, it can produce multiple frequent failures in local controllers and also challenging to achieve globally optimal behavior. The decentralized control in MGs can be found in [82–87].

2.1.4 Distributed Control

The distributed control approach can be treated as an extended version of the decentralized control. In this architecture, local controllers of each DG communicate with its neighbors via a low bandwidth communication channel to achieve goals collectively [24]. Under this method, MGs are modeled as multi-agent systems (MAS) and seek for cooperation among the neighbors to control the entire MG by dividing a large problem into multiple subproblems. Consensus-based controls are the most popular algorithms used in the MG control domain under this category. Communication delays and failures can cause issues in this control approach. The application of distributed control in MGs can be found in [44, 88–91].

2.2 Optimization of Microgrids

To gain maximum efficiency from the MG controllers, operational algorithms and parameters should be optimized. Operation cost minimization, peak power reduction, voltage and frequency regulation, air pollutant and emission minimization, active and reactive power loss minimization, reliability and customer satisfaction maximization are some of the objectives that can be achieved by tuning the MG parameters and optimizing the control algorithms. Because of the superior problem-solving behavior, population-based heuristic optimization algorithms are taken as the main focus in this dissertation.

Modern heuristic optimization approaches together with the MOO techniques are widely applied in both traditional and modern power system applications [92]. The most common applications are the power system planning, load forecasting, fault detection, power-system controls, reactive power compensation, voltage control, economic dispatch and optimal power flow [92]. Among these typical applications, the most attractive form is the economic power dispatch problem and the associated optimal power flow (OPF). Economic dispatch is the process of finding out the optimal active power generations of each generator which minimizes the total fuel cost of the system. This MOO problem is widely addressed in the literature using different intelligent MOO approaches. In [93], the multi-objective evolutionary algorithm (MOEA) is developed to solve the economic dispatch problem together with the emission minimization of atmospheric pollutants. Here the authors have solved the problem using three different approaches and results are compared. Particle swarm optimization (PSO) based MOO technique is applied in [94] to solve the same two objective active power scheduling problem and results are compared with other MOEA approaches. In both of the above methods, the best compromise solution is obtained based on the fuzzy set theory and the optimal power flow solution is obtained for several IEEE bus systems. The application of differential evolution to the OPF problem can be found in [95] and [96]. In [95], generator operating cost minimization and total transmission line loss minimization are considered. On the other hand, in [96], both the active power dispatch and reactive power dispatch problems are addressed considering the emission factors. An improved PSO algorithm is applied in [97] to solve the OPF while considering the minimization of operating cost, emission, system losses and maximization of the voltage stability index.

Intelligent MOO techniques have been widely applied in modern MG system applications [98–106]. In order to obtain the optimal location and operations of DGs, Pareto frontier differential evolution algorithm based MOO technique is developed in [98]. The NSGA II MOO-based stochastic framework for the day ahead scheduling of MG energy storage systems is presented in [99] to minimize the expected operation cost and the expected load curtailment cost. The MOGA is utilized in [100] to simultaneously maximize the power availability and minimize the generated cost of a hybrid DG system based on a techno-economic approach. The differential evolution MOO for a DC MG is proposed in [101]. In this approach, objectives are considered to simultaneously minimize operation and maintenance cost, and loss of power supply. The chaotic binary PSO is applied in [102] to minimize the total economic cost and network loss of MGs. Applications of MOO in droop based MGs can be found in [103–106]. An optimal configuration for droop controlled islanded MG systems is developed in [103] based on NSGA II. In this approach, optimization considers three conflicting objectives primarily consisting of fuel cost minimization, loadability maximization and switching operation minimization of islanded MGs. Optimal operations in droop based islanded MGs have been obtained in [104] employing the multi-objective antlion optimizer algorithm. Total generation cost, total emission, and loadability factor are considered as conflicting objectives. Further, stochastic modeling is utilized to deal with the uncertainties in load demand and renewable generation. A novel probabilistic load flow algorithm based on the cumulant method is introduced in [105] to analyze the operating state of a decentralized droop controlled islanded MGs under uncertain environments. In this modeling, a MO coordinated planning model of active and reactive power resources is proposed to control the annual comprehensive cost and the operating risk. Moreover, NSGA-II MOO is utilized to solve the MO planning model. An optimal power dispatch strategy is proposed in [106] for droop based AC–DC hybrid MGs under load and generation uncertainties. In order to simultaneously minimize the cost and emission in MGs, this approach considers expected operating cost and the expected emission of the DGs as conflicting objectives. Further, the optimal solution is obtained by employing a technique which consists of PSO and fuzzy max-min strategies.

Improvement in the traditional droop based MG control can be attained by optimizing the droop coefficients. The optimal droop coefficient computation is an elegant method to improve the traditional droop mechanism. Intelligent optimization techniques have been

widely applied to obtain the optimal droop coefficients [30–37]. An optimal droop coefficient computation method is introduced in [30] based on the fuzzy membership functions and particle swarm optimization (PSO). In this formulation, operating cost minimization and emission minimization of MGs are carried out considering the heat demand, load demand and generation uncertainties. In order to obtain the optimum dynamic response of parallel-connected DGs, an optimum droop gain setting calculation method is proposed in [31] based on the differential evolution global search technique. Considering the small-signal model of the droop based MG, optimum droop and PI controller gain computation method is proposed in [32]. In this algorithm, to minimize the deviation between the instantaneous power and the nominal output power of the inverter during the switching between the grid-connected and the islanded modes, a genetic algorithm-based technique is employed. Application of the particle swarm optimization technique to tune the PI controller gains and the droop gains of the droop based MG can be found in [33] and [34]. Objective functions in [33] are proposed to minimize the error in the measured power and to enhance the damping characteristics in each mode of operation. In [34], the performance index comprises of the active and reactive power errors and the voltage and frequency deviations from their nominal values. The PSO based optimum droop parameter calculation methodology for DCMGs is developed in [35]. In this approach, a single cost function is formulated as a summation of the current sharing errors and the voltage degradations occurring at various loading conditions. Construction of nonlinear droop relationships to optimize operations in ACMGs can be found in [36]. In this modeling, the PSO is employed to obtain optimum nonlinear droop relationships that minimize the operating cost of the MG and share the reactive power effectively among the sources. In order to have higher efficiency and lower energy losses in DCMGs, [37] is proposed a tertiary control level to compute the droop gains which provide the global efficiency optimum. Here, the genetic algorithm is applied to solve the optimization problem.

2.3 Multi Objective Optimization Methods

The topic of MOO has been explored extensively during the past few decades. When there is more than one objective to satisfy, a single-objective optimization problem becomes a MOO problem. In contrast to the single optimization problem, in MOO we are interested in several extreme values that are all equally good.

MOO techniques can be broadly divided into two sections, which are the classical methods and intelligent methods [39, 92]. Classical methods use the traditional optimization techniques where intelligent methods use bio or nature-inspired algorithms such as evolutionary algorithms (EAs) [39] and swarm intelligent based approaches [107]. The classical methods further classified into four classes which are no-preference methods, posteriori methods, a priori methods, and interactive methods [108]. Under no-preference methods, classical MOO techniques such as multi-objective proximal bundle method, method of the global criterion can be identified [108]. Examples for the posteriori methods are the weighting method, ϵ constraint method, method of weighted metrics and achievement scalarizing function approach [108]. The techniques such as value function method, Lexicographic ordering and goal programming can be classified under a priori methods [108]. Few of the interactive methods are interactive surrogate worth trade-off method, Geoffrion-Dyer-Feinberg method, sequential proxy technique, Tchebycheff method, step method and methods based on reference points [108].

Intelligent MOO techniques are more popular these days because of their superior problem-solving behavior. Most of the novel intelligent methods do not require any type of gradient information and hence it is computationally less complex when solving higher dimensions and highly nonlinear systems. Moreover, these population-based algorithms are suitable for solving problems with discontinuities in the objectives [39]. Further, the classical methods suffer from tracking in sub-optimal or local optimal solutions, as well as most of them depending on the initial conditions [39]. Therefore, intelligent population-based MOO approaches are becoming more effective in the modern research arena. Many intelligent MOO techniques have been developed so far and the most popular methodologies are derived from the multi-objective evolutionary algorithm (MOEA). MOEAs can be broadly categorized into two sections, which are the non-elitist MOEAs and elitist MOEAs [39]. Examples for the non-elitist MOEAs are vector evaluated GA (VEGA) [109], weight-based GA (WBGA) [110], random weighted GA (RWGA) [111], multiple objective GA (MOGA) [112], non-dominated sorting GA (NSGA) [113] and niched pareto GA (NPGA) [114]. On the other hand, some of the elitist MOEAs are distance-based Pareto GA (DPGA) [115], elitist non-dominated sorting GA (NSGA II) [72], and strength Pareto EA (SPEA) [116]. A summary of the MOO solution methodologies is given in Figure 2.1.

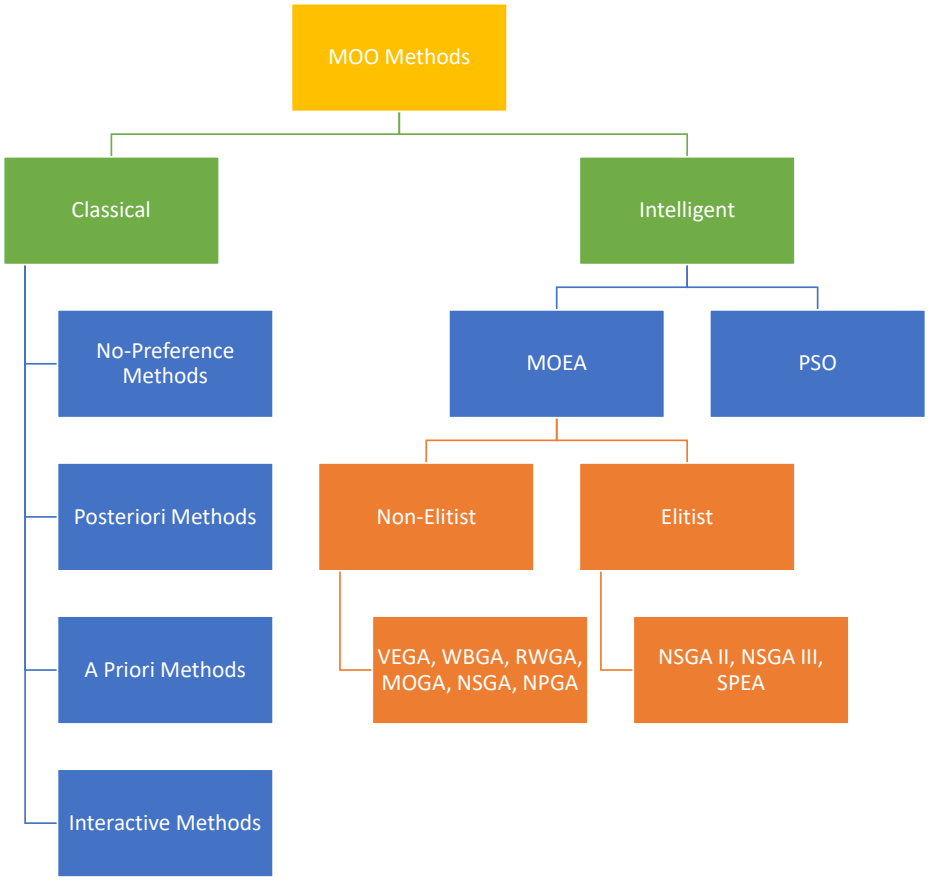

Figure 2.1: MOO solution methodologies.

Real-world MOO problems often need to be solved under certain constraints. To achieve the constraint handling capability, existing MOEAs need to be modified. Multiple constraint handling approaches have been proposed for the MOEA and some of them are summarized here. The most straightforward way of dealing with the constraints is ignoring infeasible solutions [39]. Another common method is the penalty function approach where each solution is given a penalty depending on the magnitude of the constraint violation [117]. Another constraint handling approach with the binary tournament selection named as Jimenez-Verdegay-Gomez-Skarmeta method is proposed in [118] considering only the inequality constraints of the type less than or equal. A novel constraint handling technique for MOEA is proposed in [119] based on an adaptive penalty function and a distance measure. The constrained tournament method is the technique employed in the original NSGA II algorithm to handle the inequality constraints of the type greater than or equal [39, 72]. Ray-Tai-Seow's

method is proposed in [120] where a non-domination check of the constraint violations taking into account when dealing with the constraints.

2.4 Transient Optimization and Optimal Control in Microgrids

Transients in MGs occur as a result of various disturbances in the system such as load changes, due to the intermittent and dynamic nature of DGs and transitions from islanded mode to grid-connected mode and vice versa [121]. Oscillations that are initiated as results of the transients must be damped to maintain the system stability. Improvements in the transient operations of MGs are reported in the literature [31–34, 70, 71, 86, 87, 122–126]. Majority of the work has been done to improve the transients of the droop based MGs [70, 71, 86, 122, 123]. In order to improve the dynamic response, transient droop technique is introduced in [70] by appending the active and reactive power derivative and integral terms to the conventional static droop equations. Similar work can be found in [86], where the static droop characteristics are combined with the transient droop functions by employing a 2-DOF tunable controller. The major difference in this approach is, transient droop gains are adaptive to damp the oscillatory modes at different operating conditions. The transient response of the droop based controller is highly degrading due to the low pass filtering of the calculated instantaneous active and reactive powers [71, 86]. As a solution, active and reactive power calculation, and low pass filtering is replaced by a synchronous reference frame phase-locked loop in [71]. Also, the virtual impedance loop and proportional resonant controller in the voltage control loop are integrated to enhance the dynamic response of the system. In [122], improved transient response is achieved by introducing dynamic droop coefficients during a transient period. Here, virtual inertia is added to the system by modeling the active power droop gain as a function of the time derivative of the frequency. Dynamics initiated as a result of the intermittent nature of the renewable sources are addressed in [123] and [124] considering solar PV sources. Based on the argument that the droop gains must vary according to the maximum power point curve of their associated PV array, in [123] droop coefficients are tuned as solar irradiation changes without any measure of the irradiation. In order to improve the transient response, a real-time voltage and frequency compensation strategy is proposed in [124]. Here, an adaptive virtual impedance loop is designed to suppress the voltage fluctuations caused due to the variations in the PV and an adaptive virtual frequency

impedance loop is introduced to regulate the frequency.

Even though transient improvements are considered in the aforementioned approaches, none of them focus on the optimum transient response or the path optimization of the individual inverters. Subsequent works done in [31–34,87,125,126] depict the optimum control of MGs operated with DG resources. An optimized sensitivity analysis based decentralized control method for a distribution network is proposed in [87]. Voltage regulation, the minimization of the active power losses and the reactive power exchanged with the distributed generation units are achieved by employing an artificial intelligence-based optimization technique. However, this is more on steady-state static optimization, and no attention has been posed for transient optimization. An optimal control method of a multi-inverter system is presented in [125] which tries to minimize a performance index, consist of the output voltage error, the inductor currents of all the inverters and the reference signals. In this approach, a single objective function is considered for the complete system including all the control variables and states, and the minimization is done in a cooperative manner. Optimum dynamic response of parallel operation of inverters is achieved in [31] by setting the optimum droop gains obtained via the differential evolution global search technique. This method uses the complete system matrix of the whole system to find the optimum droop gains. In that sense, this method illustrates a cooperative technique that needs the information of other DGs in the system.

Transient optimization of MGs when subjected to a mode change is addressed in [32–34, 127]. Based on the small-signal model of the droop controlled MG, optimum droop and PI controller gain calculation methodology is proposed in [32]. A GA based optimization technique is employed to improve the dynamic response during the switching between grid-connected and islanded mode. This modeling approach tries to minimize the deviation between the instantaneous power and the nominal output power of the inverter. However, this nominal output power is used in the performance index is not the steady-state optimum power productions of the DGs. Another drawback of this approach is, this needs the small-signal dynamic model of the system, which makes the analysis complex. In [33] and [34], the PSO technique is employed to tune the PI controller gains and droop gains of the droop based MG operated in the islanded mode or grid-connected mode. Objective functions in [33] are proposed to minimize the error in the measured power and to enhance the damping

characteristics in each mode of operation. On the other hand, in [34], the performance index comprises active and reactive power errors and voltage and frequency deviations from the nominal values. Here, DGs are coordinated via droop controllers and a supervisory centralized controller. Hence this method is neither a non-cooperative technique nor a decentralized method. Further, the power references or the nominal values used in the above two methods are not the optimum values that minimize the individual costs of each DG. Optimum parameter selection methodology for a droop based MG to improve the transient time and to minimize the frequency drop is proposed in [127] based on the Imperialist Competitive Algorithm. This method suggests the best parameters for voltage source inverters since the objective function is formulated to minimize the transient time. Based on the evolutionary theory, in [126] droop gains are tuned to their optimum values to minimize the settling time. In addition, this method guarantees stable and fast damping responses.

Recently optimal control, model predictive control (MPC), multi-agent distributed control and game theoretic based control have gained more attention in the MG control arena [3, 11, 44, 45]. All of these techniques are related in the sense that they generate the control inputs to minimize an associated cost functional [128, 129]. In [3] and [11] open-loop optimal control actions are generated to optimally control resources in MGs using Pontryagin's minimum principle [128]. An optimal load player management strategy is proposed in [3] by modeling the end loads as variable impedances. In [11], local optimal control of source players in an ACMG is achieved by minimizing the quadratic state cost and control effort of each DG. A distributed feedback optimal control strategy is developed in [44] to cooperatively control active sources in a DCMG. The performance index of this modeling is constructed to achieve optimal voltage and power regulation of each DGs in the MG. In [45] MPC based maximum power point tracking methodology is applied to control PV sources in a DC distribution system. Further, MPC is employed to develop an optimal droop based current regulator to interface PV sources into the DC distribution system.

Game theory-based controls are one of the emerging decision making technology in the modern MG environment. Game theory is used under the competitive circumstances where the outcome of an individuals' selection of action depends on the actions of others [130,131]. Some of the key areas where these controllers employed in the MG domain are [132], energy demand estimation and supply cost, smart grid load balancing, MG modeling and analysis, price

directed energy utilization, agent-based micro storage management, and demand and load management. The design of an optimal grid stabilizer for weak/islanded grids using a unified power quality conditioner is proposed in [133]. Here, a zero-sum, two-player game is formed between unified power quality conditioner control and grid disturbances to design a discrete-time Hamilton–Jacobi–Isaacs nonlinear optimal controller through a continual approximation of a cost function using NNs. Active power production equilibria of renewable generations are obtained in [134] by employing the game theory under the assumption of negligible reactive power variations. Both of these methods are based on numerous assumptions and complex modeling approaches. In addition, applications of the game theory can be found in [135–138] for load frequency control, distributed dispatch, and energy consumption scheduling. In [135], a differential game-based cooperative control approach is adopted to study the two-area and three-area load frequency control of interconnected power systems. In the contest of energy demand estimation and supply cost, energy consumption scheduling games are considered by taking users as players and daily schedules of their household appliances and loads as strategies. Under this, distributed dispatch strategy based on the population games is proposed in [136] and hierarchical MG management system which leads to efficient load sharing among the available DGs based on dynamic population games is proposed in [137]. In addition to that, the dynamic maximization of the MG utility is achieved by the evolutionary game theory approach. An incentive-based, autonomous and optimal energy consumption scheduling scheme is presented in [138] to minimize the cost of energy and also to balance the total residential load. An energy consumption scheduling game is formulated among the consumers and their strategies are taken as the daily schedules of their household appliances and loads. Moreover, game-theoretic, decentralized optimum decision-making methodology is presented in [3] and [4] for DC MGs.

Reinforcement learning (RL) inspired various ADP methods have been developed to solve optimal control problems in past few decades [53–55, 129, 139, 140]. Feedback optimal cooperative and multi-agent control architectures for dynamical systems who seeks collective behavior is discussed in [129]. RL based feedback optimal and game-theoretic control development can be found in [139] and [55]. The State Following Kernel method based feedback optimal control approach is proposed in [140]. Varies classes of ADP based feedback optimal controls such as Q-learning, value gradient learning, policy iteration, single network

adaptive critic, and robust ADP are presented in [53]. Further, discrete and continuous-time ADP, feedback optimal control of non-affine systems and applications of ADP techniques in real-world problems can be found in [54].

These methodologies are becoming more popular in MG control domain too [46–51]. An ADP based optimal control methodology is developed in [46] to operate partially known parallel-connected voltage source inverters (VSI) in an ACMG. In this modeling, the local performance indices are generated to minimize the output voltage error and circulation currents among the other VSIs. An intelligent dynamic energy management system (EMS) is proposed in [47] for a smart MGs. Combining evolutionary ADP and RL frameworks, an action dependent heuristic dynamic programming method is employed to solve the dynamic optimization problem while maximizing reliability, self-sustainability, environmental friendliness, extended battery life, and customer satisfaction. Application of adaptive critic based disturbance attenuation method for the MG system is presented in [48]. Here the problem is modeled as a two-player zero-sum differential game and control signals are generated to guarantee the load frequency regulation of the MG under load disturbances and energy uncertainties. An adaptive critic based dynamic stochastic optimal control design for a MG is proposed in [49]. The main objectives of this approach are modeled to smoothen the PV and wind generation output, to reduces the power losses and to maximizes the usage of battery-based energy storage systems while providing dynamic reactive power support. An optimal battery management controller for a smart residential MG system is developed in [50] by a novel mixed iterative ADP algorithm. In this modeling, the objective function is selected to minimize the total cost from the grid, to make the stored energy of the battery close to the middle of the storage limit, and to prevent large charging or discharging power of the battery. A differential game-theoretic approach is proposed in [51] to collectively control active loads in a DCMG. Here, the obtained coupled algebraic Riccati equations are solved by an offline RL based policy iteration algorithm.

2.5 Solution of Optimal Control Problem

Solution methods of optimal control problems (OCPs) can be broadly divided into two sections namely direct methods and indirect methods. Direct optimal control methods transform the optimal control problem into a nonlinear programming problem and use

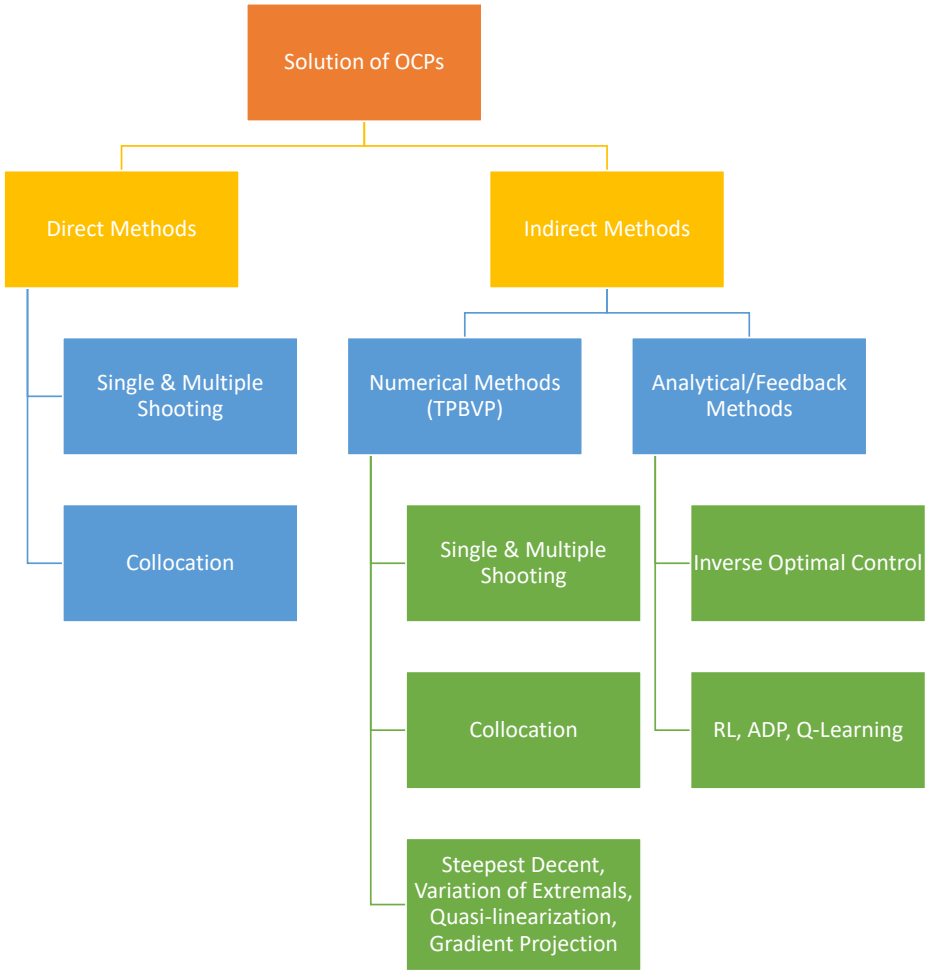

Figure 2.2: Optimal control solution methodologies.

numerical techniques to solve it. Direct single shooting, direct multiple shooting, and direct orthogonal collocation are some of the direct optimal control solution methods [128, 141–143].

Indirect methods can be again classified into numerical solution methods and analytical solution methods [55]. Generally in numerical solution techniques, Hamiltonian is formulated and resultant two-point boundary value problem (TPBVP) is solved using techniques such as indirect collocation method, indirect single and multiple shooting, steepest descent based technique, the variation of extremals, quasi-linearization and gradient projection [128, 143]. The TPBVP is generated via Pontryagin's minimum/maximum principle which results in state and costate dynamical equations and boundary conditions [128]. Analytical solution methods are based on the dynamic programming and associate Hamilton Jacobi Bellman

(HJB) equation which is highly nonlinear, difficult to solve, partial differential equation [128]. In linear systems, the HJB equation is simplified to the algebraic Riccati equation (ARE) [144]. For nonlinear systems, alternate methods have been developed to find the analytical solution to the optimal control problems such as inverse optimal control method [145, 146]. An approximate solution to the HJB equation is obtained by the RL based techniques such as temporal difference based methods, Q-Learning, adaptive dynamic programming (ADP) [53–55, 129, 139, 140]. Summary of the optimal control solution methodologies is given in Figure 2.2.

2.6 Constant Power Load and Power Buffer Controls in Microgrids

Negative impedance characteristics of CPLs introduce instabilities to the power systems [56–58]. In order to mitigate the instabilities and stabilizes CPL based MGs, various hardware-oriented methods and control-oriented methodologies have been developed [56, 57, 59–61]. Because of the high cost, loss and space requirements associated with the hardware-oriented methods, the addition of resistive loads, the inclusion of filters, load shedding, and placement of energy storage devices are not much popular [56, 61]. On the contrary, various control-oriented methodologies can be found in the literature such as linear controllers [62], boundary controllers [63], game-theoretic controllers [3,51], and sliding mode controllers [64,65]. A linear control approach is proposed in [62] to improve the stability margin of an inverter-based motor drive system followed by a CPL supplied by an imperfect dc power supply. The introduced linear controller act as an oscillation compensator which is realized by a stabilization block containing a bandpass filter and a proportional regulator. A boundary controller is presented in [63] with a first-order switching surface to control instantaneous CPLs attached to buck converters. The proposed method eliminates the large oscillations that occur in the buck converter operations under CPLs by a linear switching surface with a negative slope. In [56], a comprehensive analysis of stability issues in DCMGs with instantaneous CPLs and possible solutions are presented. Both hardware and control-oriented approaches are analyzed in terms of their advantages and disadvantages. Here, a nonlinear boundary controller which is based on state-dependent switching of LRC semiconductor devices, linear controllers such as PID controllers and nonlinear controllers based on passivity are discussed to stabilize CPL instabilities. Application of sliding mode and feedback linearization control methods

to stabilize the automotive converter systems with CPLs is carried out in [57]. In this approach, an assessment of the negative impedance instability of the CPLs in automotive power systems is presented. Further, in [59] two linear stabilizers are introduced to stabilize parallel-connected DC-DC buck converters connected to CPLs. Here, the first method is employed under constant voltage source mode while the second method is employed with the droop mode. Bifurcation analysis of CPL based power system is carried out in [64]. Here, a load bus voltage regulation problem under instantaneous CPLs is addressed through a sliding mode controller considering a DC-DC bidirectional boost power converter.

The power buffer is an effective method of mitigating instabilities caused by nonlinear load profiles, which has been introduced in [66] and discussed in [3, 51, 67–69]. In these approaches, the PEI followed by the CPL is modeled as a variable impedance load seen by the distribution network which is referred to as an active load. Then its effective input impedance is maneuvered to stabilize the MG subjected to any transients such as startup or abrupt load changes [67]. The power buffer contains large storage capacity and it is used to buffer, store and shape the input energy profile to the load rather than voltage regulation [147]. Pontryagin's minimum principle [128] is utilized in [67] to obtain the optimal geometric manifolds which stabilize the CPL with the buffer energy. The extraction of the geometric manifold in the energy-power domain based on the a priori computation of the reactions and trajectories is carried out in [69]. Here the problem is formulated as a non-cooperative game and Pontryagin's minimum principle is employed to extract the solution. Further, in [3] a non-cooperative game-theoretic controller development is proposed to improve the transient of active loads during a cold start using Pontryagin's minimum principle. Steady-state game-theoretic solutions for the active loads operate DCMG is proposed in [4]. Here, a turn-based approach is employed to obtain the optimal solution in a decentralized manner. The main drawback of all the aforementioned approaches is they provide open-loop numerical solutions. The solutions are stored in a memory or a lookup table for use in a particular situation such as load change or at startup. Feedback cooperative and game theoretic approaches in power buffer control are very limited and can be found in [51] and [68]. In these methodologies, dynamic programming is employed to obtain optimal solutions to stabilizes the MG. These approaches provide feedback control algorithms that require communication which make the distribution system complex and degrades reliability.

CHAPTER III

MULTI-OBJECTIVE OPTIMIZATION OF DROOP CONTROLLED DISTRIBUTED GENERATORS IN ISLANDED DC MICROGRIDS

3.1 Major Objectives

In order to eliminate the drawbacks in traditional droop control such as high load dependency on the system voltage and current sharing errors, a multi-objective optimization (MOO) based optimal droop coefficient computation methodology is developed. Unlike the traditional droop coefficients which are assigned based on the distributed generator (DG) capacity, the proposed approach considers three other objectives when computing the optimal droop gains. These are, overall system voltage regulation, current sharing improvement, and system loss minimization. A series of best virtual resistances and reference voltages for each DG in the system are computed while simultaneously minimizing all the objectives using NSGA II Multi-Objective Evolutionary Algorithm. In order to find out the best compromise solution from the generated Pareto optimal front, a fuzzy membership function approach is also presented. Further, to test the performance of the computed optimal droop relationships, a state feedback linearized controller is introduced. The proposed approach was tested with a parallel-connected DC 9 bus system, IEEE 30 bus system and experimentally validated on a five bus system. The proposed approach is different from the existing optima droop coefficient computation methods since they use weighted sum approaches to aggregate multi objectives to get a single objective function. Then they use single objective optimization techniques to find optimal droop gains. However, the proposed approach in this dissertation

employs a MOO technique to find the Pareto optimal front of the problem and then the best compromise solution is extracted. Main findings of this chapter are published in [148].

3.2 Droop Control in DC Microgrids

Typical DCMG is a combination of sources and loads connected to the common DC bus. This type of MG is called a parallel-connected bus system since sources and loads are connected in parallel to the common bus. Sources in MGs are referred to as DGs which are typically renewable sources followed by PEIs. In any type of a MG, the control of DGs is primarily done by droop control [25]. In the DC droop control, the load sharing is achieved by properly varying the DG output voltage (V_o) according to the measured output current (I_o) [25]. The output voltage reference (V_o^*) of a DG is given by the linear droop relationship as in (3.1) [25, 35].

$$V_o^* = V_r - R_D I_o \tag{3.1}$$

This droop relationship comprises of two constant droop coefficients namely the virtual resistance (R_D) and the output voltage reference at no load (V_r) [25]. Suppose that δV_{max} is the maximum allowed voltage deviation and I_{max} is the maximum output current, then R_D is typically designed as in (3.2) [25]. The reference voltage is usually equal to the nominal system voltage V_n.

$$R_D = \delta V_{max}/I_{max} \tag{3.2}$$

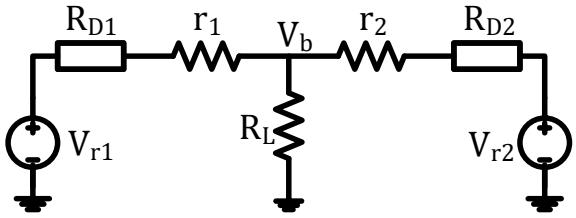

Figure 3.1: Two DG one load example test system. © [2020] IEEE.

The two primary objectives in droop based DG sources are the voltage regulation and proper load sharing [149]. This ensures stability as well as the reliability of the system and it helps to avoid any overloading of DGs. In order to understand the load sharing of droop based parallel DG system, consider the simple two DG and one resistive load system shown

in Figure. 3.1. The reference voltages of the DGs are V_{r1}, V_{r2}, virtual resistances are R_{D1}, R_{D2} and distribution line resistances are r_1 and r_2. Bus voltage at the load is V_b and the load resistance is R_L. The relationships (3.3) and (3.4) give the voltage at the load bus and the difference in current supplied by the DGs.

$$V_b = \frac{(R_1 V_{r2} + R_2 V_{r1}) R_L}{(R_1 + R_2) R_L + R_1 R_2} \tag{3.3}$$

$$\Delta I = \frac{2(V_{r1} - V_{r2}) R_L + R_2 V_{r1} - R_1 V_{r2}}{(R_1 + R_2) R_L + R_1 R_2} \tag{3.4}$$

In (3.3) and (3.4), $R_1 = R_{D1} + r_1$ and $R_2 = R_{D2} + r_2$. According to (3.4), the current sharing error is inversely proportional to the virtual resistances. Hence, if the DG virtual resistances are increased, then the current sharing can be improved. However, as the virtual resistances grow, the bus voltage degrades according to (3.3). Therefore, there is always a trade-off between voltage regulation and current sharing. In order to see the effect of virtual resistance on the current sharing and voltage regulation, two objectives are defined in (3.5) and (3.6).

$$f_1(R_{D1}, R_{D2}) = |V_n - V_b| \tag{3.5}$$

$$f_2(R_{D1}, R_{D2}) = |\Delta I| \tag{3.6}$$

Nominal voltage V_n is set to 110 V and the line resistances are set to 0.1 Ω. The reference voltages of both the DGs are kept at 111 V and the load resistance is selected as 20 Ω. The corresponding objective functions are plotted in Figure. 3.2 and it can be seen that it is difficult to extract a single solution that minimizes both the objectives by mere observation of the objective variations.

Analytically, the Pareto optimal front of two objective functions with two decision variables is given by, [150].

$$\frac{\partial f_1}{\partial R_{D1}} \frac{\partial f_2}{\partial R_{D2}} = \frac{\partial f_1}{\partial R_{D2}} \frac{\partial f_2}{\partial R_{D1}} \tag{3.7}$$

Optimal virtual resistances that minimize both the objectives are found along the curves as shown in Figure. 3.3, which are the solutions of (3.7). All the solutions along these curves are equally good. For a multi-bus system with more objectives and decision variables, finding an analytical solution for the Pareto optimal front is difficult and computationally inefficient.

Therefore, employing an intelligent MOO method is beneficial.

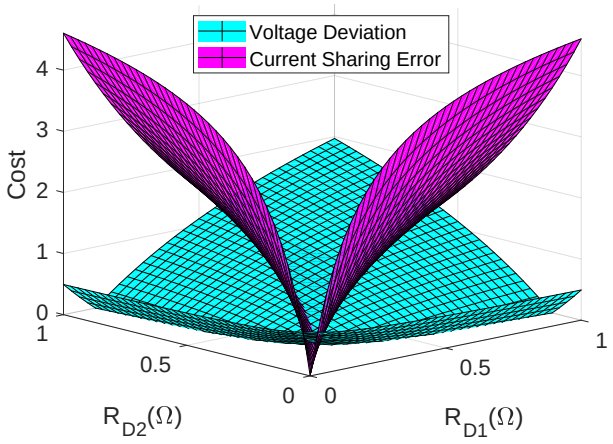

Figure 3.2: Cost variation of the two objective functions. © [2020] IEEE.

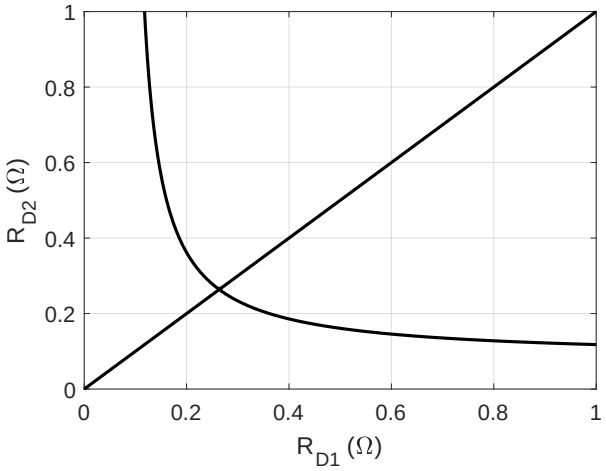

Figure 3.3: Pareto optimal front in the decision variable space. © [2020] IEEE.

3.3 Multi-Objective Formulation

Mathematical modeling of the MG and objective function formulation are explained in this section. Suppose there are N number of buses in the MG with g number of DGs in the set $\mathcal{G}$ and $N-g$ number of load buses in the set $\mathcal{L}$. Each DG can be modeled as a voltage source followed by a virtual resistance as shown in Figure. 3.1. From the nodal current and voltage relationship, the current injected to the $k^{th} \in \mathcal{G} \cup \mathcal{L}$ bus can be written as,

$$I_k = \sum_{\substack{j=1 \\ j \neq k}}^{N} (V_k - V_j) Y_{kj} \tag{3.8}$$

where, Y_{kj} is the admittance between bus k and bus j and $k, j \in \mathcal{G} \cup \mathcal{L}$. For a DG bus, the injected current can be replaced by (3.1) and the resulting nodal current and voltage equation will be,

$$\frac{V_{rk}}{R_{Dk}} = V_k \left(\frac{1}{R_{Dk}} + \sum_{\substack{j=1 \\ j \neq k}}^{N} Y_{kj} \right) - \sum_{\substack{j=1 \\ j \neq k}}^{N} Y_{kj} V_j \tag{3.9}$$

where, $k \in \mathcal{G},\ j \in \mathcal{G} \cup \mathcal{L}$. On the contrary, for a load bus with a resistive load, the load resistance can be inserted as an admittance connected to the bus and hence the injected current becomes zero. For instance, the nodal relationship of the $k^{th} \in \mathcal{L}$ load bus can be shown as,

$$0 = V_k \left(\frac{1}{R_{Lk}} + \sum_{\substack{j=1 \\ j \neq k}}^{N} Y_{kj} \right) - \sum_{\substack{j=1 \\ j \neq k}}^{N} Y_{kj} V_j \tag{3.10}$$

where, $k \in \mathcal{L},\ j \in \mathcal{G} \cup \mathcal{L}$. The nodal relationship for the N bus power system can be obtained as in (3.11).

$$I = YV \tag{3.11}$$

where, I is the modified injected current vector given by (3.12) and V is the bus voltage vector.

$$I = \left[\begin{array}{cccc|c} V_{r1}/R_{D1} & V_{r2}/R_{D2} & \cdots & V_{rg}/R_{Dg} & \underline{0} \end{array} \right]^T \tag{3.12}$$

In (3.12), $\underline{0}$ is the zero vector with length $N - g$, Y is the modified system admittance matrix with additional terms added to the diagonal entries of the usual admittance matrix. In case of a DG bus, $1/R_{Dk}$ $(k \in \mathcal{G})$ is added to the corresponding diagonal term and $1/R_{Lk}$ $(k \in \mathcal{L})$ is added if the bus is a load bus.

3.3.1 System Voltage Regulation

Overall system voltage regulation is one of the most important objectives in DCMGs. Voltage vector (V) of the MG can be computed from the nodal relationship derived in (3.11) as,

$$V = Y^{-1} I \tag{3.13}$$

The first objective can be formulated in two ways. Either minimize the error between the average voltage in the MG and the system nominal voltage V_n as in (3.14) or minimize the aggregated error between individual bus voltages and nominal voltage V_n as in (3.15).

$$f_1 = |V_n - \frac{1}{N} \sum_{j=1}^{N} V_j| \tag{3.14}$$

$$f_1 = \frac{1}{N} \sum_{j=1}^{N} |V_n - V_j| \tag{3.15}$$

3.3.2 Current Sharing Improvement

Once the DG voltages are extracted from the voltage vector (V), current injections of each DG can be calculated by employing (3.1). Then, the overall current sharing error in the system can be computed as (3.16) and minimization of this error will be considered as the second major objective.

$$f_2 = \sum_{k=1}^{g-1} \sum_{j=k+1}^{g} |I_k - I_j| \tag{3.16}$$

where, $I_k = (V_{rk} - V_k)/R_{Dk}$.

3.3.3 System Active Power Loss Minimization

Due to the distribution line resistances, active power losses exist in the MGs. Droop coefficients can be tuned to minimize power loss for a given system and the objective needing to be minimized can be considered as,

$$f_3 = \sum_{k=1}^{N-1} \sum_{j=k+1}^{N} Y_{kj} \left(V_k - V_j\right)^2 \tag{3.17}$$

The minimization of this objective is considered as a secondary objective. The main attention will be given to voltage regulation and current sharing improvement.

3.3.4 Impact of Constant Power Loads

Optimal droop coefficient computation under constant power loads (CPLs) is discussed in this section. CPLs are nonlinear loads that introduce instabilities to the power system. A CPL can be represented as a variable resistive load and it can be modeled with the aid of power electronic converters [3, 4]. The control goal of the converter will be to maintain the input power equal to the desired power value of the CPL. This will include an extra equality constraint to the MOO problem as shown in (3.18). Here, P_k is the desired active power of the CPL. In order to maintain equality in every instance, the proper value of the variable

resistance R_{Lk} needs to be computed depending on the bus voltage (V_k). Hence, this will increase the number of decision variables in the MOO problem.

$$c_{eq,k} = P_k - \frac{V_k^2}{R_{Lk}} \tag{3.18}$$

3.3.5 Optimization Constraints of the Proposed Approach

In the DCMG point of view, the developed MOO problem needs to be solved under certain power system constraints. First, the droop coefficients must be computed within the given maximum and minimum values as shown in (3.19). The decision variable vector ϕ and its lower and upper bounds are given as ϕ^L and ϕ^U must be set such that the overall system stability is being protected. The stability can be verified by performing small signal stability around the steady-state operating point of the system.

$$\phi^L \leq \phi \leq \phi^U \tag{3.19}$$

Further, the solutions must satisfy the power flow equality constraints, which are already taken into consideration while constructing the objectives. Moreover, all the bus voltages need to be inside the allowable voltage margins as in (3.20). In (3.20), allowable lower and upper bounds of the bus voltages are given as V^L and V^U respectively.

$$V^L \leq V_j \leq V^U \quad j \in \mathcal{G} \cup \mathcal{L} \tag{3.20}$$

Next, all the DG voltages and currents must be under the allowable maximum voltage drop (δV_{max}) and the maximum allowable current (I_{max}) limits as shown in (3.21) and (3.22).

$$|V_n - V_k| \leq \delta V_{max,k} \quad k \in \mathcal{G} \tag{3.21}$$

$$I_k \leq I_{max,k} \quad k \in \mathcal{G} \tag{3.22}$$

Further, if there are CPLs in the system, then the MOO problem needs to be solved under the corresponding equality constraints as explained in 3.3.4. When the DCMG structure changes from a parallel system to a mesh system, the admittance matrix needs to be modified

accordingly. Next, the developed MOO problem which contains the objectives (3.14)-(3.17) and constraints (3.18)-(3.22) need to be solved using a suitable MOO technique. The multi-objective evolutionary algorithms (MOEAs) are the most popular solution methods which are employed to solve MOO problems by identifying the Pareto optimal front. Among them, Elitist non dominated sorting genetic algorithm (NSGA II) is the most widely used MOEA in the literature and has been employed in this dissertation. It utilizes both the elite preservation strategy and explicit diversity preservation mechanism.

3.4 Best Compromise Solution

The NSGA II generates a set of equally good non dominated set of solutions called Pareto optimal solutions. Each Pareto solution contains a set of optimized droop coefficients. Among them, selecting a suitable solution to apply in the real world application requires a decision-making strategy. In order to extract a compromise solution from the Pareto front, methods such as NNs [151], Pseudo weight vector approach [152] and fuzzy membership function approach [94] are available in the literature. NN approaches require training data sets and it involves the training of the network [151]. This training makes the problem complex and inefficient. The pseudo weight vector approach is also similar to the fuzzy membership function approach, which computes a pseudo weight vector for each solution in the Pareto front [152]. However, its capability of producing good outcomes has not been tested well in the literature. On the contrary, the fuzzy membership function approach does not require any training or training data set to apply in a decision-making problem. Moreover, it is a simple mechanism and has been proven to produce good results [94, 152]. Motivated by the fuzzy set theory, this paper implemented the fuzzy membership function approach to obtain the best compromise solution.

When formulating the fuzzy membership function, user-defined unacceptable and acceptable satisfactory values for each objective are assigned (f_i^{max} and f_i^{min}). It is required to find a single Pareto solution that has objective values close to the zero or to the user-defined satisfactory objective values and farthest away from the unsatisfactory objective values towards f_i^{min}. To achieve this, a linear fuzzy membership function is formulated and the membership function value is computed for each Pareto solution using (3.23). Suppose there is M number of solutions available in the Pareto optimal set. Then, the membership

value of the k^{th} solution in i^{th} objective (μ_i^k) is given by,

$$\mu_i^k = \begin{cases} 1 & \text{if } f_i^k \leq f_i^{\min}, \\ \frac{f_i^{\max} - f_i^k}{f_i^{\max} - f_i^{\min}} & \text{if } f_i^{\min} < f_i^k < f_i^{\max}, \\ 0 & \text{if } f_i^k \geq f_i^{\max}. \end{cases} \tag{3.23}$$

This value measures how close a Pareto solution to each of the satisfactory objective values or below. The membership function value is computed for all the objectives. In this particular problem, since there are three objectives, the membership function value of a single Pareto solution is a three-dimensional vector. The procedure first computes the fuzzy membership value for each solution and objective. Next, in order to obtain an overall measure of goodness from the three-dimensional performance vector, normalization is done using (3.24).

$$\mu^k = \frac{\sum_{i=1}^{N_{obj}} \mu_i^k}{\sum_{k=1}^{M} \sum_{i=1}^{N_{obj}} \mu_i^k} \tag{3.24}$$

where, N_{obj} is the number of objectives. This overall normalized membership value aggregates all the individual membership function values computed for a single Pareto solution. Then it produces a normalized measure of goodness in all the objectives. Once this normalization is performed for all the Pareto solutions, the Pareto solution, which possesses the highest value, is the best solution closes to zero cost or closes to all the satisfactory objective values. Hence, the Pareto optimal solution which has the maximum value of the normalized overall membership value is selected as the best compromise solution.

3.5 Proposed State Feedback Linearized Droop Controller

Controller design for a DG system to regulate the DG output voltages to the reference values given by the derived optimal droop relationships is discussed in this section. Every DG in a MG is connected to the system through a PEI as shown in Figure 3.4. In DC MGs, these can be DC-DC buck, boost or any other DC-DC converter. The boost power converter topology is considered as the example intermediate converter in this paper. First, the instantaneous output current ($i_{o,k}$) of the DG is sensed and the required output voltage reference ($V_{o,k}^*$) is calculated according to the droop relationship given in (3.1) with the

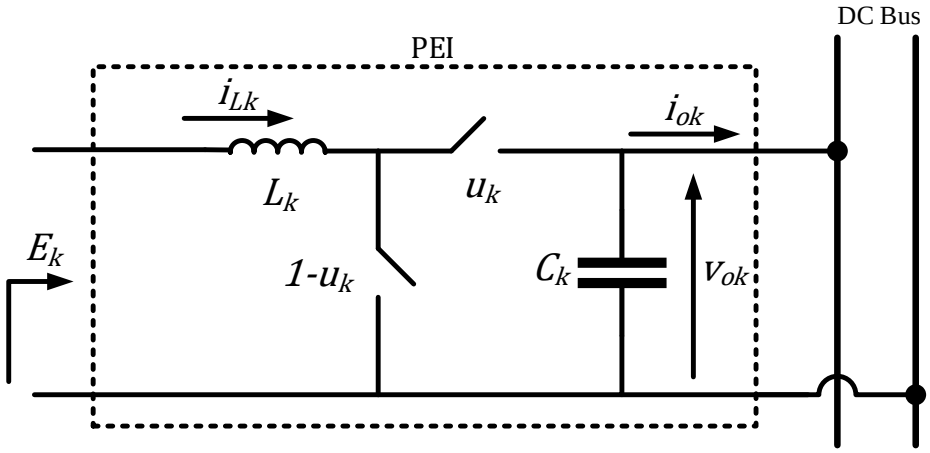

Figure 3.4: Boost PEI topology. © [2020] IEEE.

computed optimal droop coefficients. Next, using this voltage reference, corresponding inductor current reference ($I^*_{L,k}$) can be computed. Then, the state feedback linearization controller [153] is employed to regulate the output voltage and inductor current to the corresponding references. The dynamic model of the average mode boost converter can be expressed as,

$$L_k \frac{di_{L,k}}{dt} = -v_{o,k}u_k + E_k \tag{3.25}$$

$$C_k \frac{dv_{o,k}}{dt} = i_{L,k}u_k - i_{o,k} \tag{3.26}$$

where, L_k, C_k, E_k, u_k, $i_{o,k}$ $i_{L,k}$ and $v_{o,k}$ are the inductance, capacitance, input voltage, control input, output current, inductor current and output capacitor voltage of the k^{th} DG. For the ease of controller design, this dynamical model is converted to the Brunovsky's canonical form [153]. Two new states are defined as the total energy stored in the system ($x_{1,k}$) and the internal power of the converter ($x_{2,k}$) which are given by,

$$x_{1,k} = \frac{1}{2}\left(L_k i^2_{L,k} + C_k v^2_{0,k}\right) \tag{3.27}$$

$$x_{2,k} = E_k i_{L,k} - v_{o,k} i_{o,k} \tag{3.28}$$

With these new states, dynamical model of the boost converter in Brunovsky's canonical form can be represented as,

$$\dot{x}_{1,k} = x_{2,k} \tag{3.29}$$

$$\dot{x}_{2,k} = f\left(x_k\right) + g\left(x_k\right) u \tag{3.30}$$

where, $f(x_k) = E_k^2/L_k + i_{o,k}^2/C_k$ and $g(x_k) = -(E_k v_{0,k}^2/L_k + i_{o,k} i_{L,k}/C_k)$. Based on the reference output voltage ($V_{o,k}^*$) provided by the optimal droop relationship, the desired values of the states ($x_{1,k}^d, x_{2,k}^d$) are calculated as,

$$x_{1,k}^d = \frac{1}{2}[L_k (I_{L,k}^*)^2 + C_k (V_{o,k}^*)^2] \tag{3.31}$$

$$x_{2,k}^d = 0 \tag{3.32}$$

Here, $I_{L,k}^* = i_{o,k} V_{o,k}^*/E_k$ is the equivalent inductor current reference corresponding to the reference output voltage $V_{o,k}^*$. With the desired states, the system state error can be calculated as,

$$r_k = \alpha(x_{1,k} - x_{1,k}^d) + (x_{2,k} - x_{2,k}^d) \tag{3.33}$$

The dynamics of the error system can be obtained as,

$$\dot{r}_k = \alpha x_{2,k} + f\left(x_k\right) + g\left(x_k\right) u_k \tag{3.34}$$

Under the control input given by (3.35), it can be shown that the dynamical system is stable and it drives the system state error to zero [153]. Consequently, the error between the actual output voltage and the reference output voltage will become zero at the steady-state. In the controller, α and K are positive design constants.

$$u_k = \frac{1}{g(x_k)}(-f(x_k) - \alpha x_{2,k} - K r_k) \tag{3.35}$$

Stability of the proposed controller can be analyzed by considering the positive definite Lyapunov function given by,

$$V_k = \frac{1}{2} r_k^2 \tag{3.36}$$

Time derivative of V along the error dynamics (3.34) can be shown as,

$$\dot{V}_k = r_k\big(\alpha x_{2,k} + f\left(x_k\right) + g\left(x_k\right) u_k\big) \tag{3.37}$$

Substituting the control input given by (3.35), the time derivative of the Lyapunov function can be shown to be a negative definite function given in (3.38). This concludes the asymptotic stability of the k^{th} DG error at the origin.

$$\dot{V}_k = -K r_k^2 \leq -K|r_k|^2 \tag{3.38}$$

Considering the overall Lyapunov function $V = \frac{1}{2}\sum_{k=1}^{g} r_k^2$, the asymptotic stability of the entire MG can be established by following the same procedure. The complete process is summarized in the flow chart given in Figure 3.5.

If the system has an emergency or a fault situation, as far as it is stabilizable, the stability and the control effect of the MG are guaranteed by the developed feedback controller under the computed droop gains. However, during the emergency period, the previously calculated droop coefficients may not be the optimal design. Thus, as an alternative, a new set of droop coefficients can be computed using the proposed approach and reassigned for the emergency period. This requires a centralized control unit to acquire information about the changes in the MG and to set the recomputed optimal droop coefficients. In MG domain, this is possible by establishing a communication medium for sharing the information.

3.6 Simulation Test Cases and Results

Simulations were carried out in Matlab considering the 5 DGs, 4 loads system shown in Figure 3.6 and the IEEE 30 bus system [154] with nominal voltage $V_n = 110$ V. The DGs can be any DC power source followed by the PEI as shown in Figure 3.4. In this modeling, it is assumed that the input voltage to each PEI is constant which is a typical assumption in many droop-based MGs in the literature [9, 25, 155]. Distribution line resistances were set to 0.2 Ω. Upper and lower bounds of the virtual resistances were chosen as 0.2 Ω and 1.5 Ω while the upper and lower reference voltage bound for all the DGs were set to 110 V and 115 V. The optimization constraints were considered as, $V_i > 0.95V_n$, $\delta V_{max} = 5$ V, and

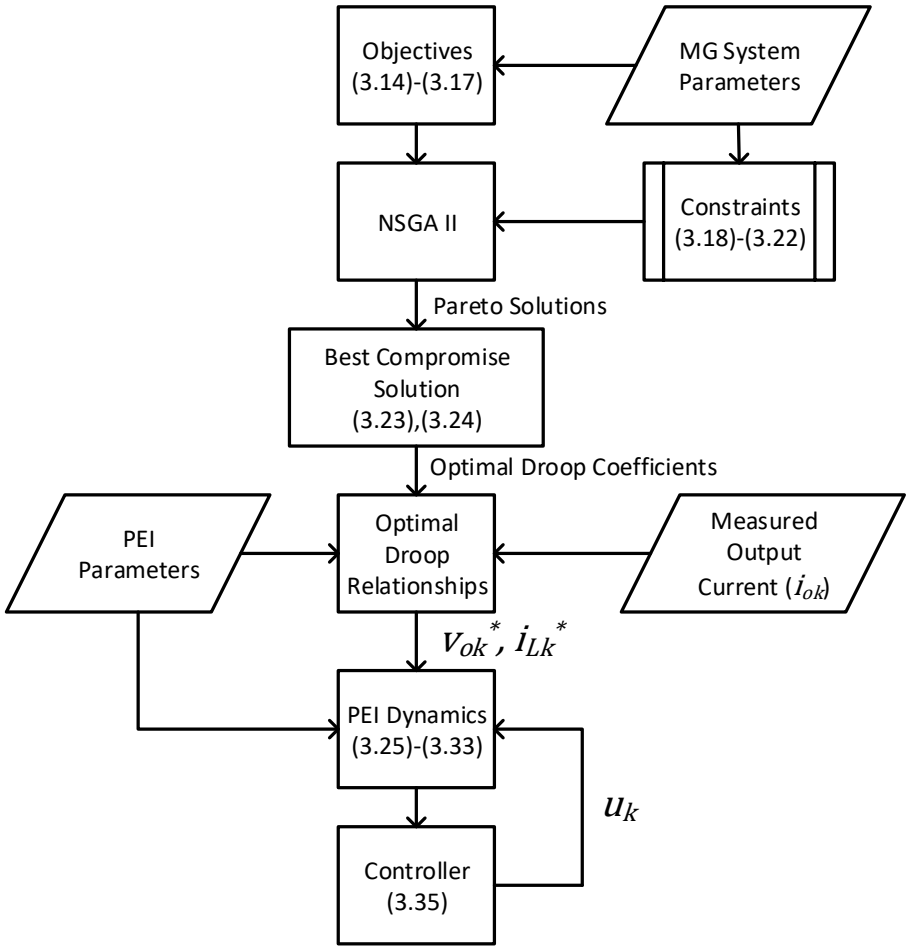

Figure 3.5: Procedure of the complete process. © [2020] IEEE.

$I_{max} = 10$ A. The unacceptable and acceptable satisfactory values for the best compromise solution are given in Table 3.1. These values can be assigned as users wish or observing the variation in the Pareto optimal front. In all the simulations these values were chosen to have the best possible voltage regulation and current sharing since those are the objectives with paramount importance. Several tests were performed such as equal DG reference voltages, arbitrary DG reference voltages, comparison with traditional droop, generator disconnection, MG with CPLs, unequal line resistance, and meshed MG system. In each case, MOEA was initialized with 500 individuals in the population.

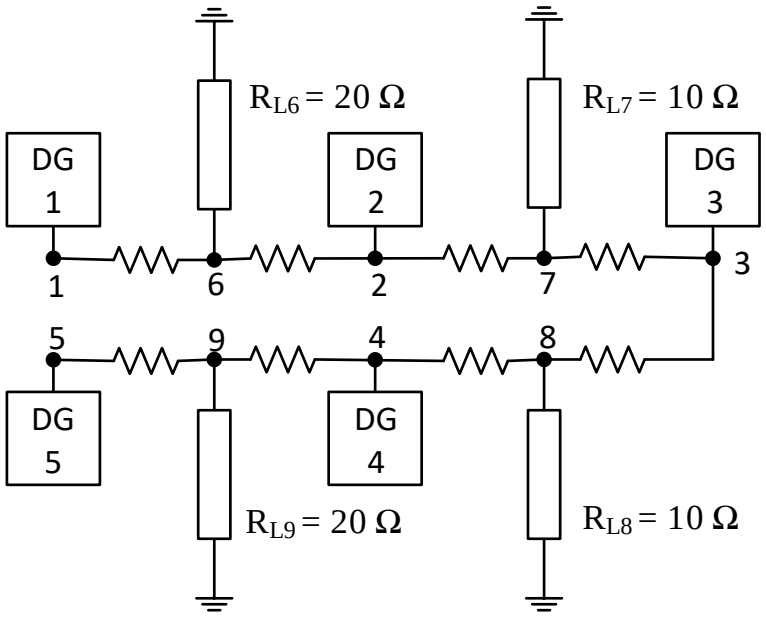

Figure 3.6: Parallel connected test system. © [2020] IEEE.

Table 3.1: Acceptable and Unacceptable Objective Values for the Best Compromise Solution

	f_1^{max}	f_1^{min}	f_2^{max}	f_2^{min}	f_3^{max}	f_3^{min}
Value	4 V	2 V	4 A	1 A	50 W	30 W

3.6.1 Parallel MG System with Equal DG Reference Voltages

Pareto optimal front in the objective space for equal DG reference voltages with equal line resistances is shown in Figure 3.7. The best compromise solution was found as $f_1 = 1.35$ V, $f_2 = 0.37$ A and $f_3 = 43.57$ W. At this point, optimal virtual resistances of DG 1 to DG 5 were obtained as 0.577 Ω, 0.796 Ω, 0.928 Ω, 0.796 Ω and 0.565 Ω. The optimal reference voltage for this test case was found at 113.87 V. Clearly the obtained best cost solution from the proposed fuzzy membership function approach lies below the unsatisfactory objective values defined for this problem. Moreover, the computed optimal solution shows $f_1 < f_1^{min}$ and $f_2 < f_2^{min}$ which are close to the zero cost. Without the fuzzy membership function approach, it would be infeasible to obtain such a solution by analyzing the Pareto front given in Figure 3.7 due to the conflicting nature of the objective values. For instance, the power loss increases if one traverses towards the zero voltage deviation point in the Pareto front

starting from the optimal solution. Further, seeking a solution with lower losses by traversing down from the optimal solution along the Pareto surface degrades both current and voltage deviations according to Figure 3.7. Moreover, current sharing minimization increases both system losses and voltage deviation. Therefore, it is very difficult to find a compromise solution without a decision making strategy. The fuzzy membership function approach eases the burden of finding the optimal solution along the Pareto optimal front.

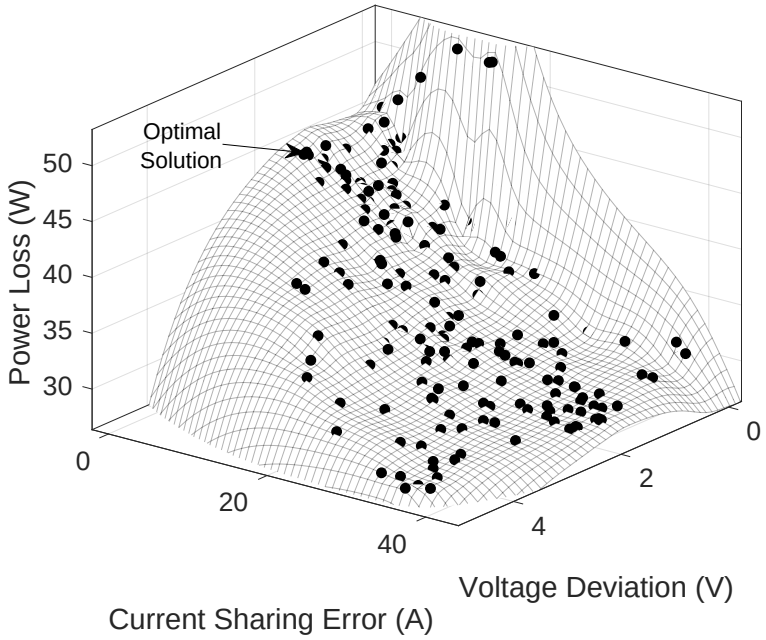

Figure 3.7: Pareto optimal front of parallel system with equal V_{ref}. © [2020] IEEE.

3.6.2 Parallel MG System with Arbitrary DG Reference Voltages

Pareto optimal front for arbitrary DG reference voltages with equal line resistances is shown in Figure 3.8. In contrast to the previous test cases, here an extra degree of freedom is included when computing the optimal droop parameters by allowing arbitrary reference voltages. The best compromise solution was found at the point $f_1 = 0.13$ V, $f_2 = 0.24$ A and $f_3 = 44.671$ W. Voltage deviation error is minimized compared to the previous case since different DGs are allowed to have different reference voltages. The corresponding virtual resistances obtained in this solution were, 0.522 Ω, 0.625 Ω, 0.695 Ω, 0.519 Ω and 0.399 Ω. Moreover, the computed optimal DG reference voltages were, 114.87 V, 114.01 V, 113.62 V,

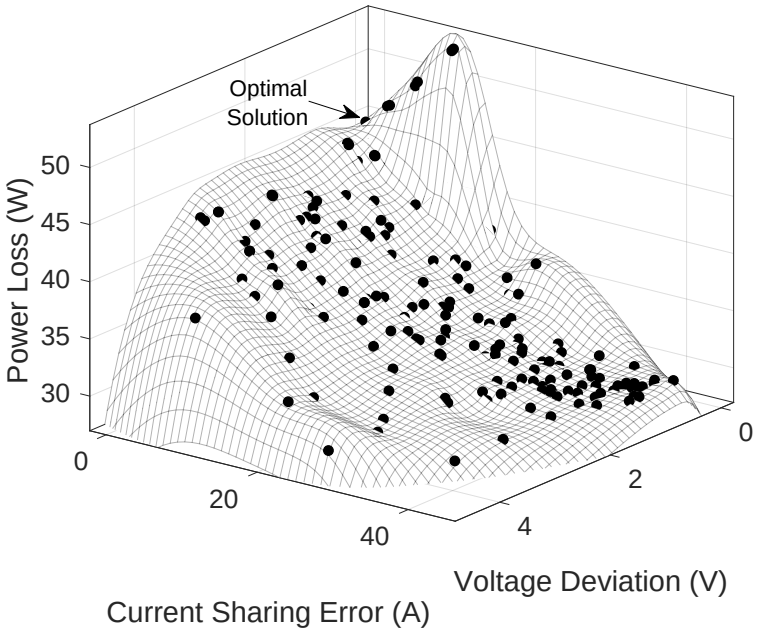

Figure 3.8: Pareto optimal front of parallel system with arbitrary V_{ref}. © [2020] IEEE.

113.30 V, and 114.01 V respectively.

3.6.3 Performance Comparison with Traditional Droop

The parallel DG system in Figure 3.6 was controlled by the controller developed in section 3.5 with traditional droop coefficients and computed optimal droop coefficients. Then the performances of the optimal droop relationships were compared with the traditional droop relationships. In the traditional approach, all the DG virtual resistances were kept at 0.5 Ω and reference voltages were set to 110 V. These traditional droop coefficients were obtained by following the procedure described in section 3.2 based on the maximum allowable DG output voltage deviations and maximum output currents given above. Controller parameters α and K were set to 10 and 5000 and, boost converter parameters were selected as $L_k = 10$ mH, $C_k = 3.4$ mF and $E_k = 60$ V for all the DGs. Results of parallel DG system with equal line resistances are given in Figure 3.9 and Figure 3.10 and results of the other systems are presented at the end of each test case. In parallel DG system with equal line resistances, DG1, DG5, and DG2, DG4 voltages and currents are overlapping because of the symmetry of the network.

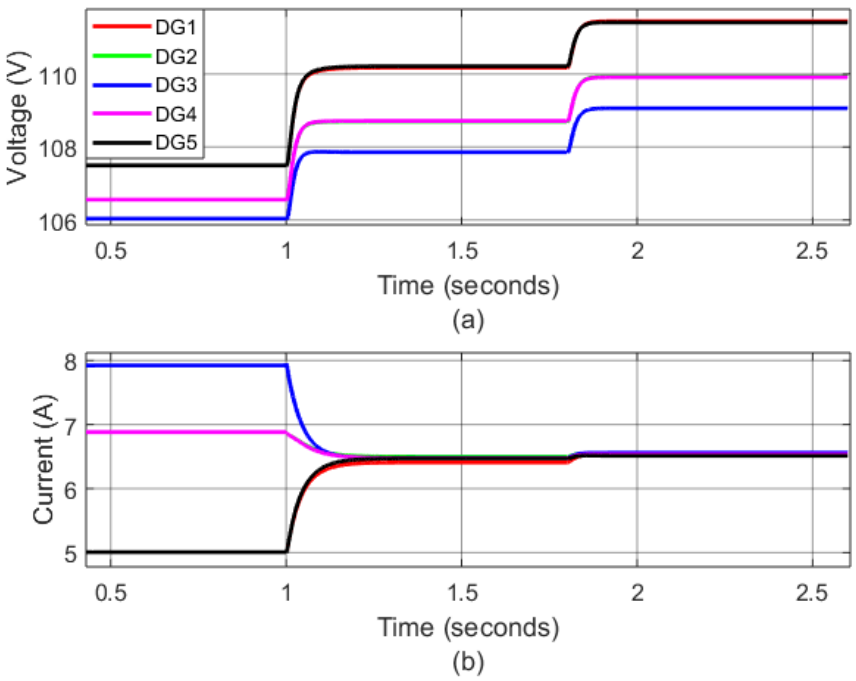

Figure 3.9: Variation of DG output voltages and currents in parallel DG system with equal line resistances (a) Voltages and (b) Currents. © [2020] IEEE.

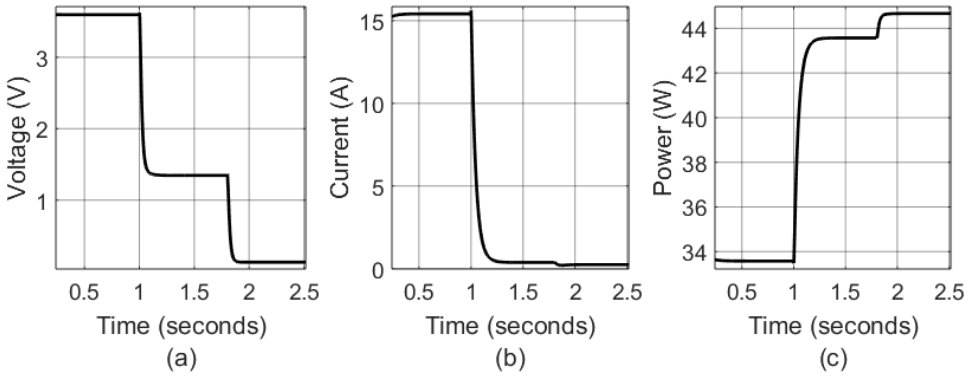

Figure 3.10: Variation of the objective functions in parallel DG system with equal line resistances (a) f_1, (b) f_2 and (c) f_3. © [2020] IEEE.

Parallel DG system with equal line resistances was initialized with the traditional droop coefficients and at t = 1s those were changed to optimal droop gains with equal reference voltages. Next, optimal droop coefficients with arbitrary reference voltages were set at t = 2s. The results show a significant improvement in voltage regulation and current sharing. Clearly, the DG output currents reach an equal value and remain close to each other

with the optimal droop and voltages are restored to keep the average system voltage close to the nominal value. In equal reference voltage case and in arbitrary reference voltage case, the observed voltage regulation improvements over the traditional droop coefficients were 62.5% and 96.4% respectively. Significant current sharing improvement can be identified in both scenarios and they are 97.6% and 98.4% over the traditional method. However, power loss minimization has been slightly degraded due to the compromisation between multiple objectives. Lower power loss can be always achieved by changing the f_3^{max} and f_3^{min} values which will result in degrading the voltage regulation and current sharing than in this case.

3.6.4 Generator Disconnection

The performance of the proposed approach under a fault or an emergency situation was evaluated under this test case. Initially, the MG in Figure 3.6 was controlled by the optimal droop coefficients with arbitrary reference voltages. When t = 2s, DG5 was disconnected from the MG and hence bus 5 becomes a load bus with no load attached to it. Variations in the DG output voltages and currents are shown in Figure 3.11.

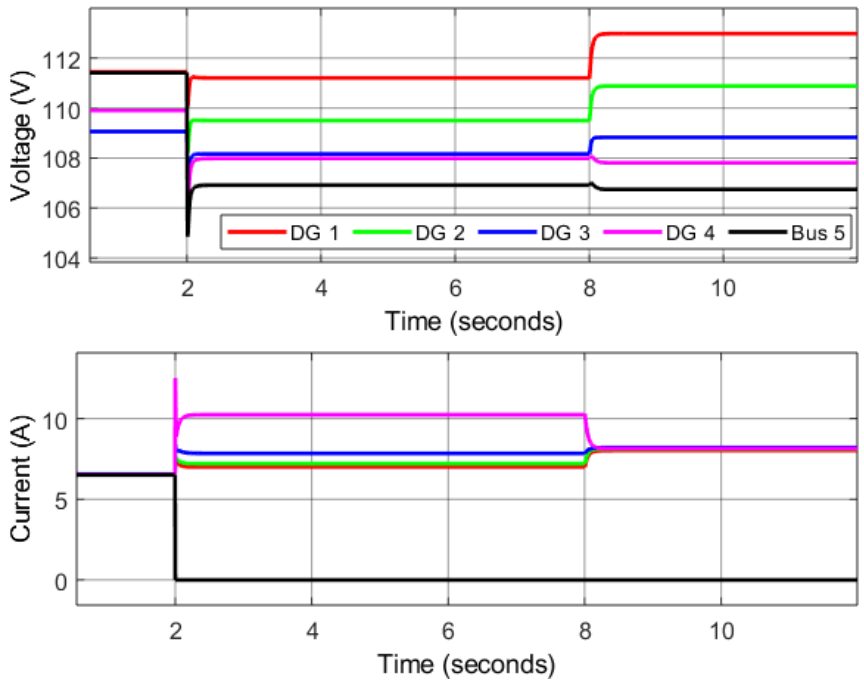

Figure 3.11: Variation of DG output voltages and currents in parallel DG system subjected to a generator disconnection (a) Voltages and (b) Currents. © [2020] IEEE.

At the point of DG disconnection, all the bus voltages undergo a voltage dip due to the loss of a generation source. Lowest voltage can be identified in bus 5, which is 104.8 V. Injected current at bus 5 goes to zero while other DGs show current overshoots. Maximum overshoot can be seen in DG 4 which increases its current up to 12.52 A. All the currents and voltages converge to a new equilibrium after 0.2s. Now the MG is controlled by pre-fault optimal droop coefficients which are not the optimal setting for the new system. Still, the pre-computed droop coefficients are capable of providing the required demand while protecting the system stability. Under the pre-fault optimal droop settings, the objective values were computed as, $f_1 = 1.63$ V, $f_2 = 10.33$ A and $f_3 = 43.63$ W. Optimal virtual resistances and corresponding reference voltages for the post-fault MG with 4 DGs were found as 0.231 Ω, 0.503 Ω, 0.623 Ω, 0.719 Ω and 114.83 V, 114.969 V, 113.942 V and 113.674 V respectively. After 6s from the fault, recomputed optimal droop coefficients with arbitrary reference voltages were assigned to the existing DGs. Thus, the objective values improve to $f_1 = 0.95$ V, $f_2 = 0.58$ A and $f_3 = 56.27$ W.

3.6.5 Microgrid with Constant Power Loads

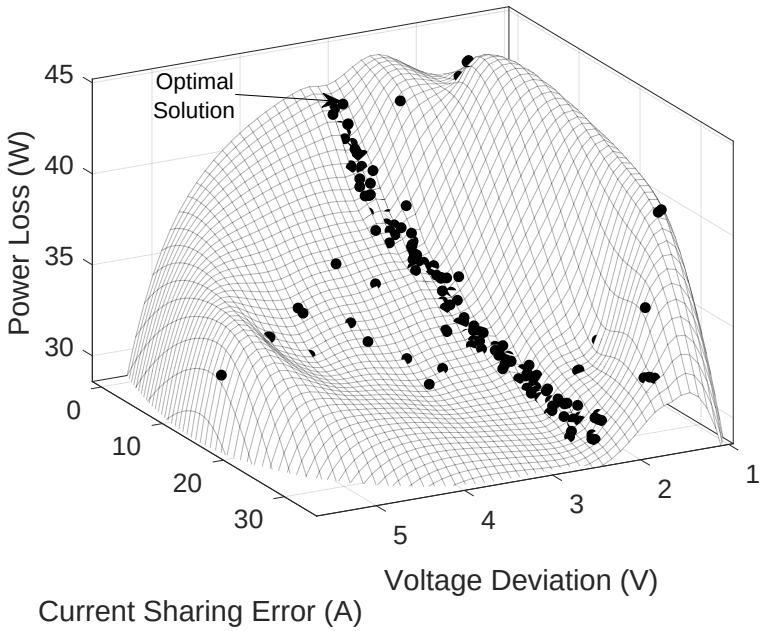

Figure 3.12: Pareto optimal front of parallel system with CPLs. © [2020] IEEE.

The effect of CPLs in the optimal droop coefficient computation is explored in this

section. Loads at bus six and bus nine in the parallel-connected system with equal line resistances were considered as CPLs with a power consumption of 500 W. Generated Pareto optimal front is depicted in Figure 3.12. The best compromise solution was found at $f_1 = 2.95$ V, $f_2 = 0.39$ A and $f_3 = 41.87$ W. In this test case, due to the effect of CPLs, voltage deviation error has been increased. Optimal virtual resistances were found as, 0.748 Ω, 0.999 Ω, 1.146 Ω, 0.989 Ω, 0.757 Ω and DG reference voltage was observed as 113.15 V. Further, the corresponding equivalent variable resistances of the CPLs at bus 6 and 9 were 23.05 Ω and 23.02 Ω respectively.

3.6.6 Parallel MG System with Unequal Line Resistances

In order to demonstrate the performances of the proposed concept with unequal distribution line resistances, a simulation test case was conducted. Table 3.2 summarizes the line resistances used to generate the results in Figure 3.13, while keeping all other parameters unchanged. In this case, the best cost solution for arbitrary DG reference voltages was found at $f_1 = 1.34$ V, $f_2 = 0.38$ A and $f_3 = 38.30$ W. System loss shows a lower value compared to the previous cases because some of the line resistances are now below 0.2 Ω. Voltage deviation and current sharing error increases due to the asymmetry in the network. The optimal virtual resistances were found as 0.6604 Ω, 0.7661 Ω, 0.8360 Ω, 0.8264 Ω and 0.5627 Ω. The optimal DG reference voltages for this test case were observed as, 113.69 V, 113.57 V, 113.36 V, 114.17 V, and 114.21 V.

Table 3.2: Distribution Line Resistances. © [2020] IEEE.

From Bus	To Bus	Value (Ω)	From Bus	To Bus	Value (Ω)
1	6	0.10	6	2	0.15
2	7	0.20	7	3	0.25
3	8	0.10	8	4	0.15
4	9	0.20	9	5	0.25

In order to compare the performances against the traditional droop coefficients, the parallel DG system with unequal line resistances was initialized with the traditional droop coefficients and at t = 1s those were changed to the optimal droop coefficients computed above. According to the results shown in Figure 3.13 and Figure 3.14, even with the different line

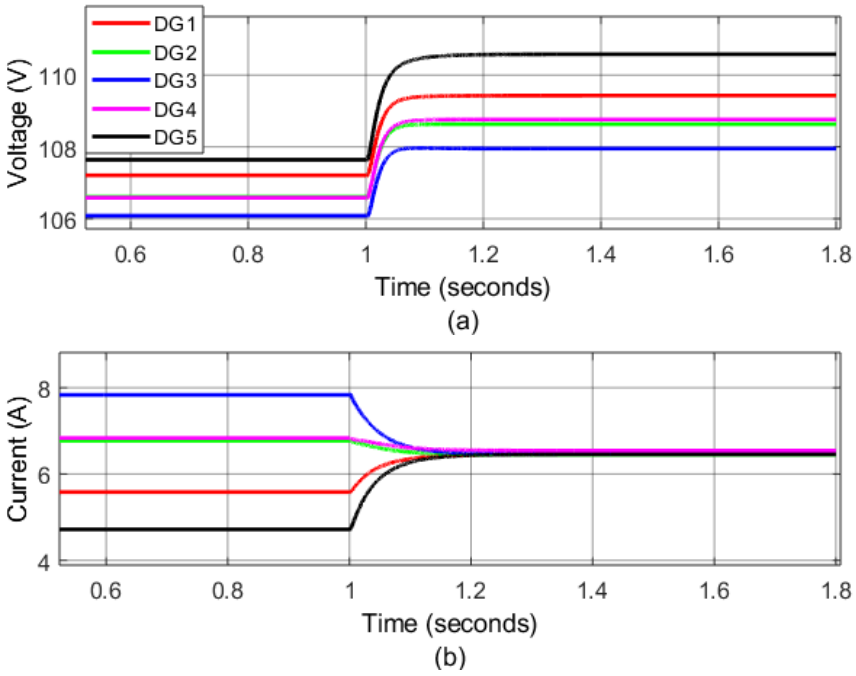

Figure 3.13: Variation of DG output voltages and currents in parallel DG system with unequal line resistances (a) Voltages and (b) Currents. © [2020] IEEE.

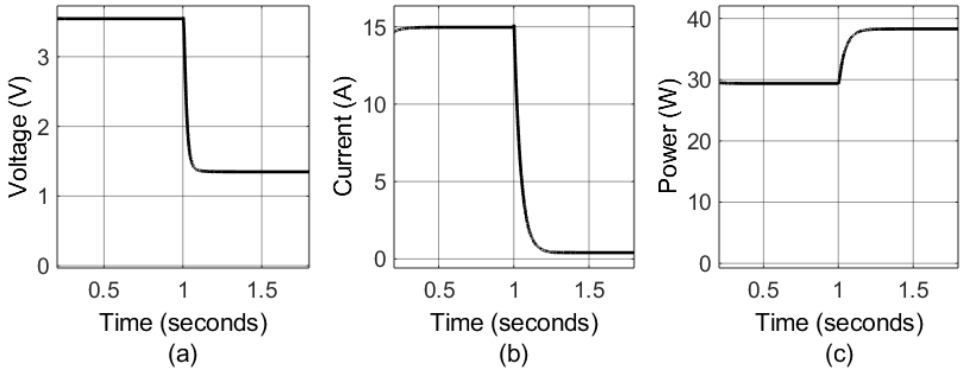

Figure 3.14: Variation of the objective functions in parallel DG system with unequal line resistances (a) f_1, (b) f_2 and (c) f_3. © [2020] IEEE.

resistances, the obtained optimal droop coefficients demonstrate excellent voltage regulation and current sharing error minimization. Comparative improvements in average voltage regulation and current sharing error minimization over the traditional droop coefficients were calculated as 62% and 97.2 % respectively.

3.6.7 Meshed MG System

This test case was carried out to compute the optimal droop coefficients of a meshed MG considering the IEEE 30 bus system given in [154]. Distribution line resistances and all the loads were considered as 0.2 Ω and 30 Ω respectively. Obtained Pareto optimal front with arbitrary DG reference voltages is shown in Figure 3.15. Considered unacceptable and acceptable satisfactory values for the best compromise solution were $f_1^{max} = 7$ V, $f_2^{max} = 25$ A, $f_3^{max} = 280$ W, $f_1^{min} = 5$ V, $f_2^{min} = 15$ A and $f_3^{min} = 250$ W. Best cost solution was found as $f_1 = 2.15$ V, $f_2 = 13.34$ A and $f_3 = 299.9$ W. The obtained optimal virtual resistances were, 0.275 Ω, ,0.314 Ω, 0.270 Ω, 0.290 Ω, 0.343 Ω, 0.376 Ω. The optimal reference voltages were found as, 114.87 V, 114.86 V, 114.95 V, 113.90 V, 114.80 V, 114.31 V respectively.

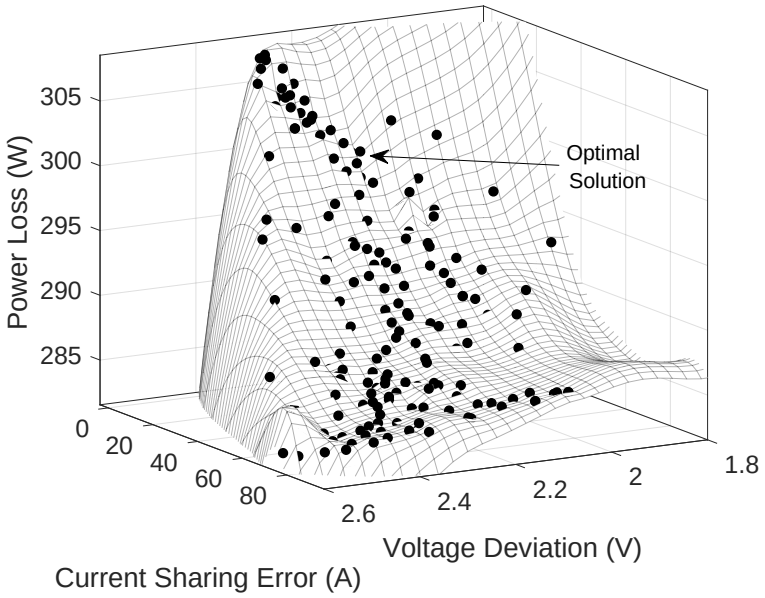

Figure 3.15: Pareto optimal front of meshed system. © [2020] IEEE.

A Comparison between the traditional and optimal droop in the mesh MG was performed and results are given here. In the mesh system, traditional virtual resistances were set to 0.4 Ω for all the DGs based on their allowable maximum output voltages deviation and maximum output currents given above. The mesh DG system was initialized with the traditional droop coefficients and at t = 1s those were changed to optimal droop gains with arbitrary reference voltages. In the traditional case, steady-state DG voltages are below the nominal system voltage and the currents are distributed between 12.22 A and 7.95 A

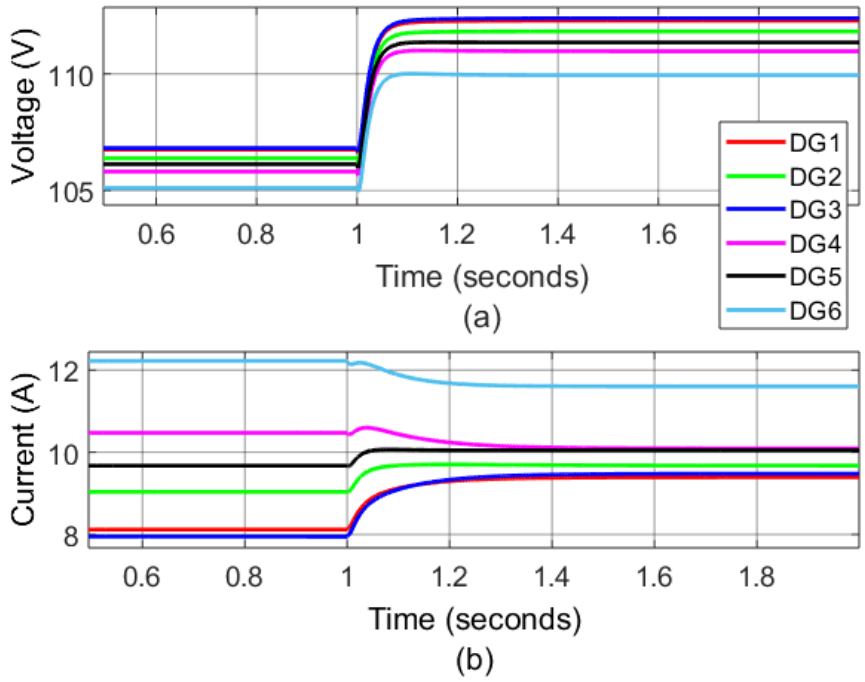

Figure 3.16: Variation of DG output voltages and currents in mesh DG system (a) Voltages and (b) Currents. © [2020] IEEE.

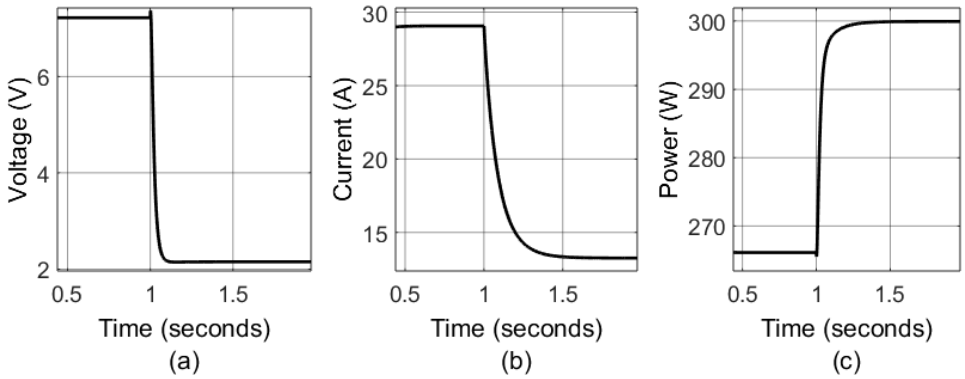

Figure 3.17: Variation of the objective functions in mesh DG system (a) f_1, (b) f_2 and (c) f_3. © [2020] IEEE.

as shown in Figure 3.16. With the optimal droop, voltages are restored to maintain the overall system voltage close to the nominal value. DG output currents show close variation than the traditional case where the distribution is now between 11.6 A and 9.48 A. Since the mesh system is not symmetrical, current sharing error minimization is not good as in the parallel system. If high priority is given to the current sharing error minimization, a

better result can be obtained. However, it will result in higher system losses and poor voltage regulation. According to Figure 3.17, objective values of the traditional case are $f_1 = 7.22$ V, $f_2 = 29.06$ A and $f_3 = 266.1$ W. Even though a high loss is observed with the optimal droop, the objectives f_1 and f_2 gained 70.2% and 54.1% improvements over the traditional method.

3.7 Experimental Validation

The effectiveness and applicability of the optimal droop coefficients computed by the proposed method were experimentally validated on the test bench shown in Figure 3.18. The experimental test bench contains the DS1104 controller card, CP1104 I/O board, MOSFET converter system and the bus system. The upper half of the parallel-connected bus system shown in Figure 3.6 was considered as the test bus system with 3 DGs and two loads at 30 Ω and 20 Ω operated in 30 V nominal bus voltage with 1 Ω distribution line resistances. Upper and lower bounds of the virtual resistances were chosen as 0.3 Ω and 1.5 Ω while the upper and lower reference voltage bounds were set to 28 V and 32 V. Further, optimization constraints were considered as, $V_i > 0.95V_n$, $\delta V_{max} = 1$ V, and $I_{max} = 2$ A. Obtained optimal virtual resistances of DG1, DG2 and DG3 were 0.547 Ω, 0.722 Ω, and 0.734 Ω. The optimal reference voltages were found at 30.92 V, 30.43 V, and 30.62 V respectively. With these droop coefficients, the MG was controlled by the developed state feedback controller. The experimental setup details are summarized in Table 3.3.

In the presented experimental test setup, the update laws were programmed in the MATLAB/Simulink environment. The feedback signals from the current and voltage sensors were taken into the computer through the dSPACE DS1104 controller card and CP1104 I/O board. Some of the voltage and current information were measured directly from the inbuilt test points in the *Vishay* power electronic drive board. To get the other voltage feedbacks, Tektronix P5200A differential probes were used. Further, Tektronix TCP A300 current amplifiers combined with TCP305A current probes have been used to get the output current information of each DG. Generated duty cycles were passed through the PWM generator and the corresponding PWM switching signals were fed into the MOSFET converters through the slave I/O PWM DBUS connector in the dSPACE CP1104 I/O board.

Initially, the system was controlled by the traditional droop and then the coefficients were changed to optimal droop. The output current and voltage waveforms of the DGs are

Table 3.3: Parameters of the Experimental Setup. © [2020] IEEE.

Parameter	Value
Traditional R_D	0.5 Ω
Traditional V_r	30 V
Switching frequency	16 kHz
L_k	10 mH
E_k	20 V
C_k	DG1 & DG3 - 3.4 mF, DG2 - 2.8 mF

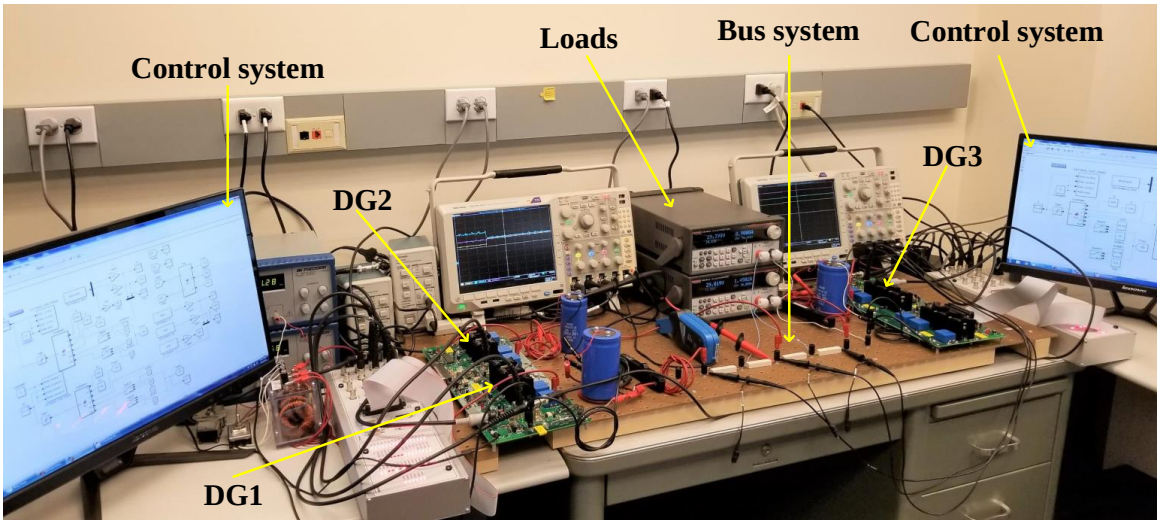

Figure 3.18: Experimental test bench. © [2020] IEEE.

shown in Figure 3.19 and Figure 3.20. According to Figure 3.19, DG output currents are not equal and under the optimal droop, they converge to a closer value around 0.8 A. The DG output voltages show a small increment as in Figure 3.20. Experimental costs of the three objectives under the optimal droop coefficients were $f_1 = 0.43$ V, $f_2 = 0.08$ A and $f_3 = 1.28$ W. The three objective values of the traditional droop were $f_1 = 0.98$ V, $f_2 = 0.93$ A and $f_3 = 0.82$ W. Since the optimal solution of the droop coefficients was extracted to have the best possible voltage regulation and current sharing, a slight increment in losses can be observed. However, with the optimal droop, the improvement in f_1 and f_2 over the traditional droop are 56.21% and 91.40% respectively.

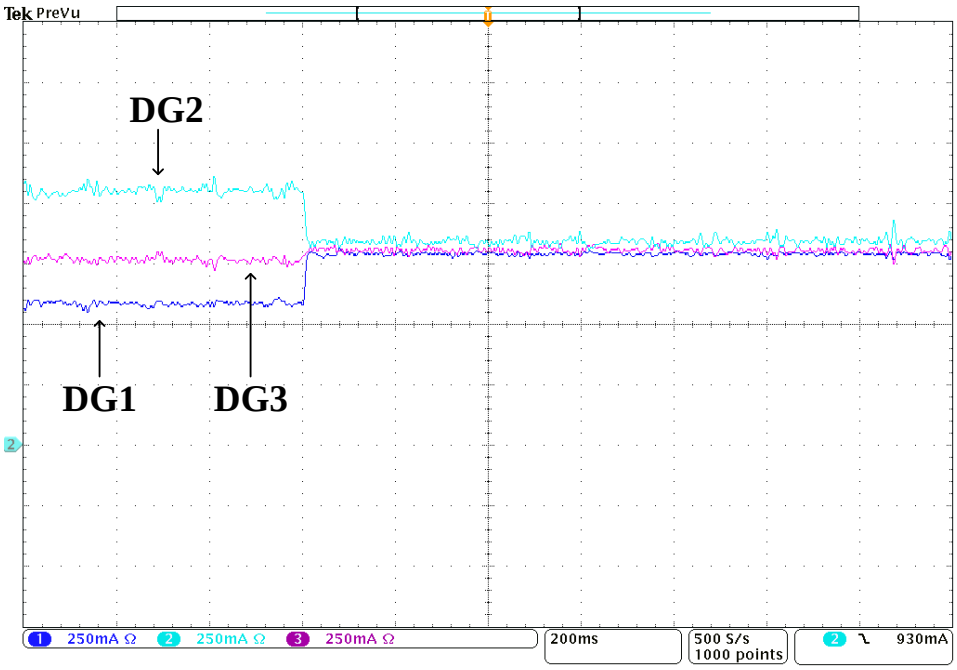

Figure 3.19: Experimental current variation. © [2020] IEEE.

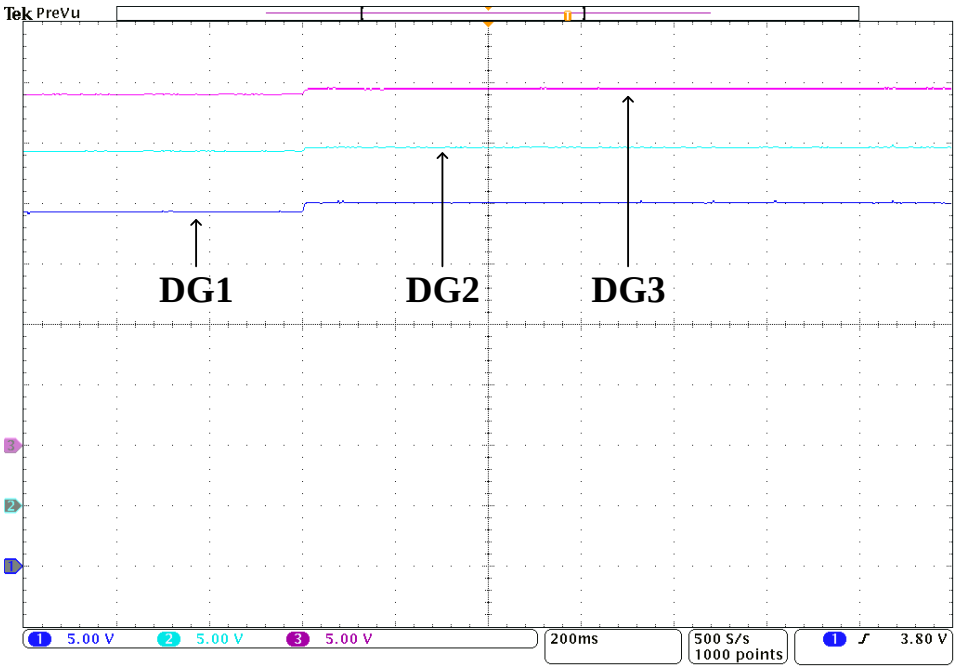

Figure 3.20: Experimental voltage variation. © [2020] IEEE.

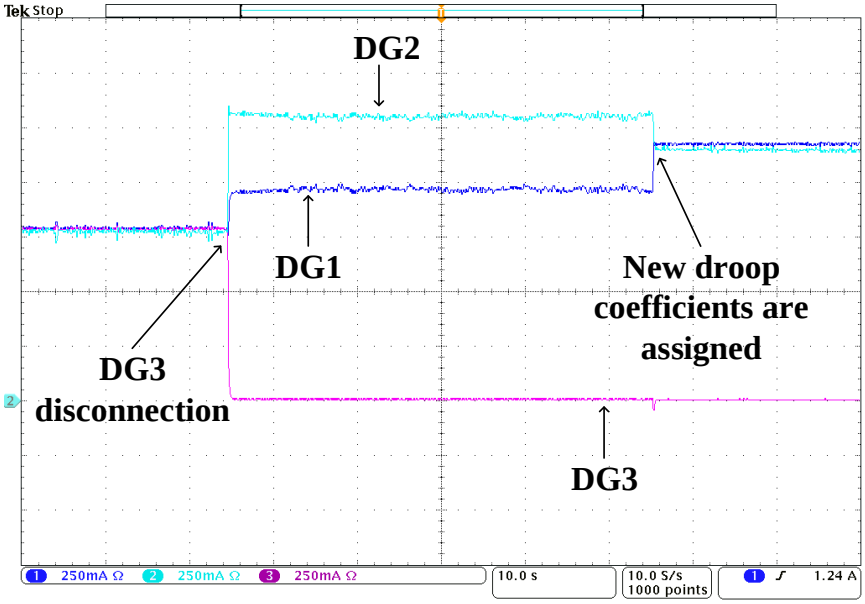

Figure 3.21: Experimental current variation subjected to a DG disconnection. © [2020] IEEE.

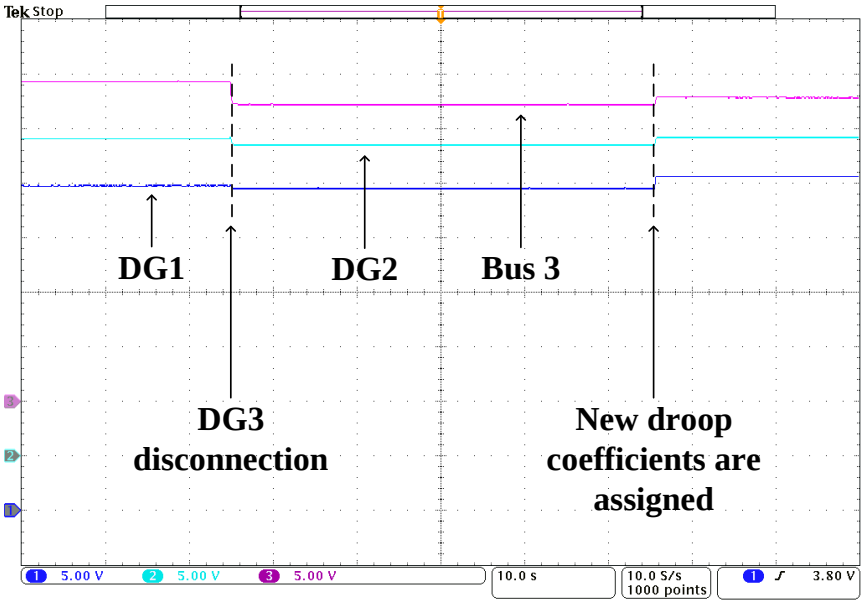

Figure 3.22: Experimental voltage variation subjected to a DG disconnection. © [2020] IEEE.

Control action and stability of the proposed concept under a DG disconnection was experimentally verified. Initially, the MG was controlled by the pre-fault optimal droop

found in the first experimental test case. Then, the DG3 was disconnected from the MG and hence it becomes a load bus with no load connected to it. The remaining DGs were controlled with the pre-fault optimal droop until the post-fault optimal droop coefficients are available and assigned. Variations in the currents and voltages are shown in Figure 3.21 and Figure 3.22. According to the results, the control and stability of the MG are protected with the pre-fault droop even one DG is disconnected. During this period, the experimental objective values were computed as, $f_1 = 1.8$ V, $f_2 = 0.325$ A and $f_3 = 1.71$ W. After 6s from the DG disconnection, post-fault optimal droop coefficients were assigned. Obtained post-fault optimal virtual resistances and reference voltages of DG1 and DG2 were 0.301 Ω, 0.598 Ω, 31.94 V, and 30.87 V respectively. With the post-fault optimal droop, improvements in current sharing and voltage regulation can be observed. Experimental objective values for the post-fault optimal droop were calculated as $f_1 = 1.11$ V, $f_2 = 0.02$ A and $f_3 = 2.96$ W.

3.8 Conclusion

A MOO based optimal droop coefficient computation methodology for DGs in islanded DCMG was proposed in this section. Overall system voltage regulation, current sharing error minimization, and total system active power loss minimization were taken as conflicting objectives. Elitist non dominated sorting genetic algorithm (NSGA II) was utilized to obtain the Pareto optimal front in the objective space and a fuzzy membership function was employed to obtain the best compromise solution. Simulations were carried out for both the parallel-connected system and the meshed system. In addition, a state feedback linearized controller was utilized to facilitate the control actions under the optimal droop relationships. Both simulation and experimental results were presented with the developed feedback controller to demonstrate the effectiveness of the proposed optimal droop coefficients over the traditional ones. According to the results, it can be inferred that the droop coefficients generated by the proposed MOO approach have superior steady-state responses and better performance compared to the traditional droop coefficients. The inclusion of a dynamic MOO technique to make the droop coefficient calculation process online and replace the controller to an adaptive controller would be exciting future directions of this work. The inclusion of a dynamic MOO technique allows to adaptively change the droop constants along with solar radiation which has numerous advantages in renewable-based MGs.

CHAPTER IV

DROOP FREE OPTIMAL FEEDBACK CONTROL OF DISTRIBUTED GENERATORS IN ISLANDED DC MICROGRIDS

4.1 Major Objectives

A droop free, approximate optimal feedback control methodology is proposed in this chapter for islanded DCMGs. Mitigation of major drawbacks in traditional proportional-integral (PI) based droop control is the main objective of the proposed approach. Concurrent learning-based feedback optimal control methodology is employed to compute the constraint input of each distributed generator (DG) in the MG. Unlike other feedback optimal controllers, the proposed methodology for DCMG possesses convergence of the unknown wights to a neighborhood of the optimal weights without the persistence of excitation (PE). Simulation and experimental results are presented to demonstrate the proposed concept considering 7 bus system and 5 bus test systems respectively. The major contributions of this section are summarized below.

1. The development of a droop free control algorithm to replace conventional droop mechanism in DGs in islanded DCMGs.

2. A novel, real-time feedback optimal control algorithm to achieve the optimal dynamic response of the droop free DGs.

In the traditional droop methods, the sources in the MG are controlled through predefined droop characteristics called the linear droop relationships [25, 40]. Here, the DG output

voltage is changed according to the measured output current based on the droop relationship. Conversely, online droop free methods predict the source behavioral characteristics based on the instantaneous measurements of the system and do not rely on predefined offline trajectories or surfaces. In the proposed droop free approach, instead of tampering the output voltage, the DG input current is changed according to the measured output current while keeping the output voltage at the nominal value. This control objective is realized in an optimal manner to gain the best possible transient performances subjected to any disturbance in the system. The proposed real-time optimal feedback control algorithm is based on the infinite horizon optimal control architecture. Further, this algorithm is derived from the concurrent reinforcement learning (RL) adaptive/approximate dynamic programming (ADP) with control bounds. The main advantages of this feedback optimal control algorithm compared to the existing methods in DCMG control are,

1. No offline training is required. Parameter convergence is achieved online.
2. Does not require PE condition to guarantee the parameter convergence like most of the other existing feedback optimal controllers.
3. Bounded control signal in the allowable control space.
4. Fast parameter convergence.

This novel control algorithm is introduced to replace the traditional PI-based control loops in the droop controller. Introducing the droop free algorithm together with the proposed optimal feedback control algorithm, the following advantages are obtained compared to the existing conventional PI-based droop control.

1. Higher voltage quality through improved voltage regulation in individual DGs and overall DCMG.
2. Mitigation of poor transient performances.
3. Low control burden by minimum duty cycle variations.
4. Fast response to sudden disturbances.

In the modeling, each DG is modeled as a control affine dynamical system and optimal duty cycles for each DG are generated by a constrained input ADP method. Two RL based adaptive tuning algorithms are introduced to learn the unknown parameters in the optimal value function and the controller by simulation of experience via Bellman Error (BE) extrapolation which does not require PE to guarantee the parameter convergence. Main findings of this chapter are published in [156].

4.2 Dynamic Modeling of Distributed Generators

In this chapter, intermediate PEI of each DG is assumed to be boost topology as shown in Figure 4.1. A combination of the input voltage source, PEI and the controller is referred to as a DG. We are not considering the dynamics of the input power source in this chapter as it is a different research topic. In control design for DGs, it is customary to assume the input power source provides a constant voltage to the PEI [25, 41]. Hence, all the input sources are assumed to be constant DC voltage sources. Even though the input voltage is assumed to be constant in the modeling to ease the computational burden, the proposed control algorithm is capable of compensating input voltage disturbances. Simulation results are presented to demonstrate the adaptability against the input voltage disturbances later in the chapter. Further, we assume that the PEI is closely located to the main DC bus and hence the line resistance between the main DC bus and output of the PEI can be neglected.

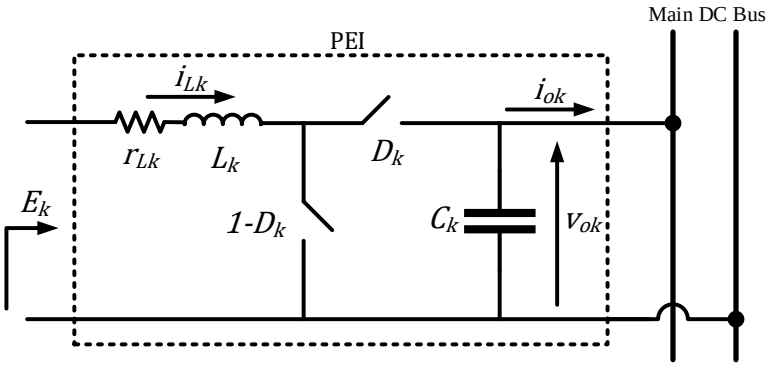

Figure 4.1: Schematic diagram of the boost PEI. © [2020] IEEE.

Suppose N number of DGs exist in the set $\mathcal{G}$. Then, the dynamic model of the k^{th}

DG ($k \in \mathcal{G}$) can be represented as,

$$L_k \dot{i}_{Lk}(t) = E_k - \mathcal{D}_k v_{ok}(t) - r_{Lk} i_{Lk}(t) \tag{4.1}$$

$$C_k \dot{v}_{ok}(t) = \mathcal{D}_k i_{Lk}(t) - i_{ok} \tag{4.2}$$

where, the two states i_{Lk}, v_{ok} are the inductor current and output voltage, control input is the duty cycle $\mathcal{D}_k$, i_{ok} is the instantaneous output current and L_k, r_{Lk}, C_k, E_k are the inductance of the inductor, the resistance of the inductor, the capacitance of the capacitor and the input voltage of the DG. In the modeling, the output current assumed to be time-independent and at any given time controller attempts to adjust the duty cycle to supply the measured instantaneous output current. Hence, the desired duty cycle is a function of the instantaneous output current. Suppose the desired output voltage is x_{2d} which is the nominal system voltage, the desired duty cycle can be obtained by (4.1) and (4.2) as,

$$\bar{\mathcal{D}}_k = \frac{E_k + \sqrt{E_k^2 - 4x_{2d} i_{ok} r_{Lk}}}{2x_{2d}} \tag{4.3}$$

Assumption 1 : Every DG has a maximum generation capacity which limits its output current. The bound of k^{th} DG instantaneous output current is given by,

$$i_{ok} < \frac{E_k^2}{4x_{2d} r_{Lk}} \; ; \quad \forall k \in \mathcal{G} \tag{4.4}$$

This assumption ensures the existence of a real solution to the desired duty cycle in (4.3).

Defining the error system states as $x_{1k} = i_{Lk}(t) - i_{ok}/\bar{\mathcal{D}}_k$, $x_{2k} = v_{ok}(t) - x_{2d}$, relative control as $u_k = \mathcal{D}_k - \bar{\mathcal{D}}_k$ and using (4.1)-(4.3), the error system dynamics of the k^{th} DG can be obtained in control affine form as,

$$\dot{x}_k = f_k(x_k) + g_k(x_k) u_k \tag{4.5}$$

where, the concatenate state $x_k = \begin{bmatrix} x_{1k} & x_{2k} \end{bmatrix}^T$, $f_k(x_k)$ and $g_k(x_k)$ are given by,

$$f_k(x_k) = \begin{bmatrix} \frac{-r_{Lk}x_{1k} - \bar{\mathcal{D}}_k x_{2k}}{L_k} \\ \frac{\bar{\mathcal{D}}_k x_{1k}}{C_k} \end{bmatrix}; g_k(x_k) = \begin{bmatrix} \frac{-(x_{2k} + x_{2d})}{L_k} \\ \frac{x_{1k} + i_{ok}/\bar{\mathcal{D}}_k}{C_k} \end{bmatrix} \tag{4.6}$$

Since the control duty cycle is only allowed to use the values in $\mathcal{D}_k \in (0, 1)$, relative controller can only pick values in the set $u_k \in (-\bar{\mathcal{D}}_k, 1 - \bar{\mathcal{D}}_k)$. In order to make the upper and lower bounds of the controller even such that $|u_k| \leq \bar{u}_k$, control bound is selected as $\bar{u}_k = min\{\bar{\mathcal{D}}_k, 1 - \bar{\mathcal{D}}_k\}$. Even though this assignment restricts the control space more than it supposed to be, alternatively it makes the constrained input control problem much simpler to solve and it always ensures the actual duty cycle remains in the set $(0, 1)$.

Now the goal is to find the optimal feedback control actions which drive the error system states given by (4.5) to zero. The next section explains how to achieve this goal online in the state feedback form.

4.3 Infinite Horizon Approximate Optimal Control of Distributed Generators

4.3.1 Problem Statement

Once the system dynamics are constructed as in (4.5) and (4.6) with the control input constraint explained in previous section, the goal is to solve the infinite horizon optimal control problem. Consequently, the objective is to find a control signal $(u_k^*(x_k))$ which minimizes the performance index,

$$J_k(x_k, u_k) = \int_{t_0}^{\infty} r_k(x_k(\tau), u_k(\tau))d\tau \tag{4.7}$$

such that,

$$u_k^*(x_k) = \underset{u_k(\tau) \in \Omega_k^u | \tau \in \mathbb{R}_{\geq t}}{\arg\min} \int_t^{\infty} r_k(x_k(\tau), u_k(\tau))d\tau \tag{4.8}$$

where, $\Omega_k^u = \{u_k | u_k \in \mathbb{R}, |u_k(x_k)| \leq \bar{u}_k\}$. The instantaneous cost in (4.7) and (4.8) is defined as,

$$r_k(x_k, u_k) = Q_k(x_k) + U_k(u_k) \tag{4.9}$$

where, $Q_k(x_k)$ is a positive definite function and $U_k(u_k)$ is a positive definite integral function. Since the goal is to regulate the error system states to zero, the quadratic state cost of

the form $x_k^T P_k x_k$ is selected for $Q_k(x_k)$. Here, P_k is a positive definite symmetric matrix with appropriate dimension. In order to satisfy the control input constraint, following non-quadratic penalty function is employed for $U_k(u_k)$ [157, 158].

$$U_k(u_k) = 2R_k\bar{u}_k \int_0^{u_k} \tanh^{-1}(\zeta/\bar{u}_k)d\zeta \tag{4.10}$$

where, R_k is a positive constant.

The performance index is the objective function that the control agent wishes to maximize or minimize. This dissertation considers the integral state and control cost from any initial state to infinity. This particular problem is called the infinite horizon optimal control problem. The instantaneous state cost is the difference between the current state and the desired state at that time instance while the instantaneous control cost is formulated as a nonlinear function of the difference between current control and desired control at that time instance. The integral summation of these state and control errors from the initial time to the infinity makes the performance index and the goal is to minimize the cost of errors. Since this is a performance index of the cost that contains state and control errors, we want to minimize it to reach the desired state and control. To minimize the performance index, the only explicit adjustable variable in hand is the control signal. The control variable in this problem is the control duty cycle. It directly tied to the state through system dynamics (4.1) and (4.2). Since the performance index comprises of system state and it has nonlinear control error function, the control signal directly affects the performance index. Hence, by properly adjusting the control signal, the performance index can be minimized.

Closed form solution to the derived optimal control problem is characterized by the optimal value function given by [128],

$$V_k^*(x_k) = \min_{u_k(\tau)\in\Omega_k^u|\tau\in\mathbb{R}_{\geq t}} \int_t^\infty r_k(x_k(\tau), u_k(\tau))d\tau \tag{4.11}$$

The optimal value function satisfies the Hamilton Jacobi Bellman (HJB) equation [128] such that,

$$\min_{u_k\in\Omega_k^u} \left[\nabla V_k^*(x_k)(f_k(x_k) + g_k(x_k)u_k(x_k)) + r_k(x_k, u_k)\right] = 0 \tag{4.12}$$

where, ∇ is the gradient operator with respect to x_k and $H(x_k, u_k) = \nabla V_k^*(x_k)(f_k(x_k) +$

$g_k(x_k)u_k(x_k)) + r_k(x_k, u_k)$ is the Hamiltonian. If the optimal controller $(u_k^*(x_k))$ exists, according to (4.12), the HJB equation can be shown as,

$$\nabla V_k^*(x_k)(f_k(x_k) + g_k(x_k)u_k^*(x_k)) + r_k(x_k, u_k^*(x_k)) = 0 \tag{4.13}$$

with the initial condition $V_k^*(0) = 0$. The optimal control law which satisfies the HJB equation can be obtained by differentiating the Hamiltonian with respect to u_k as,

$$u_k^*(x_k) = -\bar{u}_k \tanh\left[\frac{1}{2R_k\bar{u}_k}\nabla V_k^*(x_k)g_k(x_k)\right] \tag{4.14}$$

Since the hyperbolic tangent function is a continuous, one to one bounded function such that $|\tanh(\cdot)| \leq 1$, the optimal control policy derived in (4.14) satisfies $|u_k| \leq \bar{u}_k$. Further, the second derivative of the Hamiltonian can be shown as, $2R_k\bar{u}_k\nabla_{u_k}(\tanh^{-1}(u_k/\bar{u}_k))$. Since the hyperbolic tangent function is strictly monotonically increasing, the second derivative is positive [55]. This implies $u_k^*(x_k)$ given in (4.14) minimizes the Hamiltonian.

Once the optimal control policy $u_k^*(x_k)$ is obtained, the optimal duty cycle of the k^{th} DG $(\mathcal{D}_k^*)$ can be computed. This optimal duty cycle is a state feedback controller which is a function of the DG's optimal value function. To obtain the value function, one needs to substitute the optimal control (4.14) in (4.13) and solve the HJB equation for $V_k^*(x_k)$. Then $V_k^*(x_k)$ can be substituted back in (4.14) to obtain $u_k^*(x_k)$ and subsequently $\mathcal{D}_k^*$. However, obtaining an exact analytical solution to the HJB equation is generally infeasible. Hence, methods have been developed to obtain an approximate solution by employing ADP techniques. In RL based online ADP methods, the optimal value function is approximated by a NN and the unknown weights of the approximate value function are updated to minimize the approximation error called the Bellman Error (BE) [53, 55]. In this chapter, two linear in the parameter (LIP) NNs are utilized to successively approximate the optimal value function and the optimal feedback control law as described in the next section. In the subsequent analysis, the indicator k is dropped for the notational brevity and the procedure is similar for all the DGs in $\mathcal{G}$.

4.3.2 Value Function Approximation

NNs are an effective method for unknown function approximation on prescribed compact sets [159]. The universal approximation property of NNs can be utilized to synthesize the optimal value function in a compact set $\chi \subset \mathbb{R}^2$ as,

$$V^*(x) = W^T\sigma(x) + \epsilon(x) \tag{4.15}$$

where, $W \in \mathbb{R}^L$ is the vector of ideal NN weights bounded by a known constant such that $\|W\| \leq \bar{W}$, $L \in \mathbb{N}$ is the number of neurons, $\sigma(x) : \mathbb{R}^2 \to \mathbb{R}^L$ is a continuously differentiable activation function having the properties $\sigma(0) = 0$ and $\nabla\sigma(0) = 0$, and $\epsilon(x)$ is the function reconstruction error which is bounded in the sense $\sup_{x\in\chi} |\epsilon(x)| \leq \bar{\epsilon}$ and $\sup_{x\in\chi} |\nabla\epsilon(x)| \leq \bar{\epsilon}'$ [55]. With this NN representation, the optimal controller can be derived as,

$$u^*(x) = -\bar{u}\tanh\Big[\frac{1}{2R\bar{u}}\Big(W^T\nabla\sigma(x) + \nabla\epsilon(x)\Big)g(x)\Big] \tag{4.16}$$

Since the optimal wight vector W is unknown, an estimate set of weights are assigned to approximate the value function and the optimal control law as,

$$\hat{V}(x, \hat{W}_c) = \hat{W}_c^T\sigma(x) \tag{4.17}$$

$$\hat{u}(x, \hat{W}_a) = -\bar{u}\tanh\Big[\frac{1}{2R\bar{u}}\hat{W}_a^T\nabla\sigma(x)g(x)\Big] \tag{4.18}$$

where, $\hat{W}_c \in \mathbb{R}^L$ and $\hat{W}_a \in \mathbb{R}^L$ are called the critic and actor weights which are the estimates of actual weights W. Replacing the optimal value function and optimal control in (4.13) by these estimates, the BE can be expressed as,

$$\delta(x, \hat{W}_c, \hat{W}_a) = \nabla\hat{V}(x, \hat{W}_c)\Big(f(x)+g(x)\hat{u}(x, \hat{W}_a)\Big)+Q(x)+2R\bar{u}\Big[\hat{u}(x, \hat{W}_a)\tanh^{-1}\Big(\frac{\hat{u}(x, \hat{W}_a)}{\bar{u}}\Big) + \frac{\bar{u}}{2}ln\Big(1 - \Big(\frac{\hat{u}(x, \hat{W}_a)}{\bar{u}}\Big)^2\Big)\Big] \tag{4.19}$$

The objective is to design an adaptive tuning algorithm to simultaneously adjust the weight estimates to minimize the BE as explained in the next subsection. Eventually, the decision variables of the transient optimization problem become the unknown weights in the actor

and critic NNs. Utilizing two sets of weights to estimates the same unknown optimal weights makes the problem less complex. Further, with this modification, critic weights appear linearly in the BE which allows the least-squares (LS) based update law [52, 55].

4.3.3 Model Based Reinforcement Learning

RL is learning itself on how to proceed and what actions to take in order to gain reward by maximizing or minimizing a given performance index [160]. The learner is given a performance index and a possible pool of actions or an action space, but not told which actions to take. Therefore, the learning agent must explore and decide which actions yield the most reward by utilizing them. Depending on the rewards gained by current and past actions, the learning agent decides the future actions. Further, the goal or the performance index must interrelate to the state space in some way so that the learning agent can sense the variations in the state and gained reward as consequences of its actions. In this chapter, the learner is trying to minimize the BE by tuning the actor and critic weights.

Online RL implies it works in real-time without any human interaction or prior information. This type of learning process operates in real-time, and it is an unsupervised like learning mechanism which does not require any offline tuning. The algorithm seeks the optimal value function along the system trajectories as it operates, and it tries to find the control signal which minimizes the considered performance index. This means it uses the information gain by the state space to tune the unknown weights in the value function and control signal. If the dynamical system changes due to a load change or any other disturbance, then the operating conditions and eventually the state trajectories will change. Then, the weight tuning laws will adjust accordingly to find out the new weights corresponding to the current system in real-time.

Two update laws are employed here to learn the optimal weights in the value function by adjusting the actor and critic weights. In online RL based update laws, these wights are updated through the observed data along the system trajectories. The traditional online learning algorithms require sufficient richness in the observed data to converge the weight estimates to a neighborhood of the optimal weights which is characterized by the PE condition. Usually, a probing noise is added to the controller to achieve PE which is undesirable in DCMG control. Therefore, this chapter employs a concurrent learning-based adaptive learning

algorithm that does not require PE for convergence [161]. The methodology discussed in this work utilizes the system model to extrapolate the BE to unexplored areas of the state space and use that information as a gained experience for learning.

An update law based on the LS with forgetting factor is employed to tune the critic gains as [52, 55, 162],

$$\dot{\hat{W}}_c(t) = -k_{c1}\Gamma(t)\frac{\phi(t)}{\rho(t)}\delta(t) - \frac{k_{c2}}{M}\Gamma(t)\sum_{i=1}^{M}\frac{\phi_i(t)}{\rho_i(t)}\delta_i(t) \tag{4.20}$$

$$\dot{\Gamma}(t) = \Big(\beta\Gamma(t) - k_{c1}\Gamma(t)\frac{\phi(t)\phi^T(t)}{\rho^2(t)}\Gamma(t) - \frac{k_{c2}}{M}\Gamma(t)\sum_{i=1}^{M}\frac{\phi_i(t)\phi_i^T(t)}{\rho_i^2(t)}\Gamma(t)\Big)\mathbb{1}_{\|\Gamma(t)\|\leq\bar{\Gamma}} \tag{4.21}$$

where, $\phi(t) = \nabla\sigma(x)\Big(f(x) + g(x)\hat{u}(x,\hat{W}_a)\Big) \in \mathbb{R}^L$ is the regressor vector, $\rho(t) = 1 + \nu\phi^T(t)\Gamma(t)\phi(t) \in \mathbb{R}$ is the normalizing term, $\Gamma(t) \in \mathbb{R}^{L\times L}$ is the time varying LS gain matrix, $\mathbb{1}$ is the indicator function, $\bar{\Gamma}$ is the saturating upper bound of $\Gamma(t)$, k_{c1}, k_{c2}, ν are positive constant gains and β is the forgetting factor [52]. Further, $\phi_i(t) = \nabla\sigma(x_i)\Big(f(x_i) + g(x_i)\hat{u}(x_i,\hat{W}_a)\Big) \in \mathbb{R}^L$, and $\rho_i(t) = 1 + \nu\phi_i^T(t)\Gamma(t)\phi_i(t) \in \mathbb{R}$ are the regressor and normalizing term evaluated at the predefined set of points x_i and $\delta_i(t) = \delta(x_i,\hat{W}_c,\hat{W}_a)$ is the BE extrapolated to those points. In the modeling, it is assumed that the predefined points satisfy the following rank condition [55].

Assumption 2 : There exists a finite set of fixed points $\{x_i \in \mathbb{R}^2 | i = 1,\ldots,M\}$ such that $\forall t \in \mathbb{R}_{\geq 0}$,

$$0 < \underline{c} \triangleq \frac{1}{M}\left(\inf_{t\in\mathbb{R}_{\geq 0}}\left(\lambda_{min}\left\{\sum_{i=1}^{M}\frac{\phi_i(t)\phi_i^T(t)}{\rho_i^2(t)}\right\}\right)\right) \tag{4.22}$$

Based on the stability analysis the actor weights are updated as,

$$\dot{\hat{W}}_a(t) = -k_{a1}\Big(\hat{W}_a(t) - \hat{W}_c(t)\Big) + \bar{u}\Big(k_{c1}\tanh(\hat{D}_a)\frac{\phi(t)}{\rho(t)}G_\sigma^T + \frac{k_{c2}}{M}\sum_{i=1}^{M}\tanh(\hat{D}_{ai})\frac{\phi_i(t)}{\rho_i(t)}G_{\sigma i}^T\Big)\hat{W}_c(t) \tag{4.23}$$

where, $G_\sigma = \nabla\sigma(x)g(x)$, $G_{\sigma i} = \nabla\sigma(x_i)g(x_i)$, $\hat{D}_a = G_\sigma^T\hat{W}_a/2R\bar{u}$ and $\hat{D}_{ai} = G_{\sigma i}^T\hat{W}_a/2R\bar{u}$. Alternatively a projection based algorithm can also be implemented to tune the actor weights in the sense that $\dot{\hat{W}}_a(t) = proj\Big(-k_{a1}(\hat{W}_a(t) - \hat{W}_c(t))\Big)$ [162]. Based on these tuning laws,

estimate of the optimal controller can be obtained using (4.18) and then the approximate optimal duty cycle for each DG can be recovered as,

$$\hat{\mathcal{D}}(x, \hat{W}_a) = \hat{u}(x, \hat{W}_a) + \bar{\mathcal{D}} \tag{4.24}$$

The complete process is summarized in Figure 4.2.

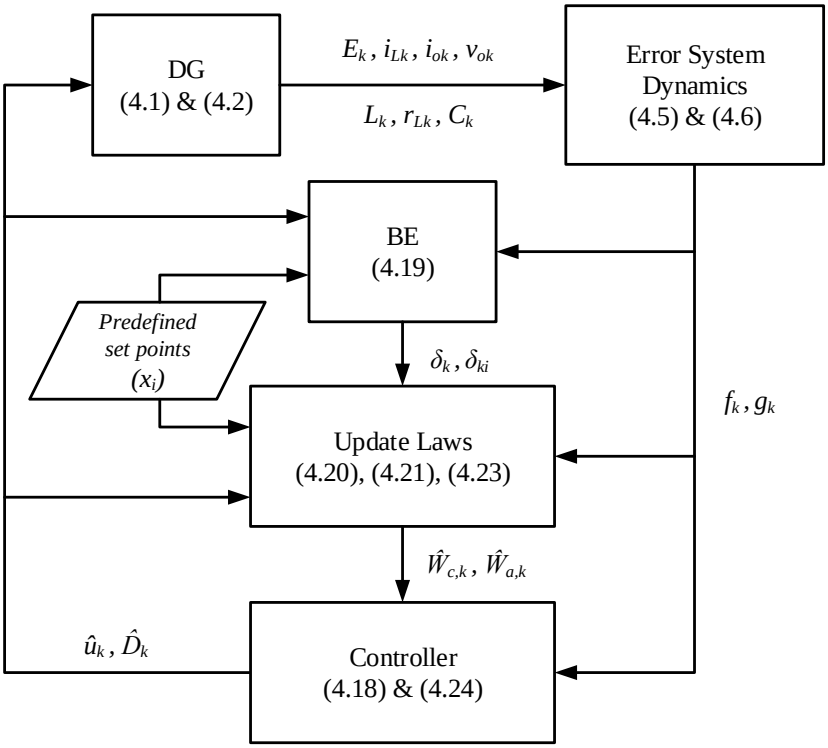

Figure 4.2: Model based approximate dynamic programming solution of a single DG. © [2020] IEEE.

4.4 Stability Analysis

Stability analysis of the local optimal controller is done in this section. For notational brevity function dependency on state and time is suppressed unless otherwise stated for clarity. Define a closed ball $B_r \subset \mathbb{R}^{2(1+L)}$ with radius r centered at the origin and let $\chi \triangleq B_r \cap \mathbb{R}^2$.

Subtracting (4.13) from (4.19), BE (δ) and extrapolated BE (δ_i) can be expressed as,

$$\delta = -\phi^T \tilde{W}_c - \bar{u} \tanh(\hat{D}_a) G_\sigma^T \tilde{W}_a + R\bar{u}^2 \ln\left[\frac{1-\tanh^2(\hat{D}_a)}{1-\tanh^2(\hat{D}_a^*)}\right] - \nabla\epsilon f \tag{4.25}$$

$$\delta_i = -\phi_i^T \tilde{W}_c - \bar{u} \tanh(\hat{D}_{ai}) G_{\sigma i}^T \tilde{W}_a + R\bar{u}^2 \ln\left[\frac{1-\tanh^2(\hat{D}_{ai})}{1-\tanh^2(\hat{D}_{ai}^*)}\right] - \nabla\epsilon_i f_i \tag{4.26}$$

where, $\tilde{W}_c = W - \hat{W}_c$ and $\tilde{W}_a = W - \hat{W}_a$ are the critic and actor weight estimation errors, $\nabla\epsilon_i = \nabla\epsilon(x_i)$, $f_i = f(x_i)$, $g_i = g(x_i)$, $\nabla\sigma_i = \nabla\sigma(x_i)$, $\hat{D}_a^* = (W^T\nabla\sigma + \nabla\epsilon)g/2R\bar{u}$ and $\hat{D}_{ai}^* = (W^T\nabla\sigma_i + \nabla\epsilon_i)g_i/2R\bar{u}$.

Consider the continuously differentiable positive definite (PD) candidate Lyapunov function $V_L : \mathbb{R}^{2(1+L)} \times \mathbb{R}_{\geq 0} \to \mathbb{R}_{\geq 0}$,

$$V_L(Z,t) = V^*(x) + \frac{1}{2}\tilde{W}_c^T \Gamma^{-1} \tilde{W}_c + \frac{1}{2}\tilde{W}_a^T \tilde{W}_a \tag{4.27}$$

where, V^* is the optimal value function, $Z = \begin{bmatrix} x^T & \tilde{W}_c^T & \tilde{W}_a^T \end{bmatrix}^T \in \mathbb{R}^{2(1+L)}$. Since V^* is PD and LS gain matrix is bounded such that $\underline{\Gamma} I_L \leq \Gamma(t) \leq \bar{\Gamma} I_L$ [55, 162], V_L is bounded as [163],

$$\underline{v}_L(\|Z\|) \leq V_L(Z,t) \leq \bar{v}_L(\|Z\|) \tag{4.28}$$

where, $\underline{v}_L$ and $\bar{v}_L$ are class $\mathcal{K}$ functions. Using the BEs in (4.25) and (4.26), time derivative of (4.27) along the dynamics (4.5), (4.20), (4.21), (4.23) can be expressed as,

$$\begin{aligned}\dot{V}_L = -Q(x) - U(u^*) - \tilde{W}_c^T \left[k_{c1}\frac{\phi\phi^T}{\rho}\left(1 - \frac{1}{2\rho}\right) + \frac{k_{c2}}{M}\sum_{i=1}^{M}\frac{\phi_i\phi_i^T}{\rho_i} - k_{c2}\sum_{i=1}^{M}\frac{\phi_i\phi_i^T}{2M\rho_i^2} + \frac{\beta\Gamma^{-1}}{2}\right]\tilde{W}_c - \tilde{W}_a^T\dot{\hat{W}}_a \\ - \bar{u}\tilde{W}_c^T\left[k_{c1}\tanh(\hat{D}_a)\frac{\phi}{\rho}G_\sigma^T + \frac{k_{c2}}{M}\sum_{i=1}^{M}\tanh(\hat{D}_{ai})\frac{\phi_i}{\rho_i}G_{\sigma i}^T\right]\tilde{W}_a + \Xi\end{aligned} \tag{4.29}$$

where, $\Xi = \tilde{W}_c^T\left[k_{c1}\frac{\phi}{\rho}\left(R\bar{u}^2\ln\left[\frac{1-\tanh^2(\hat{D}_a)}{1-\tanh^2(\hat{D}_a^*)}\right] - \nabla\epsilon f\right) + \frac{k_{c2}}{M}\sum_{i=1}^{M}\frac{\phi_i}{\rho_i}\left(R\bar{u}^2\ln\left[\frac{1-\tanh^2(\hat{D}_{ai})}{1-\tanh^2(\hat{D}_{ai}^*)}\right] - \nabla\epsilon_i f_i\right)\right]$. Using the inequality $\frac{\phi\phi^T}{\rho^2} \leq \frac{\phi\phi^T}{\rho}$ [162], and substituting for $\dot{\hat{W}}_a$, the Lyapunov

derivative can be upper bounded as,

$$\dot{V}_L \leq -Q(x) - U(u^*) - k_{c2}\tilde{W}_c^T\left[\frac{\beta\Gamma^{-1}}{2k_{c2}} + \sum_{i=1}^{M}\frac{\phi_i\phi_i^T}{2M\rho_i}\right]\tilde{W}_c - k_{a1}\tilde{W}_a^T\tilde{W}_a + k_{a1}\tilde{W}_a^T\tilde{W}_c$$
$$- \bar{u}\tilde{W}_a^T\left[k_{c1}\tanh(\hat{D}_a)\frac{\phi}{\rho}G_\sigma^T + \frac{k_{c2}}{M}\sum_{i=1}^{M}\tanh(\hat{D}_{ai})\frac{\phi_i}{\rho_i}G_{\sigma i}^T\right]W + \Xi \quad (4.30)$$

The approximation $\ln\left[1-\tanh^2(D)\right] = \ln(4) - 2Dsgn(D) + \epsilon_D$ [158] is employed in the subsequent stability analysis for the bounded approximation error $\epsilon_D \leq \bar{\epsilon}_D$ for $D = \{\hat{D}_a, D_a^*\}$. Define the notation $\overline{|\omega|} \triangleq \sup_{x\in\chi}\|\omega\|$ and positive constants $\{\lambda_j | j = 1,\ldots,6\}$ such that $\lambda_1+\lambda_2+\lambda_3 = 1$ and $\lambda_4+\lambda_5+\lambda_6 = 1$. Further, let $\underline{C}$ and ϑ are two positive constants defined as,

$$\underline{C} = \frac{\beta}{2\bar{\Gamma}k_{c2}} + \frac{\underline{c}}{2} \quad (4.31)$$

$$\vartheta = \frac{\gamma^2(k_{c1}+k_{c2})^2}{4}\Big(\frac{\bar{u}\bar{W}^2\overline{|G_\sigma|}}{k_{a1}\lambda_5} + \frac{\Delta^2}{k_{c2}\underline{C}\lambda_3}\Big) + \Delta_{u^*} \quad (4.32)$$

where, $\Delta = \bar{u}(2\bar{W}\overline{|G_\sigma|}+\overline{|\nabla\epsilon g|})+R\bar{u}^2\bar{\epsilon}_D+\overline{|\nabla\epsilon f|}$, $\Delta_{u^*} = 2\bar{u}(\bar{W}\overline{|G_\sigma|}+\overline{|\nabla\epsilon g|})+R\bar{u}^2(ln(4)+\bar{\epsilon}_{D_a^*})$, and $\bar{\epsilon}_D = \bar{\epsilon}_{\hat{D}_a} + \bar{\epsilon}_{D_a^*}$. Moreover, define any class $\mathcal{K}$ PD function $v_L(\|Z\|)$, and sufficient conditions for ultimate boundedness as,

$$v_L(\|Z\|) \leq \frac{1}{2}\Big(Q(x) + k_{c2}\underline{C}\lambda_1\|\tilde{W}_c\|^2 + k_{a1}\lambda_4\|\tilde{W}_a\|^2\Big) \quad (4.33)$$

$$2\sqrt{k_{a1}k_{c2}\underline{C}\lambda_2\lambda_6} \geq k_{a1} + \bar{u}\gamma(k_{c1}+k_{c2})\overline{|G_\sigma|} \quad (4.34)$$

$$v_L^{-1}(\vartheta) < \bar{v}_L^{-1}(\underline{v}_L(r)) \quad (4.35)$$

Using the boundedness of the normalized regressor such that $\|\frac{\phi}{\rho}\| \leq \gamma$ [55], and under the sufficient conditions (4.34) and (4.35), $\dot{V}_L$ can be further upper bounded as,

$$\dot{V}_L \leq -v_L(\|Z\|), \quad \forall\|Z\| > v_L^{-1}(\vartheta) \quad (4.36)$$

for all $Z \in B_r$ and $t \geq 0$. Hence, according to [163] the concatenated state and weight estimation error system Z is uniformly ultimately bounded (UUB) in the sense $\lim_{t\to\infty}\sup\|Z\| \leq$

$\underline{v}_L^{-1}(\bar{v}_L(v_L^{-1}(\vartheta)))$. Taking the overall Lyapunov function as $\sum_{k\in\mathcal{G}} V_{L,k}(Z_k,t)$, and following the similar procedure, UUB result for the entire MG can be established. Based on the analysis given in this section, it can be inferred that, under the sufficient conditions and assumptions, the proposed concept stabilizes each DG and eventually the entire DCMG.

4.5 Simulation Test Cases and Results

Simulations were carried out considering the 7 bus test system shown in Figure 4.3 with transmission line resistance 0.2 Ω and nominal voltage 30 V. Typically, the number of DGs are limited in islanded DCMGs and hence a small test system has been used to validate the proposed concept. Plant and controller parameters are given in Table 4.1 for $k = 1, 2, 3$. Value function of each DG is approximated by a quadratic power series of error system states by considering the activation function $\sigma(x_k) = \begin{bmatrix} x_{1k}^2 & x_{2k}^2 & x_{1k}x_{2k} \end{bmatrix}^T$. This activation function makes the LIP NN which contains 3 neurons and a single layer. Initial conditions for the actor and critic weights were considered as 0.2 and the least square gain matrix was initialized with $100I_{3\times3}$.

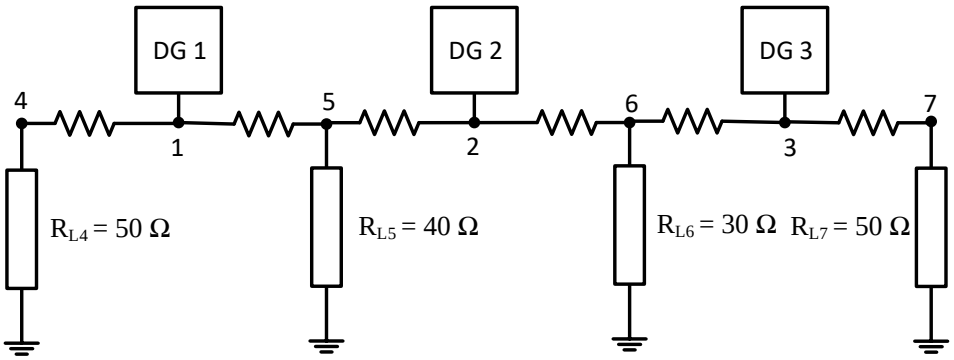

Figure 4.3: Bus system used for simulations. © [2020] IEEE.

Four main simulation test cases are presented. The first test case simulates the startup phase of the DCMG with zero initial conditions which demonstrates the performance of the proposed approach during the startup transient stage. Second and third test cases are presented to show the adaptability, load sharing, and stability of the proposed droop free concept against load and DG input voltage disturbances. Each test case was compared with the traditional droop controllers with PI control as the fourth simulation test case.

Table 4.1: Plant and Controller Parameters. © [2020] IEEE.

Parameter	Value	Parameter	Value
L_k	500 μH	k_{c1}	10
r_{Lk}	0.5 Ω	k_{c2}	20
C_k	120 μF	k_{a1}	20
E_k	15 V	β	0.3
$\bar{\Gamma}$	200	ν	0.05
P_k	$I_{2\times 2}$	R_k	$1/(L_k C_k)$

4.5.1 Startup Transient Optimization

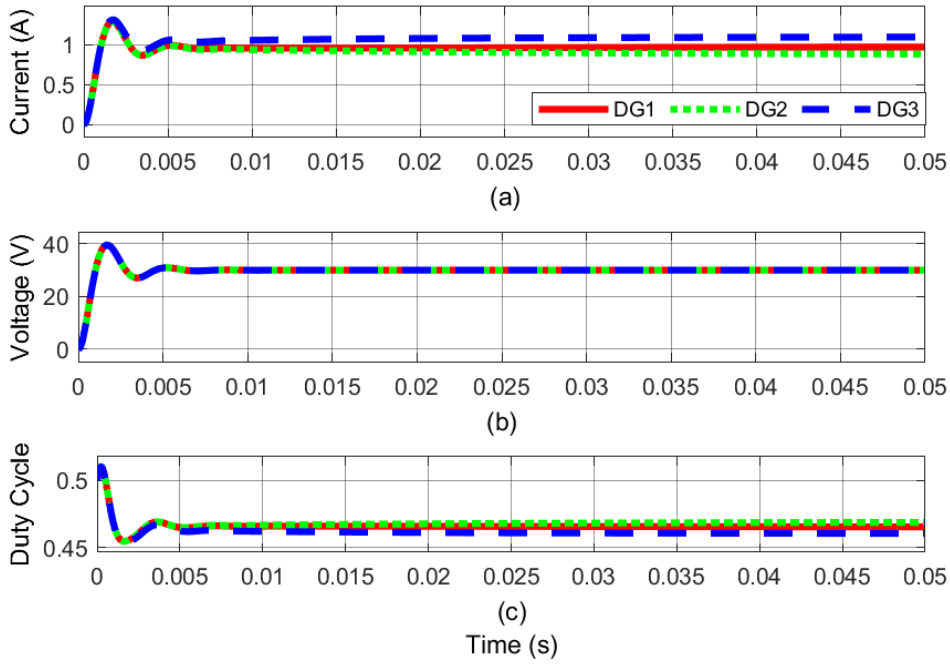

Figure 4.4: Variations during the startup (a) Output current, (b) Output voltage and (c) Duty cycle. © [2020] IEEE.

The DCMG was initialized with zero initial conditions and the results are shown in Figure 4.4. The main objective of this test case to demonstrates the performance of the proposed approach during the startup transient stage. According to the results, output voltages reach the desired 30 V within 10 ms. The duty cycle variation is very small and it is

bounded between 0.453 and 0.511 which validates the claim of constrained input. During the learning transient, the maximum output current is observed as 1.3 A, while the maximum output voltage is 39.5 V. Steady-state (s.s) output currents of DG1, DG2 and DG3 are 0.97 A, 0.87 A and 1.1 A respectively. According to the results, it can be identified that the proposed controller perfectly share the load and regulate the voltage to the desired value while protecting the overall system stability.

The convergence of the actor and critic weights and satisfaction of the rank condition are shown in Figure 4.5 and Figure 4.6 respectively. Both actor and critic weights converge to 0.0011, 0.0026, 0.0008 and the rank condition satisfies the assumption in (4.22). This result demonstrates the convergence performance of the proposed learning algorithm given by (4.20), (4.21) and (4.23).

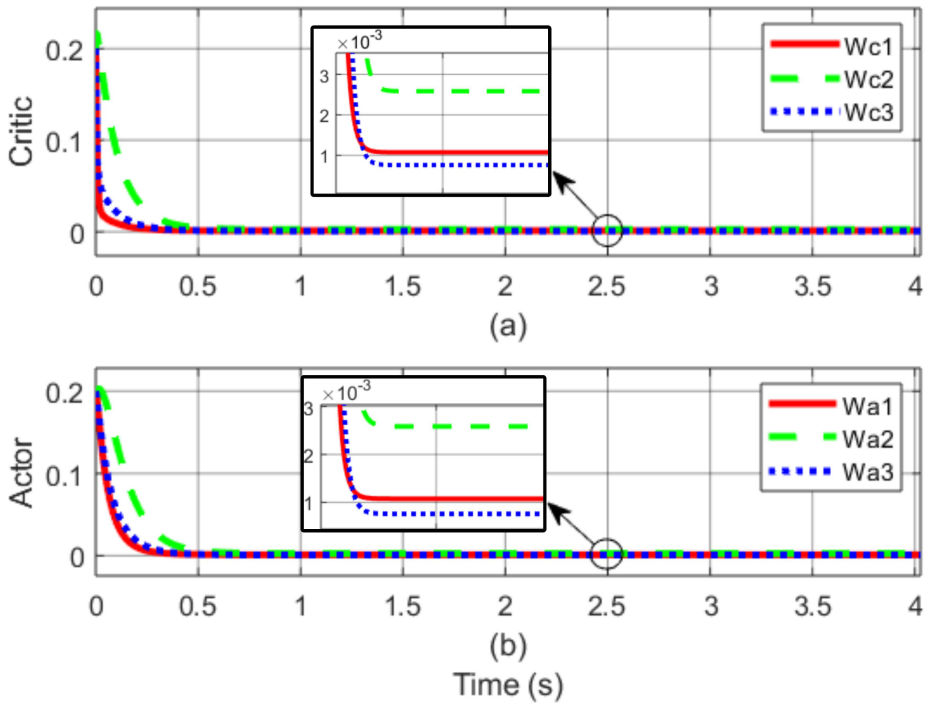

Figure 4.5: Variation of the DG1 NN weights (a) Critic weights, (b) Actor weights. © [2020] IEEE.

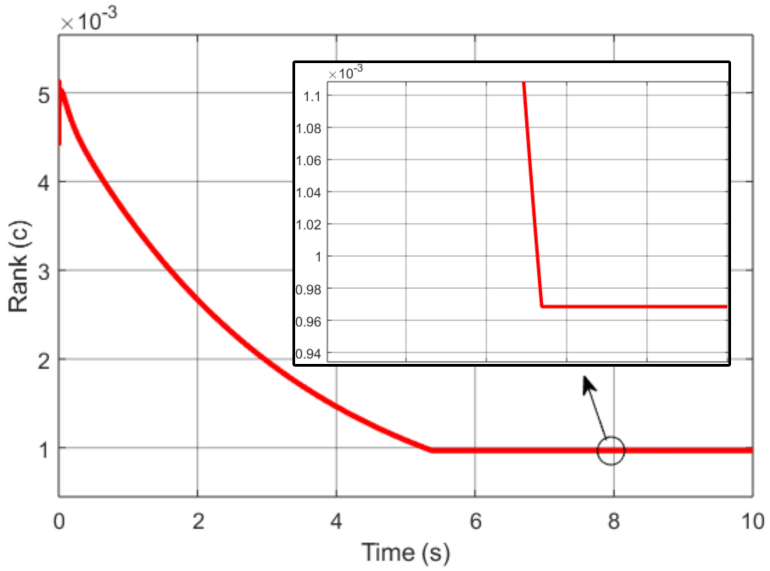

Figure 4.6: Variation of the rank condition given in assumption 2. © [2020] IEEE.

4.5.2 Adaptability Against Load Disturbances

The main objective of this test case is to demonstrate the adaptive control ability of the proposed approximate optimal control law under load influences. In order to explore the adaptability of the proposed concept against load disturbances, a step load change from 40 Ω to 20 Ω was given to load at bus five at $t = 1s$. According to the results shown in Figure 4.7, the peak to peak (p.p) maximum output voltage fluctuation around the nominal voltage is 1.06 V and all the DGs regain the desired voltage within 10 ms. Duty cycles of all the DGs remain within the acceptable range. DG1 and DG2 output currents rise to 1.34 A and 1.25 A since they are close to the load bus 5 while DG3 output current remains at 1.1 A. According to the simulation results, it can be inferred that the proposed control algorithm is capable of regulating the DG output voltage and protecting the system stability under load disturbances.

4.5.3 Adaptability Against Input Voltage Disturbance

Analysis of the adaptability of the proposed approximate optimal control law against the input voltage disturbance is the main objective of this simulation test case. In order to see the performance, a step input voltage change was given to DG1 from 15 V to 20 V at

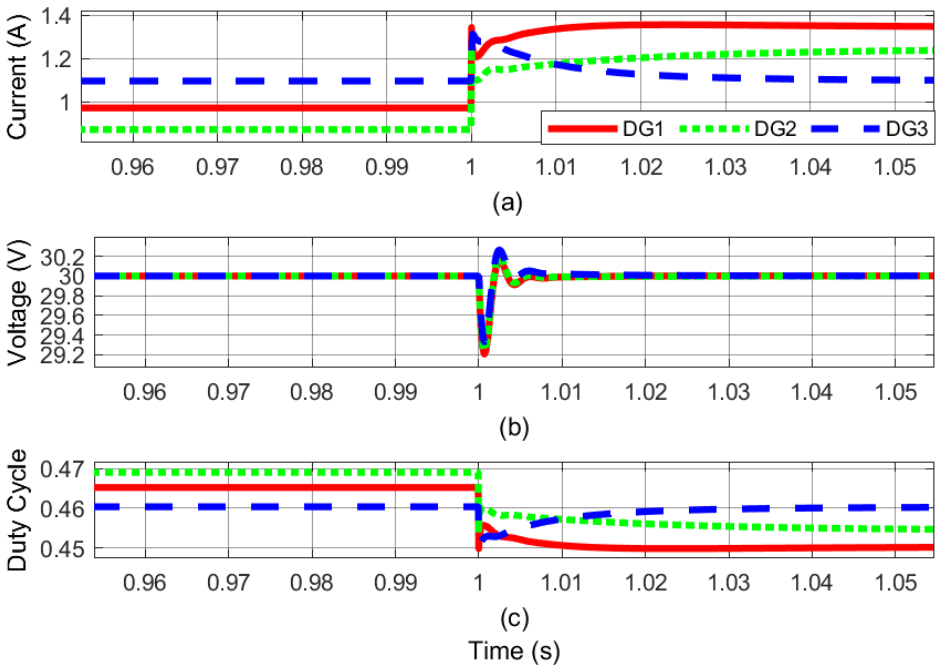

Figure 4.7: Variations subjected to a load disturbance (a) Output current, (b) Output voltage and (c) Duty cycle. © [2020] IEEE.

$t = 1s$. According to the results shown in Figure 4.8, output voltages and currents reach their original s.s values within 20 ms. The p.p maximum output voltage fluctuation around the nominal voltage is 0.5 V. DG1 duty cycle converges to a new value due to the input voltage change while other duty cycles remain in the same values as before. Based on the simulation test results, it can be seen that the proposed control algorithm perfectly regulates the DG output voltage and protects the system stability under input voltage disturbances.

4.6 Comparison with Traditional Controller

The main objective of this test case is to compare the performance of the proposed concept against the existing droop based controls. The proposed controller was compared with the traditional PI-based droop controller. In PI-based droop control, two cascade PI controllers were employed in the traditional method which comprises of slow outer voltage loop and a fast inner current loop. Proportional and integral gains of the outer voltage loop were set to 0.001 and 5 where the corresponding current loop gains were considered as 1 and 50 respectively. The PI gains were tuned to have the best transient and s.s responses. The

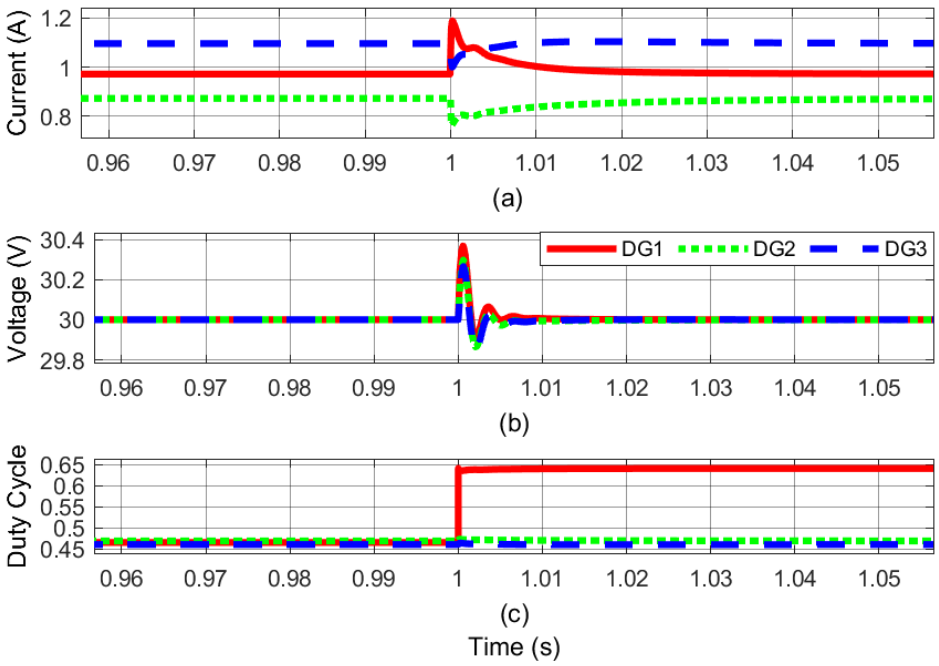

Figure 4.8: Variations subjected to an input voltage disturbance (a) Output current, (b) Output voltage and (c) Duty cycle. © [2020] IEEE.

droop relationship gives a reference voltage set point for the voltage loop. Droop coefficients were selected as 0.5 Ω for virtual impedance and 30 V for the no-load reference voltage. In order to keep the duty cycle within the allowable bound, the output of the current control loop was passed through a hard limiter before feeding into the converter. Upper and lower bounds of the hard limiter were selected as 1 and 0 respectively. Performances of the controllers were compared in two situations. Case 1 represents the startup phase of the DCMG and case 2 represents a load change scenario at bus five from 40 Ω to 20 Ω after 10s of normal operation. The results are summarized in Table 4.2 and Figure 4.9 to Figure 4.11.

The variations of integral transient state costs given by (4.7) are shown in Figure 4.9. The cost can be used as a measure of the transient performance of the controller. In the startup phase as well as after the load change, the proposed controller shows a small integral cost compared to the traditional PI controller. The main observations of the startup cost comparison can be summarized as; with the proposed controller, the maximum cost can be observed in DG1 which is 0.5557 and with the PI controller, the maximum transient cost of 2.929 can be observed in DG3. After the load change, all DG integral costs increase and the

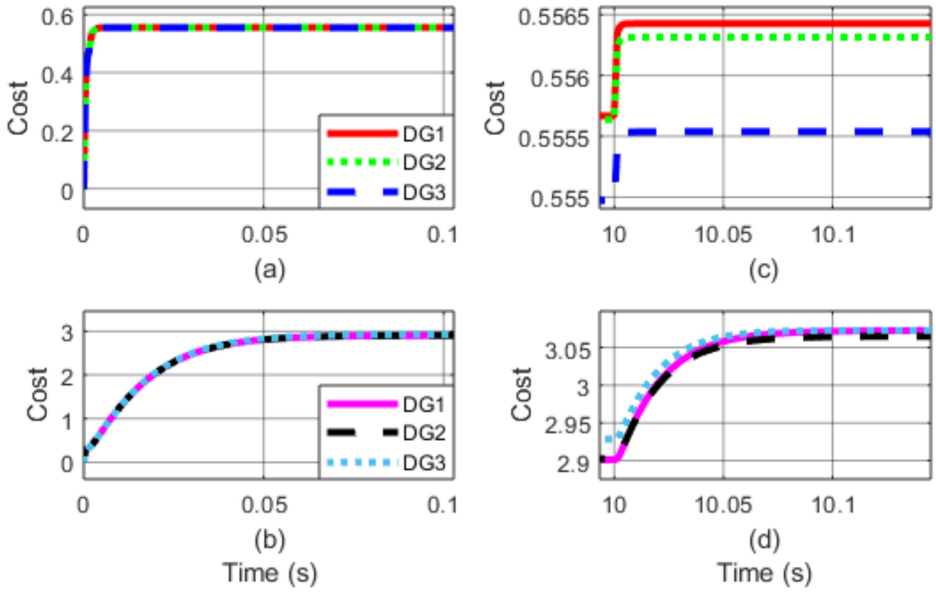

Figure 4.9: Comparison of integral state costs (a) Proposed controller in startup, (b) Traditional controller in startup, (c) Proposed controller in load change, (d) Traditional controller in load change. © [2020] IEEE.

main observation can be summarized as; with the proposed controller, DG1 transient cost shows the highest value of 0.5564 and with the PI controller, DG3 transient cost increases to 3.074. Integral costs of the remaining DGs and percentage improvements (% Imp.) over the PI droop method are given in Table 4.2. According to the results, improved transient performance can be achieved by the proposed concept.

Further, the convergence is much faster in the proposed controller compared to the conventional method. In the startup, the maximum settling times were observed in DG3 which are; 2.114 ms under the proposed controller and 38.812 ms with the PI droop controller. After the load change, the maximum settling times were observed as; 2.422 ms in DG3 with the proposed controller and 61.022 ms in DG 1 under the PI droop controller. All the other settling times with PI droop controller and percentage improvements are given in Table 4.2. Clearly, the PI droop controller shows a sluggish response in the startup and under a load disturbance compared to the proposed controller.

Duty cycle variations in startup and load change transients are shown in Figure 4.10. In both cases, the droop controller shows higher variation and it grasps both allowable upper or lower bounds. In the startup, the maximum p.p duty cycle variations are observed as;

0.0569 with the proposed controller, and 1 with the PI controller. The percentage p.p duty cycle reduction in DG3 over the PI droop controller was computed as 94.31 %. After the load change, both controllers show small duty cycle variations and the maximum p.p variations are; 0.0154 with the proposed controller and 0.0552 with the PI controller. The proposed controller achieves a significantly low duty cycle variation over the PI droop controller due to the minimization of the control effort given in (4.10).

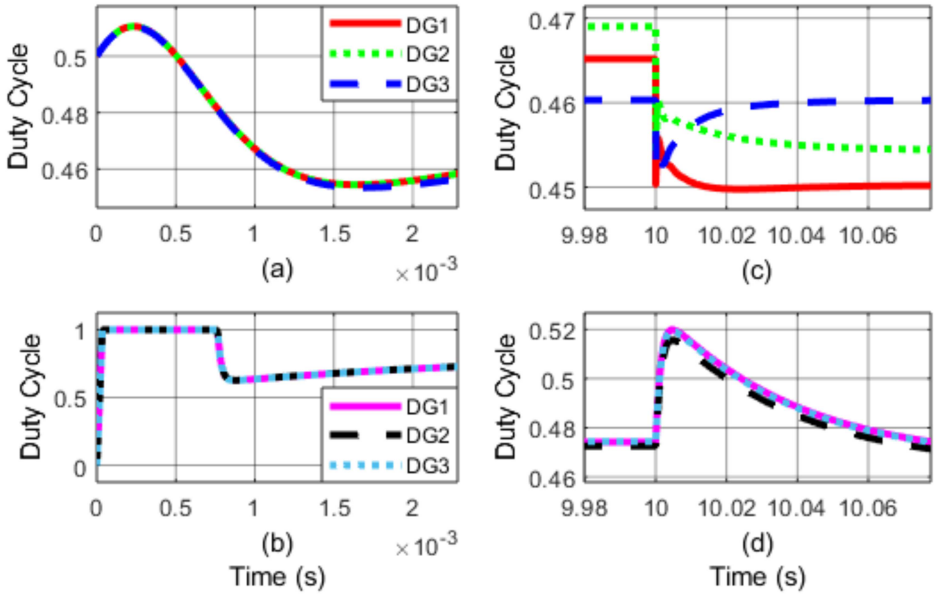

Figure 4.10: Comparison of duty cycles (a) Proposed controller in startup, (b) Traditional controller in startup, (c) Proposed controller in load change, (d) Traditional controller in load change. © [2020] IEEE.

DG output voltage deviations from the nominal voltage are shown in Figure 4.11. Main observations drawn from this analysis are;

1. In regular operation and after a load change, zero DG output voltage errors are observed under the proposed controller.

2. In the regular operation, the maximum voltage error of 0.5 V can be observed in DG3 with PI droop controller.

3. The minimum voltage error can be observed in DG2 which is 0.47 V under the PI droop controller.

After the load change, all the DG voltage errors increased and comparative results are depicted in Table 4.2 for the PI droop controller. Even though the load change greatly affected the DG voltage error in the PI droop controller, no change can be seen with the proposed controller. The average DCMG voltage error before the load change was computed as; 0.059 V with the proposed controller, and 0.54 V with the PI controller. After the load change, average DCMG voltage errors increase to; 0.07 V with the proposed controller and 0.67 V with the PI controller. The percentage improvements in the average voltage gained by the proposed controller over the droop methods are; 89.1% before the load change and 89.55% after the load change. Percentage increment in the average MG voltage error before and after the load change is; 18.64% in the proposed controller and 24.07% in the droop controllers. Further, by employing the proposed concept 80.92% overall DCMG integral state cost in startup and 81.9% overall DCMG integral state cost in load change are reduced over the traditional PI droop controller.

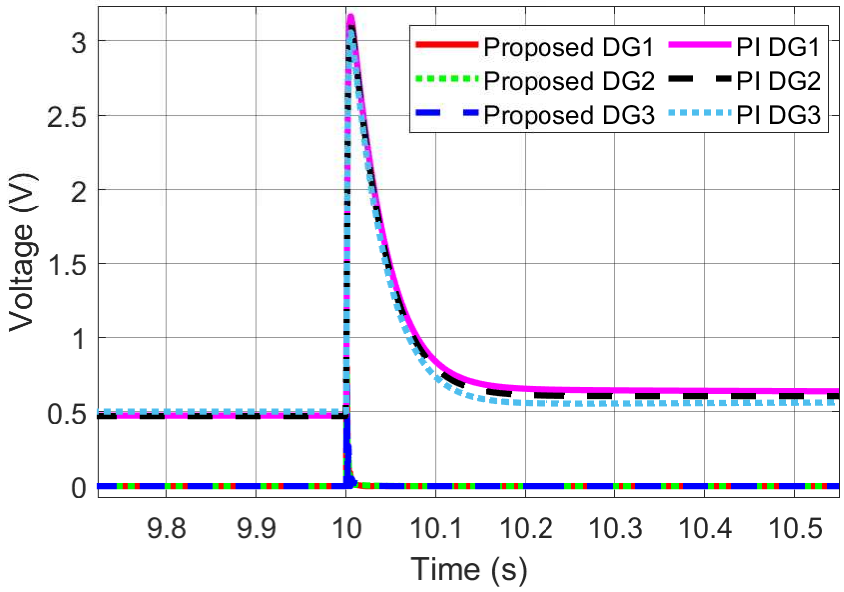

Figure 4.11: Comparison of voltage errors before and after the load change. © [2020] IEEE.

Table 4.2: Comparative Analysis with Traditional PI Based Droop Controller. © [2020] IEEE.

		DG1			DG2			DG3		
		Proposed	Traditional	% Imp.	Proposed	Traditional	% Imp.	Proposed	Traditional	% Imp.
Integral state cost	case 1	0.5557	2.901	80.84	0.5556	2.903	80.86	0.5550	2.929	81.05
	case 2	0.5564	3.073	81.89	0.5563	3.065	81.85	0.5555	3.074	81.93
Settling time (ms)	case 1	2.108	37.973	94.45	2.107	38.003	94.46	2.114	38.812	94.55
	case 2	2.101	61.002	96.56	2.098	54.483	96.15	2.422	51.062	95.26
S.S voltage deviation (V)	case 1	0.00	0.47	100	0.00	0.47	100	0.00	0.50	100
	case 2	0.00	0.63	100	0.00	0.60	100	0.00	0.57	100

4.7 Experimental Validation

The controllers and the DG system were implemented based on MATLAB/Simulink and dSPACE control systems for experimental validation. Figure 4.12 shows the experimental test bench that contains the DS1104 controller card, CP1104 I/O board, MOSFET converter system and the bus system without DG3 and load bus seven adopted from Figure 4.3. Parameters of the experimental setup are given in Table 4.3 with f_s is the switching frequency and r_l is the distribution line resistance. All the other parameters were the same as in the simulations. Multiple test case results are shown in Figure 4.13 to Figure 4.17.

Table 4.3: Parameters of the Experimental Setup. © [2020] IEEE.

Parameter	Value	Parameter	Value
L_k	10 mH	E_k	15 V
r_{Lk}	0.8 Ω	f_s	30 kHz
C_k	500 μF	r_l	1 Ω

For the practical implementation, the proposed approach requires feedbacks from two current sensors and two voltage sensors. Two current feedbacks are the inductor and the output currents while the two voltage feedbacks are the input and output voltages. These instantaneous data are fed into the controller which is programmed to reflect the process given in Figure 4.2. The controller takes the current and voltage information from the sensors to run the update laws (4.20), (4.21) and (4.23) to generates the duty cycle according to

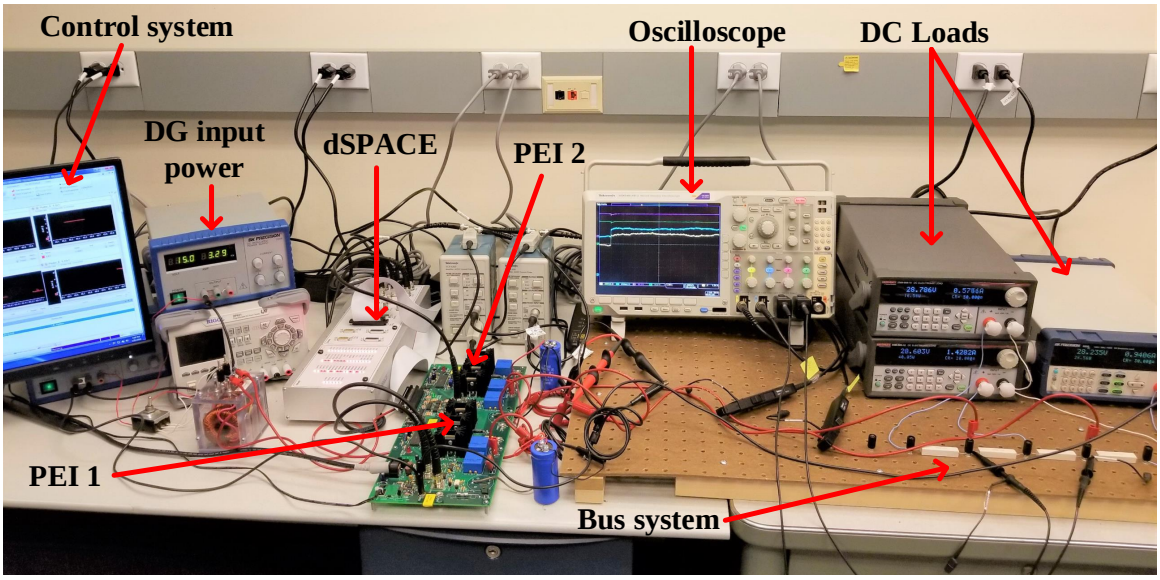

Figure 4.12: Experimental test bench. © [2020] IEEE.

(4.24). Then the duty cycle is fed into the PWM generator which outputs the corresponding switching signals to the converters. In addition to the measured signals, the controller requires the values of inductance, inductive resistance, and capacitance of the converter.

In the presented experimental test setup, the update laws were programmed in the MATLAB/Simulink environment. The feedback signals from the current and voltage sensors were taken into the computer through the dSPACE DS1104 controller card and CP1104 I/O board. Some of the voltage and current information were measured directly from the inbuilt test points in the *Vishay* power electronic drive board. To get the other voltage feedbacks, Tektronix P5200A differential probes were used. Further, Tektronix TCP A300 current amplifiers combined with TCP305A current probes have been used to get the output current information of each DG. Generated duty cycles were passed through the PWM generator and the corresponding PWM switching signals were fed into the MOSFET converters through the slave I/O PWM DBUS connector in the dSPACE CP1104 I/O board.

4.7.1 Startup Transient Optimization

Experimental variations of the DG output currents and voltages during the startup phase of the DCMG are shown in Figure 4.13. According to the results, it can be seen that both DGs regulate the output voltage close to the desired 30 V. However, due to the

unmodeled dynamics in the experimental system, slight deviations can be observed in the output voltages. Further, the s.s currents of DG1 and DG 2 are 0.95 A and 1.26 A respectively. The PWM control signal outputs from the slave I/O PWM DBUS connector in the dSPACE is shown in Figure 4.14. The s.s duty cycles of DG1 and DG 2 were observed as 0.45 and 0.43 respectively.

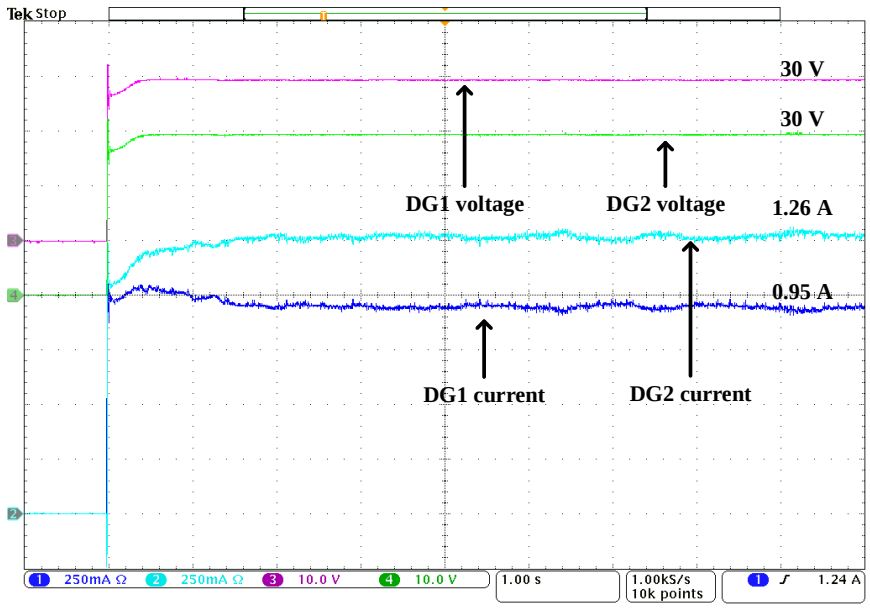

Figure 4.13: Experimental variations during the startup. © [2020] IEEE.

4.7.2 Adaptability Against Load Changes

Experimental variations of the DG output currents and voltages subjected to a load change at bus five from 40 Ω to 20 Ω are shown in Figure 4.15. As shown in the results, the output voltage of both DGs regains the desired voltage within a short time. Even though a small voltage dip is observed at the point of load change, the difference in s.s values before and after the load change is the same. There are no overshoots observed in the output currents and the s.s values are measured as 1.33 A and 1.5 A in DG1 and DG2 after the load change.

4.7.3 Adaptability Against Input Voltage Disturbance

Experimental variations of the DG output currents and voltages subjected to an input voltage disturbance in DG1 are shown in Figure 4.16. Slight overshoots are observed in

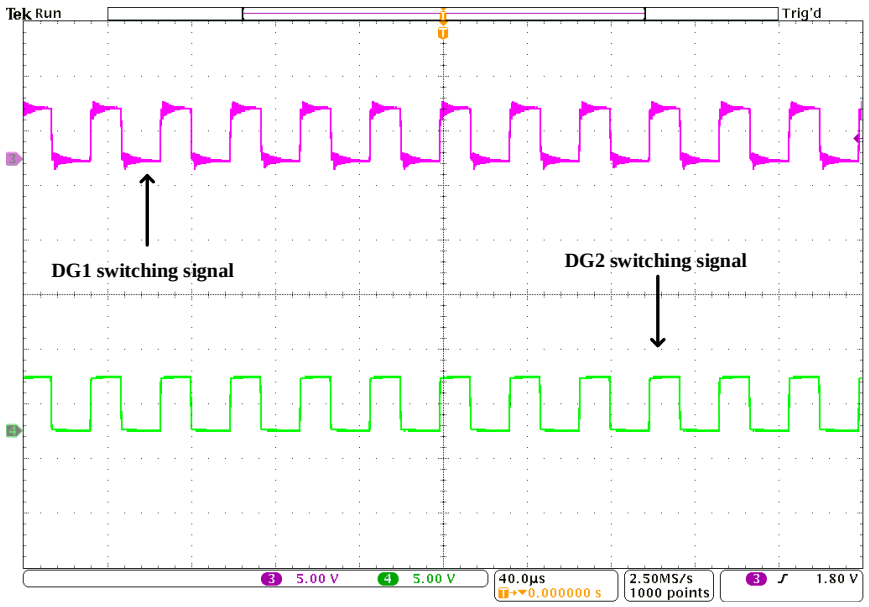

Figure 4.14: Experimental PWM switching waveforms. © [2020] IEEE.

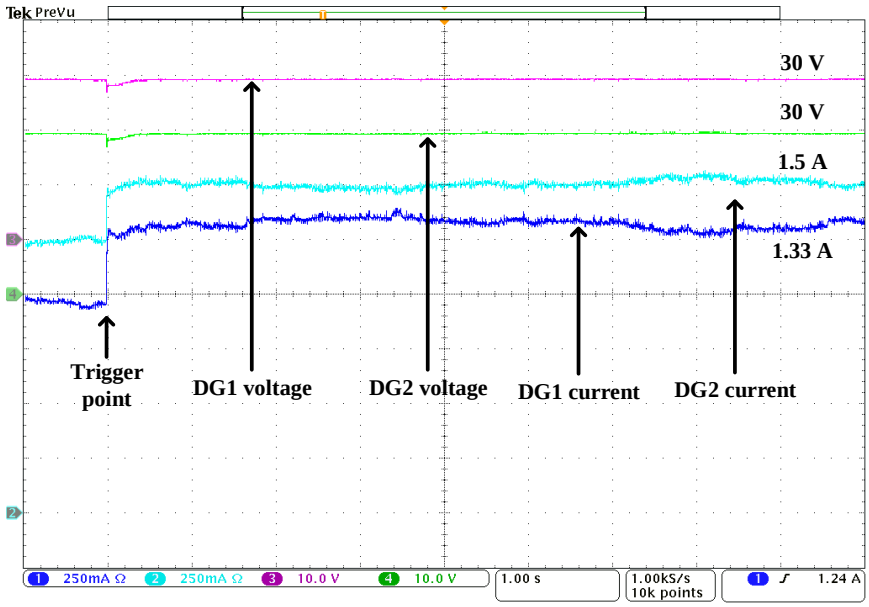

Figure 4.15: Experimental variations subjected to a load change. © [2020] IEEE.

both the DG output voltages for a short time and then they converge to the desired s.s values. An overshoot is observed in DG1 output current and on the contrary, an undershoot can be seen in DG2 output current. The reason for these large variations is the unmodeled dynamics in the switching action which used to trigger the input voltage change. Despite the

effect of unmodeled dynamics, both DG output currents and voltages regain their respective equilibrium after a short period of time.

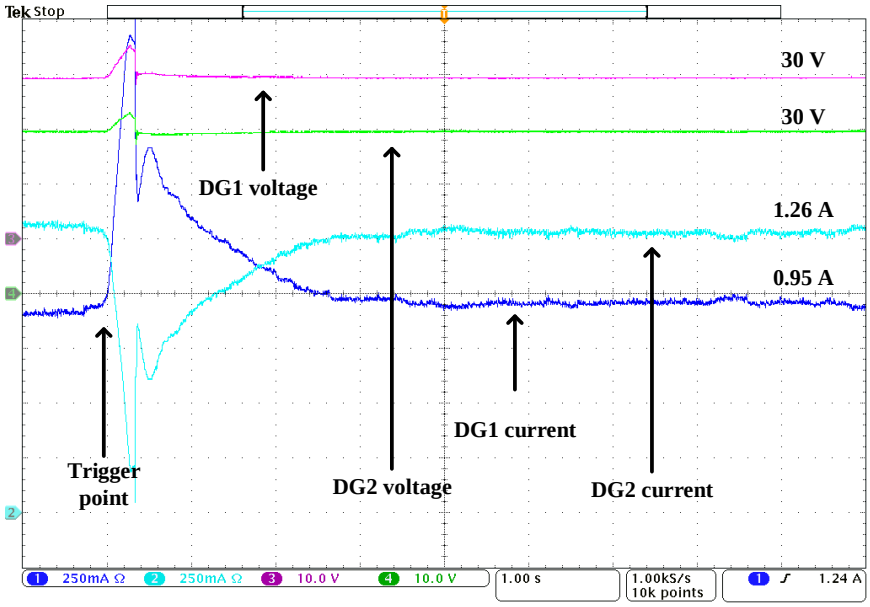

Figure 4.16: Experimental variations subjected to an input voltage change. © [2020] IEEE.

4.8 Conclusion

In this chapter, a droop free, online approximate optimal feedback control methodology was proposed to control DGs in islanded DCMGs. Each DG was modeled as a control affine dynamical system with constrained input. An optimal control problem was formulated to minimize the infinite horizon quadratic state cost with a non-quadratic control input penalty function. An approximate solution to the optimal control problem was obtained by an ADP method based on a RL algorithm. In the proposed approach, the optimal value function and the optimal control law of each DG were approximated by two separate LIP NNs. A LS based update law was implemented to update the unknown weights in the critic NN while the second update law given by the stability analysis was used to update the actor NN weights. The employed update laws are inspired by the concurrent RL which uses the simulation of experience through the BE extrapolation to guarantee the parameter convergence to a neighborhood of the actual weights without PE. Lyapunov stability analysis was presented

to show the UUB stability of the system states and the parameter estimates. Simulation and experimental results were given to demonstrate the effectiveness and applicability of the proposed concept. Both results show excellent output voltage regulation and adaptable nature in the startup, under load and input voltage changes.

The proposed feedback optimal control approach with concurrent RL requires the exact model knowledge of the DG. This includes the input voltage to the PEI, inductive, resistive and capacitive parameters of PEI .etc. To overcome this limitation, the existing algorithm can be reformulated as an advanced adaptive learning algorithm that does not require any internal parameters or exact model of the system. The adaptive algorithms can be realized by NN approximation of the dynamics combining the system identification functionalities associated with NNs and would be an interesting future direction of this work.

CHAPTER V

DECENTRALIZED OPTIMAL STABILIZATION OF ACTIVE LOADS IN ISLANDED DC MICROGRIDS

5.1 Major Objectives

The power buffer is an effective method of mitigating instabilities caused by nonlinear load profiles, which has been introduced in [66] and discussed in [3, 51, 67–69]. In these approaches, the power electronic interface (PEI) followed by the constant power load (CPL) is modeled as a variable impedance load seen by the distribution network which is referred to as an active load. Then its effective input impedance is maneuvered to stabilize the MG subjected to any transients such as startup or abrupt load changes. The power buffer contains large storage capacity and it is used to buffer, store and shape the input energy profile to the load rather than voltage regulation. Motivated by the lack of decentralized feedback optimal stabilization control approaches to optimally control active loads such as power buffers, this chapter introduces a novel control algorithm inspired by the adaptive/approximate dynamic programming (ADP). Most of the existing power buffer control methods, are either open-loop controllers or require communication among the active loads. Oppose to the existing open-loop and distributed controllers with communication, the proposed stabilization algorithm in this chapter possesses a decentralized, online feedback optimal stabilization ability of active loads operate in islanded DCMGs. The proposed methodology uses locally available measurements and no communication is required. The major challenge in ADP based optimal feedback controls is the requirement of the persistence of excitation (PE) condition to guarantee the

parameter convergence. Typically, the PE condition is achieved by adding a probing noise to the control input. Due to the lack of knowledge on sufficient noise power and the required number of distinct frequencies to satisfy the PE, the inclusion of random noise could cause serious issues. The proposed method in this chapter uses a concurrent reinforcement learning (RL) method to eliminate those issues. It does not require PE condition and hence no requirement of additive noise to the control input. The ADP based feedback optimal control solution utilizes value function approximation via neural networks (NNs). A model-based concurrent RL approach is employed to successively approximate unknown NN weights in the value function without the PE. Moreover, the decentralized stabilizing controller discussed in this chapter is an online, nonlinear feedback controller, which does not require any offline training. Therefore, the main objective of this chapter is to develop a communication free, decentralized, online feedback optimal controller to stabilizes active loads in DCMG without PE condition.

5.2 Active Loads in Islanded Microgrids

5.2.1 Active Load as a Member in the MG

Power system loads are typically modeled as constant impedance, power or current [164]. In the MG domain, end loads (ELs) are connected to the network through a PEI [4, 67]. Any PEI based load with local energy storage in a MG domain can be represented as Figure 5.1 and can be treated as an active load. The EL can be individual or a composite load of constant impedance, constant current or CPL. In DCMGs, the PEI can be any DC-DC converter topology which acts as the intermediate device between the MG and the EL. In this work, boost topology is used as the PEI as shown in Figure 5.1. The input characteristics of the PEI can be controlled to reflect the EL properties. Further, it behaves as a voltage and admittance translator between the MG and the EL [4].

Consider the average mode boost DC-DC converter shown in Figure 5.1 with the input voltage, input current, output voltage and control duty cycle are given by E_i, i_i, v_o, D_i respectively. At any given time, the variable input admittance of the PEI seen by the MG is,

$$y_i = \frac{i_i}{E_i} \tag{5.1}$$

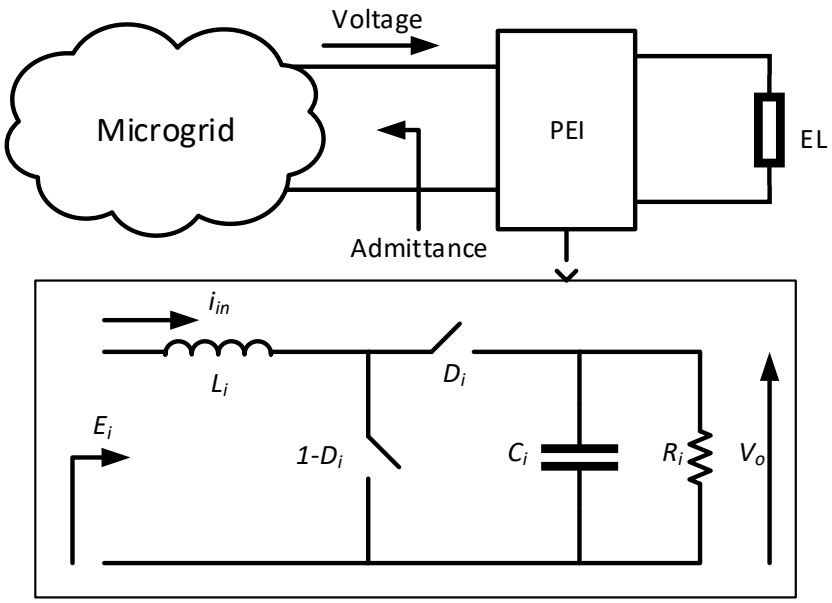

Figure 5.1: PEI as an interface between the MG and the EL with boost topology.

Considering a lossless PEI, the input-output power balance for a CPL with demand P_i yields,

$$E_i^2 y_i = P_i \tag{5.2}$$

Using the input-output voltage relationship of the boost converter ($E_i = D_i \bar{v}_i$), where $\bar{v}_i$ is the demanded voltage of the CPL, the input admittance of the PEI can be expressed as,

$$y_i = \frac{P_i}{(D_i \bar{v}_i)^2} = \frac{y_o}{D_i^2} \tag{5.3}$$

where, $y_o = \frac{P_i}{\bar{v}_i^2}$ is the effective output admittance. According to (5.3), each active load can be modeled as a variable admittance. It allows the active load to act as a member of the MG as a single quantity. Therefore, active loads can be included as elements in the power system admittance matrix. Consider a bus set M with m number of source buses and an active load set $\mathcal{L} \subset M$ with n load buses. Each active load is modeled as a variable shunt admittance (y_i) and included in the bus admittance matrix. Bus nodal relationship of the MG can be represented in matrix form as,

$$I = YE \tag{5.4}$$

where, $I \in \mathbb{R}^{(m+n)}$ and $E \in \mathbb{R}^{(m+n)}$ are the bus injected current vector and bus bar voltage vector. The symmetric bus admittance matrix is given by $Y \in \mathbb{R}^{(m+n)\times(m+n)}$. Since loads are modeled as variable admittances and included in the admittance matrix, bus nodal relationship given in (5.4) can be partitioned as,

$$\begin{bmatrix} I_s \\ \underline{0} \end{bmatrix} = \begin{bmatrix} Y_1 & Y_2 \\ Y_3 & Y_4 \end{bmatrix} \begin{bmatrix} E_s \\ E_b \end{bmatrix} \tag{5.5}$$

where, $I_s \in \mathbb{R}^m$ is the source current injections, $E_s \in \mathbb{R}^m$ is the source bus voltages, $E_b \in \mathbb{R}^n$ is the load bus voltages and $\underline{0} \in \mathbb{R}^n$ is the zero vector. Partitioned admittance matrix consists of four sub-matrices $Y_1 \in \mathbb{R}^{m\times m}$, $Y_2 \in \mathbb{R}^{m\times n}$, $Y_3 \in \mathbb{R}^{n\times m}$, $Y_4 \in \mathbb{R}^{n\times n}$. Active loads are embedded in diagonal terms of Y_4 as admittances. Load bus voltages of the MG can be obtained by,

$$E_b = Y_4^{-1}\Big(\underline{0} - Y_3 E_s\Big) \tag{5.6}$$

Once each active load is modeled as a variable shunt admittance (y_i) and included in the bus admittance matrix, it can be identified that the active load bus input voltages are a function of transmission line parameters, all the active load input admittances, and source voltages [3]. Hence, all the active loads are coupled and control decision of each active load affects the others.

5.2.2 Dynamic Modeling of Active Loads

The energy and admittance domain dynamic model of the i^{th} active load with negligible inductor energy storage can be given as [3, 67],

$$\dot{w}_i = E_i^2 y_i - P_i \tag{5.7}$$

$$\dot{y}_i = u_i \tag{5.8}$$

where, w_i is the energy stored in the capacitor, E_i is the locally available bus voltage, P_i is the power demand of the CPL and u_i is the control input. For the boost topology, the

corresponding duty cycle can be computed from the control input u_i as [73],

$$D_i = E_i\Big(1 - L_i u_i\Big)\sqrt{\frac{C_i}{2w_i}} \tag{5.9}$$

where, L_i and C_i are the inductance and capacitance of the PEI. From (5.7) the desired input admittance of the i^{th} player can be calculated instantaneously as,

$$\bar{y}_i = P_i/E_i^2, \quad \forall E_i \geq \Delta > 0 \tag{5.10}$$

where, Δ is the minimum input voltage required for uninterruptible power supply before the shutdown of the active load during a fault. When the input voltage is less than Δ or zero in a case of a complete blackout, the desired input admittance is set to a large value to keep the system stable until the stored energy in the capacitor reaches a minimum. The time duration between the beginning of the fault and the time when the system goes unstable is refereed to as the critical clearing time in this chapter. If the fault is not cleared before the critical clearing time, then the load needs to be shut down. In normal situations, the desired input admittance (5.10) ensures the demanded power to the CPL at all the time. The desired energy state is given as a function of the desired voltage of the CPL ($\bar{v}_i$) as,

$$\bar{w}_i = \frac{1}{2}C_i\bar{v}_i^2 \tag{5.11}$$

Two new states $x_{i,1} = w_i - \bar{w}_i$, $x_{i,2} = y_i - \bar{y}_i$ are defined to derive the error system dynamics of the i^{th} active load. The dynamics of the energy error state is given by,

$$\dot{x}_{i,1} = E_i^2 x_{i,2} \tag{5.12}$$

The dynamics of the input admittance error state is given by,

$$\dot{x}_{i,2} = u_i + \frac{2P_i}{E_i^3}\dot{E}_i \tag{5.13}$$

Since, $\dot{E}_i = (\nabla_y E_i)\dot{y}$ and $\dot{y} = u$, where $y \in \mathbb{R}^n$ is the vector of input admittance, $u \in \mathbb{R}^n$ is the total control vector in the MG, and ∇_y is the gradient with respect to y, (5.13) can be

rewritten as,

$$\dot{x}_{i,2} = u_i + \frac{2P_i}{E_i^3}(\nabla_y E_i)u \tag{5.14}$$

Then, the dynamics of the i^{th} active load can be represented as,

$$\dot{x}_i = f_i(x_i) + Bu_i + Z_i(X, u) \tag{5.15}$$

where, $x_i = \begin{bmatrix} x_{i,1} & x_{i,2} \end{bmatrix}^T$, $f_i(x_i) = \begin{bmatrix} E_i^2 x_{i,2} & 0 \end{bmatrix}^T$, $B = \begin{bmatrix} 0 & 1 \end{bmatrix}^T$, $Z_i(X, u) = 2BP_i(\nabla_y E_i)u/E_i^3$ is the interconnected coupling term and $X = \begin{bmatrix} x_1^T & x_2^T & ... & x_n^T \end{bmatrix}^T \in \mathbb{R}^{2n}$ is the overall system state. The saturation bounds of the control input is given by the constraint imposed on the duty cycle which is $0 \leq D_i \leq 1$. From (5.9), the control input bound can be expressed as,

$$\Big(1 - \frac{v_i}{E_i}\Big)\frac{1}{L_i} \leq u_i \leq \frac{1}{L_i} \tag{5.16}$$

Suppose that the minimum output voltage of all the active loads are $2E_i$, i.e $\bar{v}_i \geq 2E_i$. This is true because the PEI is a boost converter. Then the control input can be bounded as, $\|u_i\| \leq \bar{u}_i = \frac{1}{L_i}$.

5.3 Decentralized Feedback Optimal Controller

In the decentralized control architecture introduced in this chapter, local feedback optimal controls are obtained for the isolated active loads. Isolated active load dynamics are obtained by letting the interconnected coupling terms to zero as,

$$\dot{x}_i = f_i(x_i) + Bu_i \tag{5.17}$$

The interconnected coupling term $Z_i(X, u)$ contains the gradient with respect to input admittances. Therefore, it is highly coupled with other active load admittances and if one considers this term for the controller development, it would be impossible to derive a decentralized controller. As an alternative, the isolated subsystem is obtained without the other load player influences by eliminating the coupling term as shown in (5.17). Then, the optimal controller is derived for this isolated subsystem and it is a decentralized controller. Next, this decentralized optimal feedback controller is applied to the actual system with

the coupling term in (5.15). Later it will be shown that, under the decentralized optimal controller obtained for the isolated subsystem given by (5.17), the original dynamics of the actual active load presented in (5.15) can be stabilized. Further, under this local feedback optimal control actions, the stability of the entire MG will also be shown. Infinite horizon feedback optimal control of the i^{th} isolated active load is explained in the next section.

5.3.1 Infinite Horizon Optimal Control of Isolated Active Loads

Once the isolated load dynamics are obtained as in (5.17), the goal of each active load is to drive its state to zero by solving the infinite horizon optimal control problem. The objective of the infinite horizon optimal control problem is to find a feedback control signal $(u_i^*(x_i))$ which minimizes the performance index,

$$J_i(x_i, u_i) = \int_{t_0}^{\infty} r_i(x_i(\tau), u_i(\tau))d\tau \tag{5.18}$$

such that,

$$u_i^*(x_i) = \underset{u_i(\tau)\in\Omega_i^u|\tau\in\mathbb{R}_{\geq t}}{\arg\min} \int_{t}^{\infty} r_i(x_i(\tau), u_i(\tau))d\tau \tag{5.19}$$

where, $\Omega_i^u = \{u_i | u_i \in \mathbb{R}, |u_i(x_i)| \leq \bar{u}_i\}$ and the instantaneous cost is defined as,

$$r_i(x_i, u_i) = Q_i(x_i) + U_i(u_i) \tag{5.20}$$

where, $Q_i(x_i)$ is a positive definite (PD) function and $U_i(u_i)$ is a PD integral function. Since the goal is to regulate the error system states to zero, the quadratic state cost of the form $x_i^T P_i x_i$ is selected for $Q_i(x_i)$. Here, P_i is a PD symmetric matrix with appropriate dimension. In order to satisfy the control input constraint, following non quadratic penalty function is employed for $U_i(u_i)$ [157, 158].

$$U_i(u_i) = 2R_i\bar{u}_i \int_0^{u_i} \tanh^{-1}(\zeta/\bar{u}_i)d\zeta \tag{5.21}$$

where, R_i is a positive constant. Closed form solution to the derived optimal control problem is characterized by the optimal value function given by [128],

$$V_i^*(x_i) = \min_{u_i(\tau)\in\Omega_i^u | \tau\in\mathbb{R}_{\geq t}} \int_t^\infty r_i(x_i(\tau), u_i(\tau))d\tau \tag{5.22}$$

The optimal value function satisfies the Hamilton Jacobi Bellman (HJB) equation [128] such that,

$$H_i(x_i, u_i) : \min_{u_i\in\Omega_i^u} \left[\nabla V_i^*(x_i)(f_i(x_i) + Bu_i(x_i)) + r_i(x_i, u_i)\right] = 0 \tag{5.23}$$

where, ∇ is the gradient operator with respect to x_i. If the optimal controller $(u_i^*(x_i))$ exists, according to (5.23), the HJB equation can be shown as,

$$\nabla V_i^*(x_i)(f_i(x_i) + Bu_i^*(x_i)) + r_i(x_i, u_i^*(x_i)) = 0 \tag{5.24}$$

with the initial condition $V_i^*(0) = 0$. The optimal control law which satisfies the HJB equation can be obtained by differentiating the Hamiltonian (H_i) in (5.23) with respect to u_i as,

$$u_i^*(x_i) = -\bar{u}_i \tanh\left[\frac{1}{2R_i\bar{u}_i}\nabla V_i^*(x_i)B\right] \tag{5.25}$$

Since the hyperbolic tangent function is a continuous, one to one bounded function such that $|\tanh(\cdot)| \leq 1$, the optimal control policy derived in (5.25) satisfies $|u_i| \leq \bar{u}_i$. Further, the second derivative of the Hamiltonian can be shown as, $2R_i\bar{u}_i\nabla_{u_i}(\tanh^{-1}(u_i/\bar{u}_i))$. Also, the hyperbolic tangent function is strictly monotonically increasing, the second derivative is positive [55]. This implies $u_i^*(x_i)$ given in (5.25) minimizes the Hamiltonian.

5.3.2 Local Stability of the Isolated Active Loads

Consider the candidate Lyapunov function of the i^{th} isolated active load $\mathcal{V}_i : \mathbb{R}^2 \to \mathbb{R}_{\geq 0}$,

$$\mathcal{V}_i(x_i) = V_i^*(x_i) \tag{5.26}$$

Optimal value function is a candidate Lyapunov function [54]. The first time derivative of $\mathcal{V}_i(x_i)$ along its dynamics under the optimal controller can be shown as,

$$\dot{\mathcal{V}}_i(x_i) = \nabla V_i^*(x_i)(f_i(x_i) + Bu_i^*(x_i)) \tag{5.27}$$

From (5.24), the Lyapunov derivative can be further shown as,

$$\dot{\mathcal{V}}_i(x_i) = -r_i(x_i, u_i^*(x_i)) = -\Big(Q_i(x_i) + U_i(u_i)\Big) \leq 0 \tag{5.28}$$

Positive definiteness of $Q_i(x_i)$ and $U_i(u_i)$ make the Lyapunov derivative negative definite which implies the asymptotic stability of the origin under the decentralized feedback optimal controller.

5.3.3 Stability of the Interconnected System with the Decentralized Optimal Controller

The stability of the interconnected dynamics can be analyzed by considering the actual load dynamics given in (5.15) with the total Lyapunov function $\mathcal{V}(X) : \mathbb{R}^{2n} \to \mathbb{R}_{\geq 0}$,

$$\mathcal{V}(X) = \sum_{i=1}^{n} d_i V_i^*(x_i), \quad d_i > 0 \tag{5.29}$$

Taking the first time derivative and utilizing (5.24) and (5.28), the Lyapunov derivative can be expressed as,

$$\dot{\mathcal{V}}(X) \leq -\sum_{i=1}^{n} d_i \alpha_i \psi^2(x_i) + \sum_{i=1}^{n} d_i \nabla V_i^*(x_i) Z_i(X) \tag{5.30}$$

where, $\alpha_i > 0$ are minimum eigenvalues of P_i and $\psi^2(x_i) = \|x_i\|^2$. Define a closed ball $B_r \subset \mathbb{R}^{2n}$ with radius r centered at the origin. Suppose, there exist positive constants $\beta_i > 0$ and $\gamma_{ij} > 0$ such that, $\forall i$ and $\forall\ \|x\| < r$,

$$\|\nabla V_i^*(x_i)\| \leq \beta_i \psi(x_i) \tag{5.31}$$

$$\|Z_i(X)\| \leq \sum_{j=1}^{n} \gamma_{ij} \psi(x_j) \tag{5.32}$$

Then, the Lyapunov derivative can be upper bounded as [163],

$$\dot{\mathcal{V}}(X) \leq -\frac{1}{2} \Psi^T \big(DS + S^T D\big) \Psi \tag{5.33}$$

where, $\Psi = \begin{bmatrix} \psi(x_1) & ... & \psi(x_n) \end{bmatrix}^T$, $D = diag(d_1, ..., d_n)$, and S is an $n \times n$ matrix with the elements $s_{ij} = \alpha_i - \beta_i \gamma_{ii}$ *when* $i = j$ and $s_{ij} = \beta_i \gamma_{ij}$ *when* $i \neq j$. Hence, if there exists a positive diagonal matrix D such that $DS + S^T D > 0$, then the Lyapunov derivative is negative definite. According to [163], if the matrix S is an M-matrix, which means the leading principle minors of S are positive, then there exist a positive diagonal matrix D such that $DS + S^T D > 0$ and therefore, the origin is asymptotically stable. Hence, active power regulation can be achieved by the proposed decentralized feedback optimal control algorithm while preserving the stability of the entire MG.

However, finding an exact analytical solution to the optimal value function is generally not possible [53–55]. Therefore, ADP based RL techniques have been proposed in the literature to obtain an approximate solution. In these methods, the optimal value function is approximated by NNs. Then, the unknown NN weights in the approximated value function are continuously updated to minimize the approximation error. The approximation error is called the Bellman Error (BE) or the temporal difference (TD) [53, 55]. In this chapter, two LIP NNs are employed to successively approximate the optimal value function and the optimal feedback control law as described in the next section.

5.4 Model Based Reinforcement Learning of the Decentralized Feedback Optimal Controller

5.4.1 Value Function Approximation

NNs are known for their effectiveness in unknown function approximation on prescribed compact sets [159]. The universal approximation property of NNs can be used to synthesize the optimal value function of the i^{th} active load in a compact set $\chi \subset \mathbb{R}^2$ as,

$$V_i^*(x_i) = W_i^T \sigma(x_i) + \epsilon_i(x_i) \tag{5.34}$$

where, $W_i \in \mathbb{R}^L$ is the ideal NN weight vector bounded by a known constant such that $\|W_i\| \leq \overline{W}$ $\forall i$, $L \in \mathbb{N}$ is the number of neurons, $\sigma(x_i) : \mathbb{R}^2 \rightarrow \mathbb{R}^L$ is a continuously differentiable activation function having the properties $\sigma(0) = 0$ and $\nabla\sigma(0) = 0$. Even though, same activation function and number of neurons are utilized in this chapter, different active loads can be assigned different activation functions and number of neurons without

loss of generality. The function reconstruction error is given by $\epsilon_i(x_i)$ which is bounded in the sense $\forall i$, $\sup_{x_i \in \chi} |\epsilon_i(x_i)| \leq \bar{\epsilon}$ and $\sup_{x_i \in \chi} |\nabla \epsilon_i(x_i)| \leq \bar{\epsilon}'$ [55]. With this NN representation, the derived optimal controller can be expressed as,

$$u_i^*(x_i) = -\bar{u}_i \tanh\Big[\frac{1}{2R_i\bar{u}_i}\Big(W_i^T \nabla\sigma(x_i) + \nabla\epsilon_i(x_i)\Big)B\Big] \tag{5.35}$$

Since the ideal NN wight vector W_i is unknown, an approximate set of weights are assigned to estimate the value function and the optimal control law as,

$$\hat{V}_i(x_i, \hat{W}_{c,i}) = \hat{W}_{c,i}^T \sigma(x_i) \tag{5.36}$$

$$\hat{u}_i(x_i, \hat{W}_{a,i}) = -\bar{u}_i \tanh\Big[\frac{1}{2R_i\bar{u}_i}\hat{W}_{a,i}^T \nabla\sigma(x_i)B\Big] \tag{5.37}$$

where, the critic and actor weights are given by $\hat{W}_{c,i} \in \mathbb{R}^L$ and $\hat{W}_{a,i} \in \mathbb{R}^L$ respectively. These are the estimates of actual weights W_i. Substituting the approximated value function and optimal controller in (5.24), the BE of the i^{th} active load can be expressed as,

$$\begin{aligned}\delta_i(x_i, \hat{W}_{c,i}, \hat{W}_{a,i}) = {} & \nabla\hat{V}_i(x_i, \hat{W}_{c,i})\Big(f_i(x_i) + B\hat{u}_i(x_i, \hat{W}_{a,i})\Big) \\ & + Q_i(x_i) + 2R_i\bar{u}_i\Big[\hat{u}_i(x_i, \hat{W}_{a,i})\tanh^{-1}\Big(\frac{\hat{u}_i(x_i, \hat{W}_{a,i})}{\bar{u}_i}\Big) \\ & + \frac{\bar{u}_i}{2} ln\Big(1 - \Big(\frac{\hat{u}_i(x_i, \hat{W}_{a,i})}{\bar{u}_i}\Big)^2\Big)\Big]\end{aligned} \tag{5.38}$$

The goal is to develop an adaptive update algorithm to tune the estimated NN weights to minimize the BE simultaneously. In order to ease the complexity of the problem, two sets of weights (actor and critic) are used to estimates the same unknown ideal weights. With this modification, critic weights appear linearly in the BE which allows employing least square (LS) based update law [52, 55].

5.4.2 Model Based Reinforcement Learning

Concurrent learning-based adaptive update laws are proposed in this section to tune the weights in actor and critic NNs. In online ADP techniques, the weights are updated based on the observed data along the system trajectories [53, 55]. In order to learn the actual

NN weights, parameter convergence is required [53, 55]. To gain the parameter convergence, sufficient richness in the observed data must exist [52]. This richness is characterized by PE [52]. Typically a probing noise is added to the controller to make the regressor PE [54,165]. However, the addition of probing noise is undesirable in MG control. In contrast, this dissertation utilizes a concurrent learning-based adaptive learning algorithm which only requires relaxed PE like rank condition to guarantee parameter convergence to a neighborhood of the ideal weights [55, 161]. Instead of adding a probing noise to the control input, this method uses a virtual excitation in the adaptive algorithm. It utilizes the system model to extrapolate the BE to unexplored areas of the state space and uses that information as a gained experience for learning in the virtual excitation. The proposed adaptive law based on the LS with forgetting factor is given by [52, 55, 162],

$$\dot{\hat{W}}_{c,i}(t) = -k_{c1,i}\Gamma_i(t)\frac{\phi_i(t)}{\rho_i(t)}\delta_i(t) - \frac{k_{c2,i}}{M}\Gamma_i(t)\sum_{k=1}^{M}\frac{\phi_{k,i}(t)}{\rho_{k,i}(t)}\delta_{k,i}(t) \tag{5.39}$$

$$\dot{\Gamma}_i(t) = \Big(\beta_i\Gamma_i(t) - k_{c1,i}\Gamma_i(t)\frac{\phi_i(t)\phi_i^T(t)}{\rho_i^2(t)}\Gamma_i(t) - \frac{k_{c2,i}}{M}\Gamma_i(t)\sum_{k=1}^{M}\frac{\phi_{k,i}(t)\phi_{k,i}^T(t)}{\rho_{k,i}^2(t)}\Gamma_i(t)\Big)\mathbb{1}_{\|\Gamma_i(t)\|\leq\overline{\Gamma}} \tag{5.40}$$

$$\dot{\hat{W}}_{a,i}(t) = -k_{a,i}\Big(\hat{W}_{a,i}(t) - \hat{W}_{c,i}(t)\Big) \tag{5.41}$$

where, the regressor is $\phi_i(t) = \nabla\sigma(x_i)\Big(f_i(x_i) + B\hat{u}_i(x_i, \hat{W}_{a,i})\Big) \in \mathbb{R}^L$, normalization term is $\rho_i(t) = 1 + \nu_i\phi_i^T(t)\Gamma_i(t)\phi_i(t) \in \mathbb{R}$. The time varying LS gain matrix is given by $\Gamma_i(t) \in \mathbb{R}^{L\times L}$, and $\mathbb{1}$ is the indicator function with the saturating upper bound $\overline{\Gamma}$ for all $\Gamma_i(t)$ $\forall i$. The constant β is the forgetting factor [52], $k_{c1,i}$, $k_{c2,i}$, $k_{a,i}$, ν_i are positive constant gains. Moreover, $\phi_{k,i}(t) = \nabla\sigma(x_{k,i})\Big(f_i(x_{k,i}) + B\hat{u}_i(x_{k,i}, \hat{W}_{a,i})\Big) \in \mathbb{R}^L$, $\rho_{k,i}(t) = 1 + \nu_i\phi_{k,i}^T(t)\Gamma_i(t)\phi_{k,i}(t) \in \mathbb{R}$ and $\delta_{k,i}(t) = \delta_i(x_{k,i}, \hat{W}_{c,i}, \hat{W}_{a,i})$ are the k^{th} extrapolated regressor, normalizing term and the BE of the i^{th} active load evaluated at the predefined set of points in the state space $x_{k,i}$. It is assumed that the predefined set points satisfy the following rank condition [55]. For each

$i \in \mathcal{L}$, there exists a finite set of fixed points $\{x_{k,i} \in \mathbb{R}^2 | k = 1, \ldots, M\}$ such that $\forall t \in \mathbb{R}_{\geq 0}$,

$$0 < \underline{c}_i \triangleq \frac{1}{M} \left(\inf_{t \in \mathbb{R}_{\geq 0}} \left(\lambda_{min} \left\{ \sum_{k=1}^{M} \frac{\phi_{k,i}(t) \phi_{k,i}^T(t)}{\rho_{k,i}^2(t)} \right\} \right) \right) \tag{5.42}$$

This PE like rank condition will be used in the subsequent stability analysis to show the parameter convergence. The critic and LS gain update laws are similar to the update laws used in chapter 4. However, a simplified actor weight update law is employed in this chapter.

5.4.3 Stability of the Adaptive Update Laws

The Lyapunov stability analysis of the error state, actor and critic weight estimates is similar to the one already done in chapter 4 and briefly discussed in this section. In the subsequent analysis, the indicator i and function dependency on state and time are suppressed for notational brevity. The procedure is similar for all the individual active loads in the set $\mathcal{L}$. Consider a closed ball centered at the origin $B_\varrho \subset \mathbb{R}^{2(1+L)}$. The radius of the ball is ϱ and let $\chi \triangleq B_\varrho \cap \mathbb{R}^2$. Subtracting (5.38) from (5.24), an unmeasurable form of the BE (δ) and extrapolated BE (δ_k) can be expressed as,

$$\delta = -\phi^T \tilde{W}_c - \bar{u} \tanh(\hat{D}_a) G_\sigma^T \tilde{W}_a + R\bar{u}^2 \ln \left[\frac{1 - \tanh^2(\hat{D}_a)}{1 - \tanh^2(\hat{D}_a^*)} \right] - \nabla \epsilon f \tag{5.43}$$

$$\delta_k = -\phi_k^T \tilde{W}_c - \bar{u} \tanh(\hat{D}_{ak}) G_{\sigma k}^T \tilde{W}_a + R\bar{u}^2 \ln \left[\frac{1 - \tanh^2(\hat{D}_{ak})}{1 - \tanh^2(\hat{D}_{ak}^*)} \right] - \nabla \epsilon_k f_k \tag{5.44}$$

where, $G_\sigma = \nabla \sigma(x) B$, $G_{\sigma k} = \nabla \sigma(x_k) B$, $\hat{D}_a = G_\sigma^T \hat{W}_a / 2R\bar{u}$, $\hat{D}_{ak} = G_{\sigma k}^T \hat{W}_a / 2R\bar{u}$, $\tilde{W}_c = W - \hat{W}_c$ and $\tilde{W}_a = W - \hat{W}_a$ are the critic and actor weight estimation errors, $\nabla \epsilon_k = \nabla \epsilon(x_k)$, $f_k = f(x_k)$, $\nabla \sigma_k = \nabla \sigma(x_k)$, $\hat{D}_a^* = (W^T \nabla \sigma + \nabla \epsilon) B / 2R\bar{u}$ and $\hat{D}_{ak}^* = (W^T \nabla \sigma_k + \nabla \epsilon_k) B / 2R\bar{u}$. Consider the continuously differentiable PD Lyapunov candidate $\mathcal{V}_L : \mathbb{R}^{2(1+L)} \times \mathbb{R}_{\geq 0} \to \mathbb{R}_{\geq 0}$,

$$\mathcal{V}_L(\mathcal{Z}, t) = V^*(x) + \frac{1}{2} \tilde{W}_c^T \Gamma^{-1} \tilde{W}_c + \frac{1}{2} \tilde{W}_a^T \tilde{W}_a \tag{5.45}$$

where, V^* is the optimal value function, and the concatenated error state and weight estimation error vector is given as $\mathcal{Z} = \begin{bmatrix} x^T & \tilde{W}_c^T & \tilde{W}_a^T \end{bmatrix}^T \in \mathbb{R}^{2(1+L)}$. Due to the positive definiteness of V^* and boundedness of the LS gain matrix such that $\underline{\Gamma} I_L \leq \Gamma(t) \leq \overline{\Gamma} I_L$ [55, 162], the candidate

Lyapunov function $\mathcal{V}_L$ is bounded as [163],

$$\underline{v}_L(\|\mathcal{Z}\|) \leq \mathcal{V}_L(\mathcal{Z},t) \leq \bar{v}_L(\|\mathcal{Z}\|) \tag{5.46}$$

where, $\underline{v}_L$ and $\bar{v}_L$ are class $\mathcal{K}$ functions. Define the notation $\overline{|\omega|} \triangleq \sup_{x\in\chi}\|\omega\|$ and a positive constant $\underline{C}$ as,

$$\underline{C} = \frac{\beta}{2\overline{\Gamma}k_{c2}} + \frac{\underline{c}}{2} \tag{5.47}$$

Then, using the BEs in (5.43) and (5.44), time derivative of $\mathcal{V}_L(\mathcal{Z},t)$ along the dynamics (5.17), (5.39) - (5.41) can be upper bounded as,

$$\dot{\mathcal{V}}_L \leq -r^*(x) - k_{c2}\underline{C}\|\tilde{W}_c\|^2 - k_a\|\tilde{W}_a\|^2 + \gamma(k_{c1}+k_{c2})\overline{\Delta}\|\tilde{W}_c\| + \left[k_a + 2\bar{u}\gamma(k_{c1}+k_{c2})\overline{|G_\sigma|}\right]\|\tilde{W}_a\|\|\tilde{W}_c\| \tag{5.48}$$

where, $\overline{\Delta} = \bar{u}\Big(2\overline{W}\overline{|G_\sigma|} + \overline{|\nabla\epsilon B|}\Big) + R\bar{u}^2\bar{\epsilon}_D + \overline{|\nabla\epsilon f|}$ and γ is the upper bound of the normalized regressor such that $\|\frac{\phi}{\rho}\| \leq \gamma$ [55]. The approximation $\ln\Big[1-\tanh^2(D)\Big] = \ln(4) - 2Dsgn(D) + \epsilon_D$ [158] is employed in (5.48) for the bounded approximation error $\epsilon_D \leq \bar{\epsilon}_D$ for $D = \{\hat{D}_a, \hat{D}_a^*\}$. Define positive constants $\{\lambda_j | j = 1,\ldots,5\}$ such that $\lambda_1+\lambda_2+\lambda_3 = 1$ and $\lambda_4+\lambda_5 = 1$. Sufficient conditions for the UUB are given as,

$$2\sqrt{k_a k_{c2}\underline{C}\lambda_3\lambda_5} \geq k_a + 2\bar{u}\gamma(k_{c1}+k_{c2})\overline{|G_\sigma|} \tag{5.49}$$

$$v_L^{-1}(\vartheta) < \bar{v}_L^{-1}(\underline{v}_L(\varrho)) \tag{5.50}$$

where, ϑ is a positive constant and v_L is any class $\mathcal{K}$ PD function defined as,

$$\vartheta = \frac{\Big(\gamma(k_{c1}+k_{c2})\overline{\Delta}\Big)^2}{4k_{c2}\underline{C}\lambda_2} \tag{5.51}$$

$$v_L(\|\mathcal{Z}\|) \leq \frac{1}{2}\Big(r^*(x) + k_{c2}\underline{C}\lambda_1\|\tilde{W}_c\|^2 + k_a\lambda_4\|\tilde{W}_a\|^2\Big) \tag{5.52}$$

Under the sufficient conditions, $\dot{\mathcal{V}}_L$ can be further upper bounded as,

$$\dot{\mathcal{V}}_L \leq -v_L(\|\mathcal{Z}\|), \quad \forall\|\mathcal{Z}\| > v_L^{-1}(\vartheta) \tag{5.53}$$

for all $\mathcal{Z} \in B_\varrho$ and $t \geq 0$. Therefore, the concatenated state and weight estimation error system $\mathcal{Z}$ is UUB in the sense $\lim_{t\to\infty} \sup \|\mathcal{Z}\| \leq \underline{v}_L^{-1}(\bar{v}_L(v_L^{-1}(\vartheta)))$ [163].

5.5 Simulation Study

Series of simulations were carried out in Matlab/Simulink considering the IEEE 9 bus system given in [3] with three active loads. All the active load parameters were considered same and given by, $L_i = 500$ μH and $C_i = 120$ μF. Active load power demands were considered as 0.8 p.u, 1.0 p.u and 1.2 p.u for load 1, 2 and 3 connected to bus 5, 6 and 8 respectively. All source voltages were kept fixed at 1 p.u and distribution line resistances were considered as 0.01 p.u. Desired per unit energy storage of all the loads were set to 1 p.u. Base values of voltage, power, capacitance and inductance were considered as 110 V, 1000 W, 240 μF and 20 mH respectively. Controller parameters were considered as, $\beta = 0.3$, $k_{c1,i} = 10$, $k_{c2,i} = 20$, $k_{a,i} = 20$, $\nu_i = 0.05$, $R_i = 1$ and P_i identity matrix for all $i \in \mathcal{L}$. Value function of each active load is approximated by a quadratic power series of system states. Hence, the activation function was selected as $\sigma(x_i) = \begin{bmatrix} x_{i,1}^2 & x_{i,2}^2 & x_{i,1}x_{i,2} \end{bmatrix}^T$. Initial conditions for both the actor and critic weights were considered as 15 and the least square gain matrix was initialized with $100I_{3\times 3}$.

5.5.1 Startup Transient

This test case shows the active load behavior during the startup phase of the MG. It is assumed that all the loads are disconnected from the load buses at the beginning of the simulation and hence, initial values of the admittance are zero. Variation of the states, input bus voltages, and input powers are shown in Figure 5.2. All the internal energy states reach the desired value of 1 p.u in 6s as seen in Figure 5.2 (a). Similarly, all input admittances converge to their steady-state (s.s) values within 6s as shown in Figure 5.2 (b). Steady state input admittances of load 1, 2 and 3 can be observed as 0.823 p.u, 1.03 p.u and 1.24 p.u. In order to maximize the input power to the load during the startup, input admittance increases rapidly during the initial transient. Due to this sudden increment, overshoots can be observed in all the active load input admittances. Load bus voltage variations are illustrated in Figure 5.2 (c) where the s.s input voltages are found as 0.986 p.u, 0.985 p.u, and 0.984

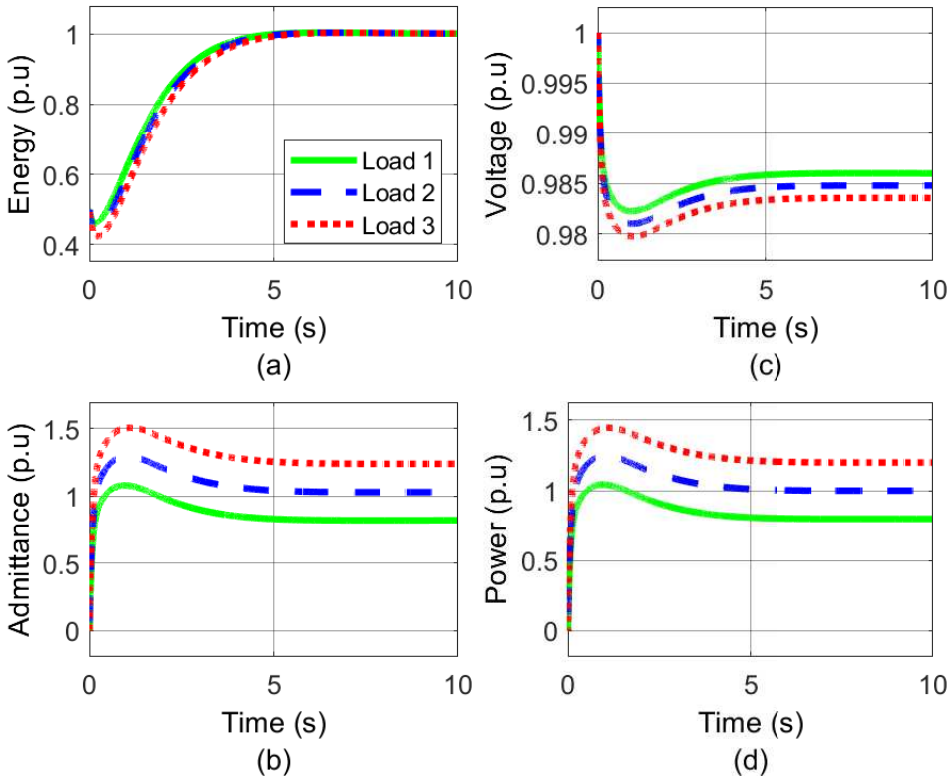

Figure 5.2: Variation of states, input voltages and powers during the startup (a) Stored energy, (b) Input admittance, (c) Input voltage and (d) Input power.

p.u. According to the input power variations given in Figure 5.2 (d), all initial input powers are zero since loads were disconnected from the bus at the beginning. Gradually, the input powers built up and after 6s, those reach their desired steady states. Overshoots exist in all the load input powers and the maximum is observed in load 3 which is equal to 1.45 p.u.

A comparison of the proposed controller against a model predictive controller (MPC) was carried out and results are shown in Figure 5.3. The MPC was designed using the Matlab/Simulink MPC controller block. Then Matlab/Simulink MPC designer tool has been used to tune the response with 0.1s sample time with a 10s prediction horizon. Compared to the proposed controller, MPC transient performances are not smooth. Further MPC learning process is relatively slow and large fluctuations can be seen in the admittance and hence in the input power. With the MPC, the internal energy consumption is higher compared to the proposed controller and load three reaches zero stored energy at 1.5s. Transient error state cost variations of active load one during the startup is shown in Figure 5.4. Similar

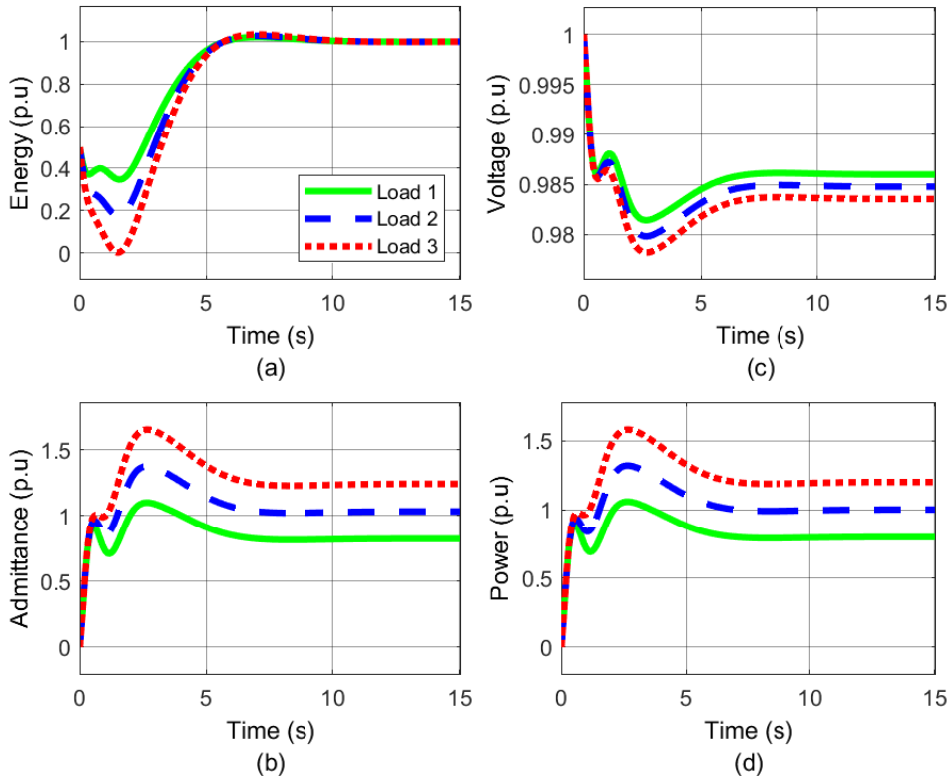

Figure 5.3: Variation of states, input voltages and powers during the startup with MPC (a) Stored energy, (b) Input admittance, (c) Input voltage and (d) Input power.

variations can be seen in the other loads as well. Clearly, the proposed controller shows lower transient cost compared to the MPC. The percentage improvement in the proposed controller with respect to the transient cost suppression at the startup is computed as 66.46%.

Actor and critic NN weight updates of active load 1 are shown in Figure 5.5. Similar variations can be seen in the other loads and they are not shown here for the sake of brevity. All weights were initialized with 15. Weight 1, 2 and 3 are converged to 2, 1.76 and 1.72 respectively.

To demonstrate the performance of the proposed concept with a more complex system, a simulation was carried out considering the modified IEEE 30 bus system [154]. The loads at bus 7, 8, 10, 12, 14 and 15 were considered as active loads with demands 0.8 p.u, 1 p.u, 1.2 p.u, 1.5 p.u, 0.5 p.u and 2 p.u respectively. All the other loads were set to constant impedance loads with 30 Ω. Variation of states and input powers are shown in Figure 5.6. All the system states converged to their respective equilibrium after 5s and demanded powers

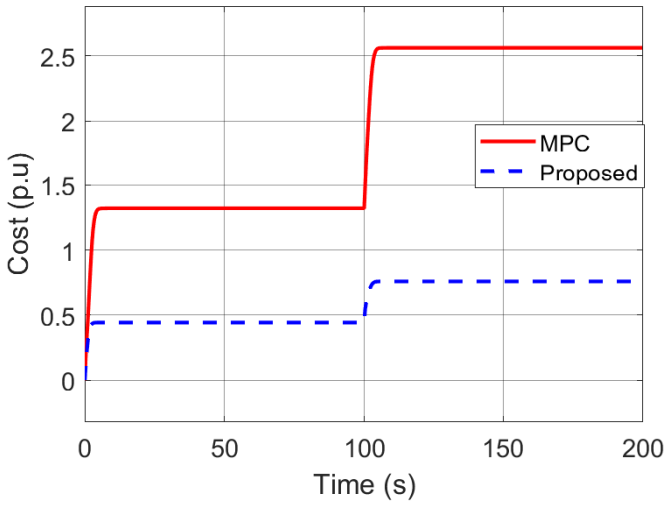

Figure 5.4: Variation of transient state cost of active load 1.

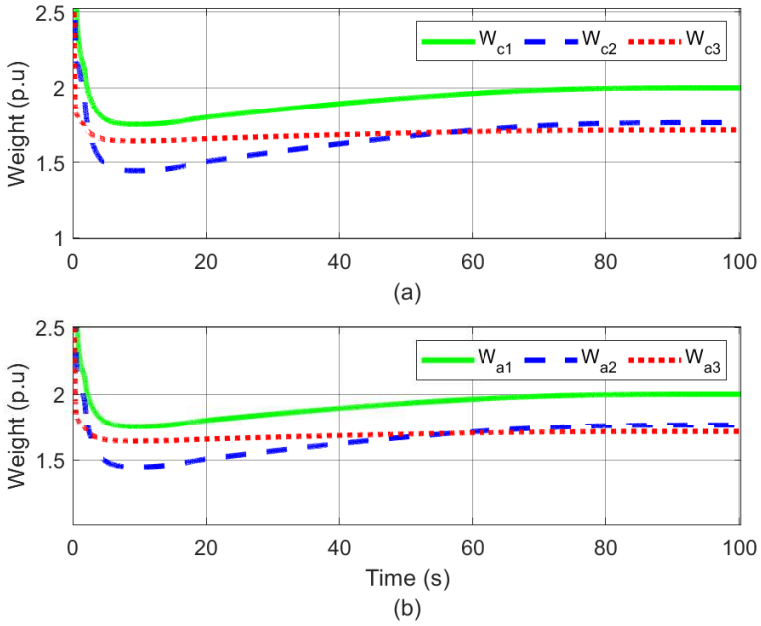

Figure 5.5: Variation of active load 1 NN weights during the startup (a) Critic and (b) Actor.

to all the active loads are delivered accordingly.

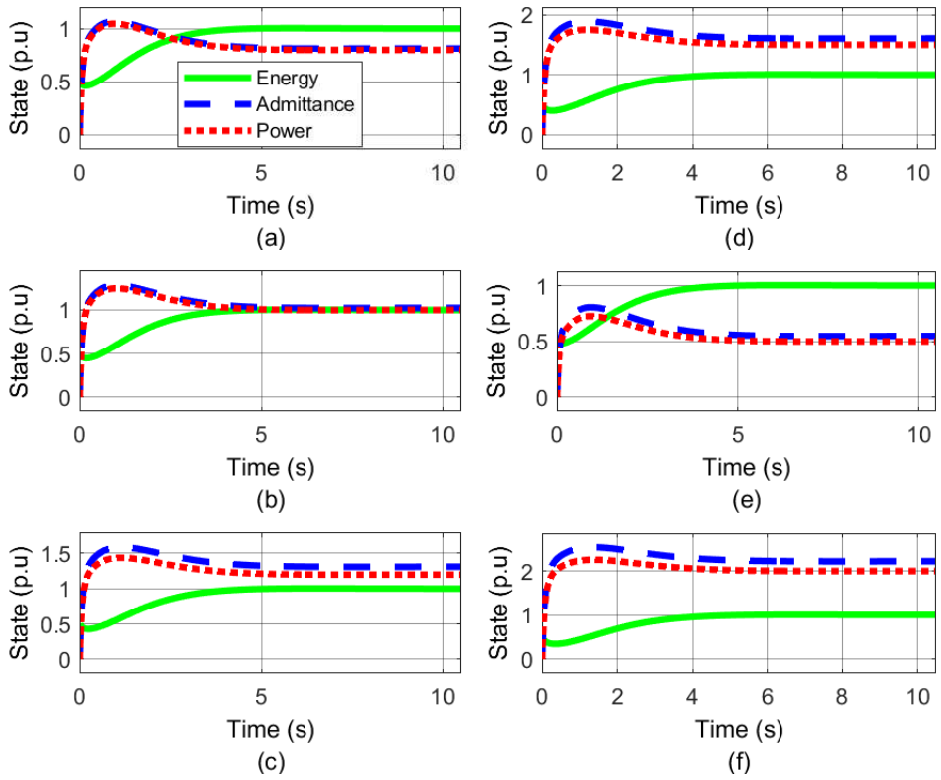

Figure 5.6: Variation of states and power during the startup in IEEE 30 bus system (a) Load 1, (b) Load 2, (c) Load 3, (d) Load 4, (e) Load 5 and (f) Load 6.

5.5.2 Active Load Demand Change

The adaptability of the proposed decentralized control law subjected to a load disturbance was examined in this test case. Load 1 power demand was changed from 0.8 p.u to 1.5 p.u at t = 100s and results are shown in Figure 5.7. Based on the results, it can be seen that, just after the abrupt load change, available input energy is not sufficient enough to satisfy the required load demand. Hence, internally stored energy needs to be utilized to compensate for the power deficiency as shown in Figure 5.7 (a). Due to this stored energy consumption, the internal energy drops from 1 p.u to 0.71 p.u in 1.1s. In the meantime, in order to maximize the energy input to the active load, input admittance increases according to the result shown in Figure 5.7 (b). At t = 101.1s, input admittance reaches a point where it can produces the demanded power to the load. Both energy and input admittance states of load one gain their respective equilibrium at 1 p.u and 1.56 p.u 8s after the disturbance. Further, slight changes can be observed in load two and three input admittances. Final input admittances of those

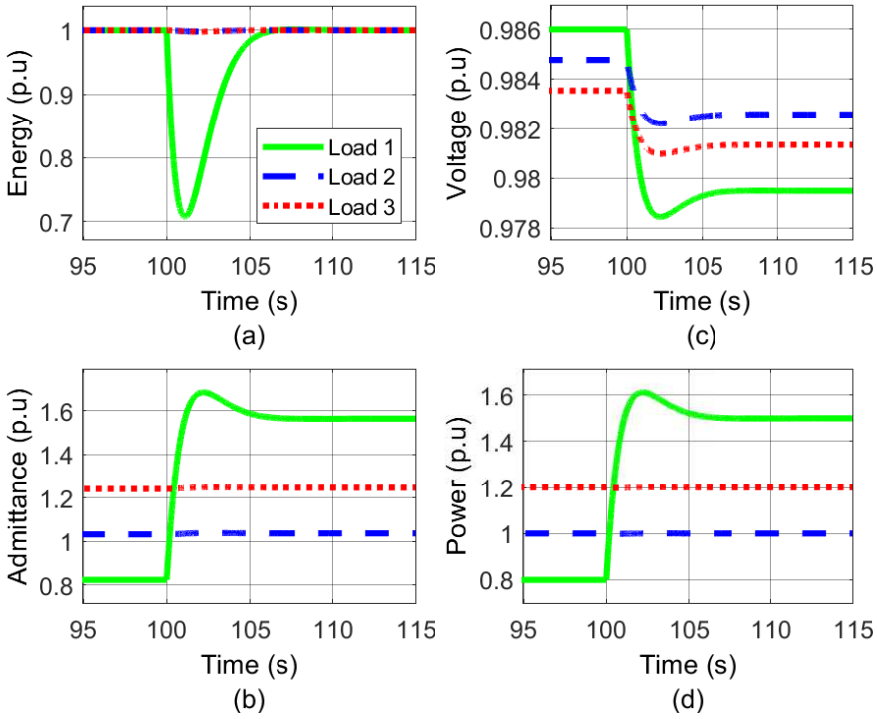

Figure 5.7: Variation of states, input voltages and powers in the load change (a) Stored energy, (b) Input admittance, (c) Input voltage and (d) Input power.

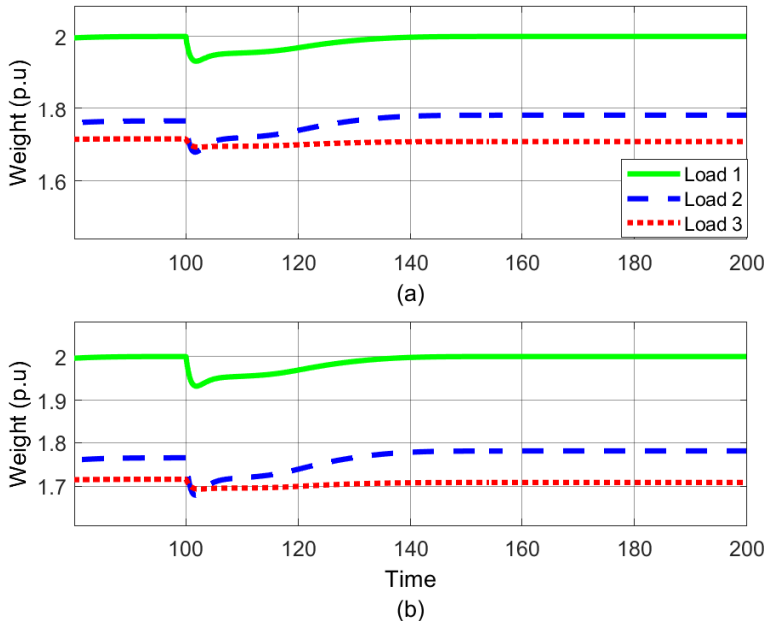

Figure 5.8: Active load 1 NN weights in the load change (a) Critic and (b) Actor.

are converged to 1.036 p.u and 1.246 p.u. Due to the demand change in load one, all the bus voltages are affected as depicted in Figure 5.7 (c). The maximum voltage drop can be observed in bus 5, where the load change occurred. The final input voltages of load 1, 2 and 3 are measured as 0.98 p.u, 0.983 p.u and 0.981 p.u. Input powers of load 2 and 3 are not affected by the demand change as expected. Within 8s, load 1 input power gains the desired value of 1.5 p.u. NN weight update process of the load 1 subjected to the demand change are shown in Figure 5.8. No change can be seen in weight 1. However, weight 2 and 3 are changed to 1.78 and 1.7.

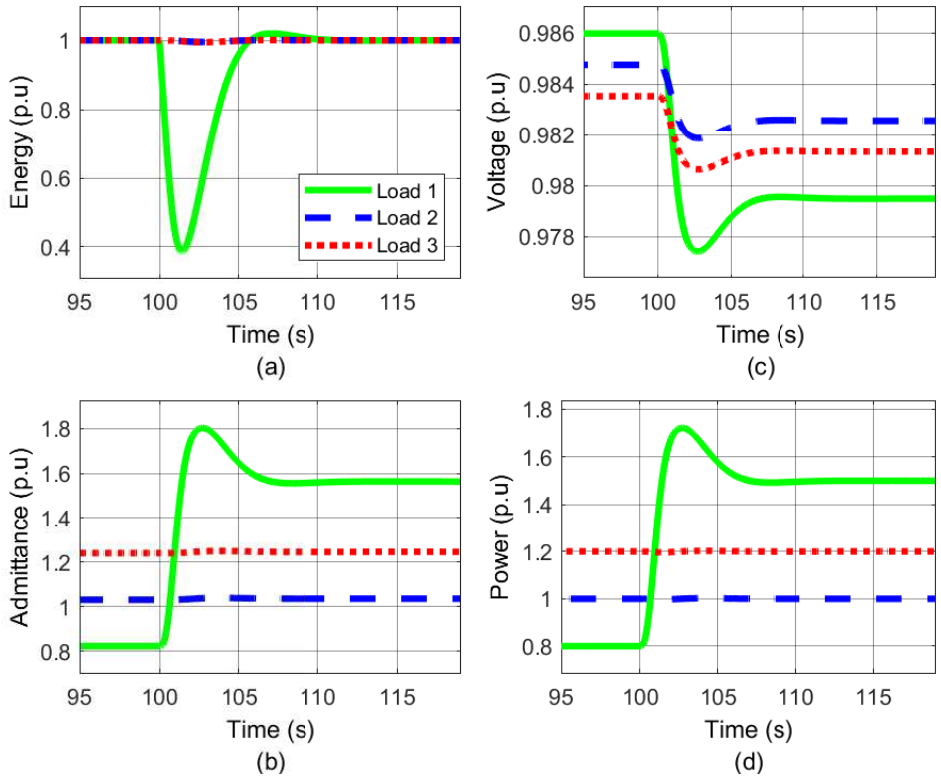

Figure 5.9: Variation of states, input voltages and powers in the load change with MPC (a) Stored energy, (b) Input admittance, (c) Input voltage and (d) Input power.

Comparative results with MPC is shown in Figure 5.9. As in the startup transient, the MPC utilizes a significant amount of stored energy. The percentage stored energy change in load 1 with the proposed controller and MPC are 29% and 61.4% respectively. Moreover, higher overshoots in admittance and input power can be observed in the MPC compared to the proposed controller. The transient error state cost variation of load 1 subjected to the

demand change is demonstrated in Figure 5.4 after 100s. Clearly, low transient cost can be observed in the proposed controller and the improvement against the MPC can be calculated as 70.36%.

5.5.3 Adaptability Against Source Disturbances - Limited Source Voltages

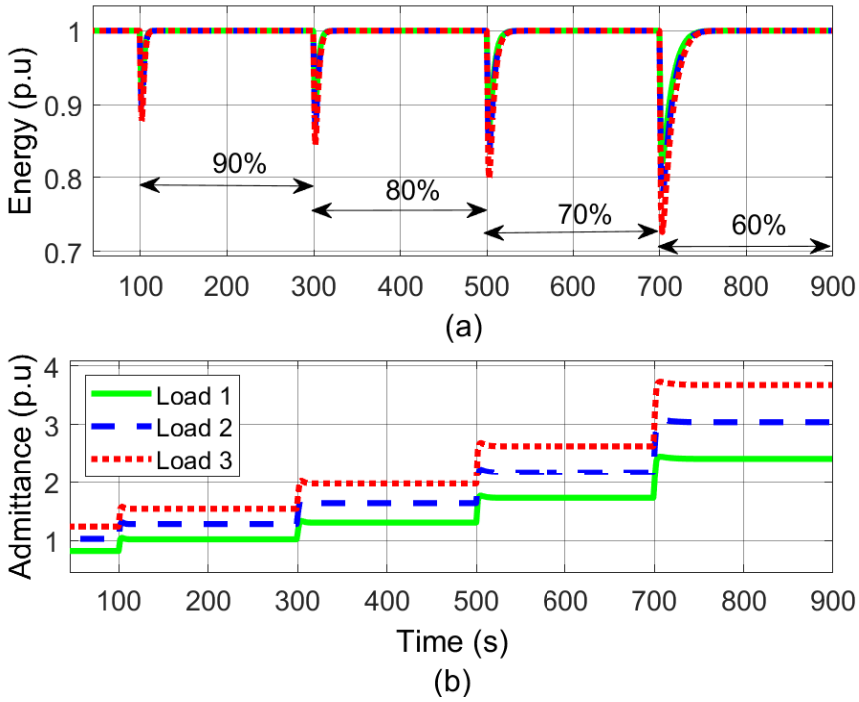

Figure 5.10: Variation of states under limited source voltages (a) Stored energy and (b) Input admittance.

The performance of the proposed concept under limited source voltages was investigated in this test case. Simulation results for 10% source voltage reduction in every 200s starting from t = 100s are given in Figure 5.10 and Figure 5.11. When the source voltage reduces, the load bus voltage goes down as seen by Figure 5.11 (a). Therefore, each time, input admittance increases to provide the required demand as shown by Figure 5.10 (b). During the transients, the internally stored energy is utilized to keep the demand at the required value as seen by Figure 5.10 (a). The internally stored energy state takes a longer time to reach the desired value when the input voltage is low. Each situation, variation in the input power shown in Figure 5.11 (b) is small and it reaches the demanded value in minimal time.

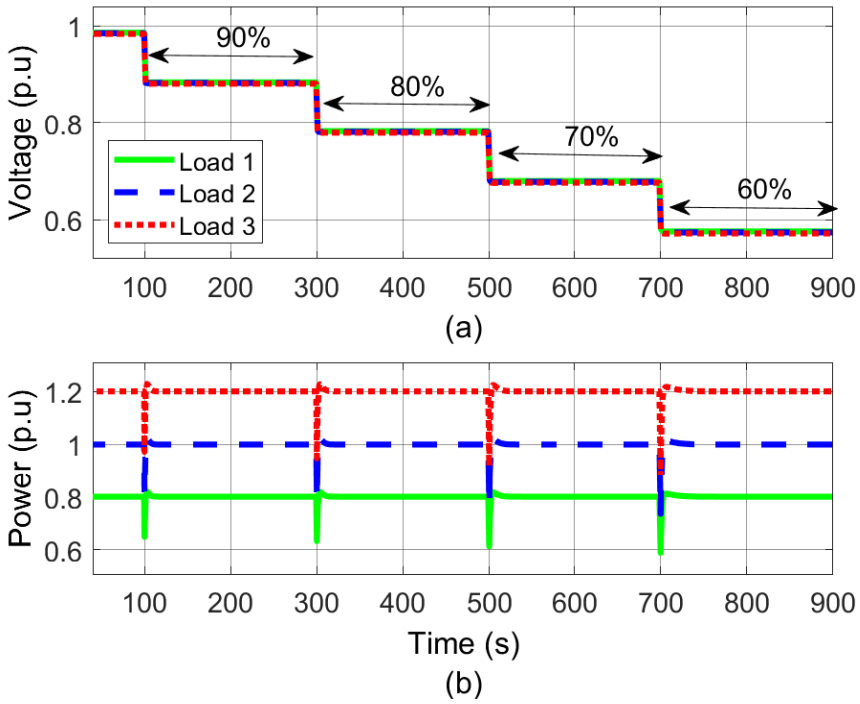

Figure 5.11: Variation of input voltages and powers under limited source voltages (a) Input voltage and (b) Input power.

According to the results, the proposed control algorithm is able to provide the CPL demand even under limited source voltages.

5.5.4 Adaptability Against Source Disturbances - Complete Blackout

A complete blackout was created by setting all the input source voltages to zero at t = 100s. Then the fault was cleared just before the critical clearing time which was found as 650ms for this test setup. During the fault period, all the desired input admittances were set to 10 p.u. Variation in the states, input voltages and powers are given in Figure 5.12 and Figure 5.13. Due to the blackout, all the input voltages and input powers become zero for a short time as seen from Figure 5.13. In order to provide the load demand, the internally stored energy is utilized in each active load as shown in Figure 5.12 (a). Within the fault period, energy states of load 1, 2 and 3 drop to 0.496 p.u, 0.37 p.u and 0.244 p.u. In contrast, input admittances increase to reach the desired value of 10 p.u and at the end of the fault period, maximum values of load 1, 2 and 3 admittances are 5.406 p.u, 5.506 and 5.607 p.u.

At the same time, corresponding maximum input powers are 4.618 p.u, 4.698 p.u and 4.778 p.u. After the fault has been cleared, the energy storage of all the loads rapidly increases and reaches the desired s.s after 20s. Maximum energy storage of 3.505 p.u can be observed in load 1 while 3.321 p.u and 3.137 p.u are observed in load 2 and 3 respectively.

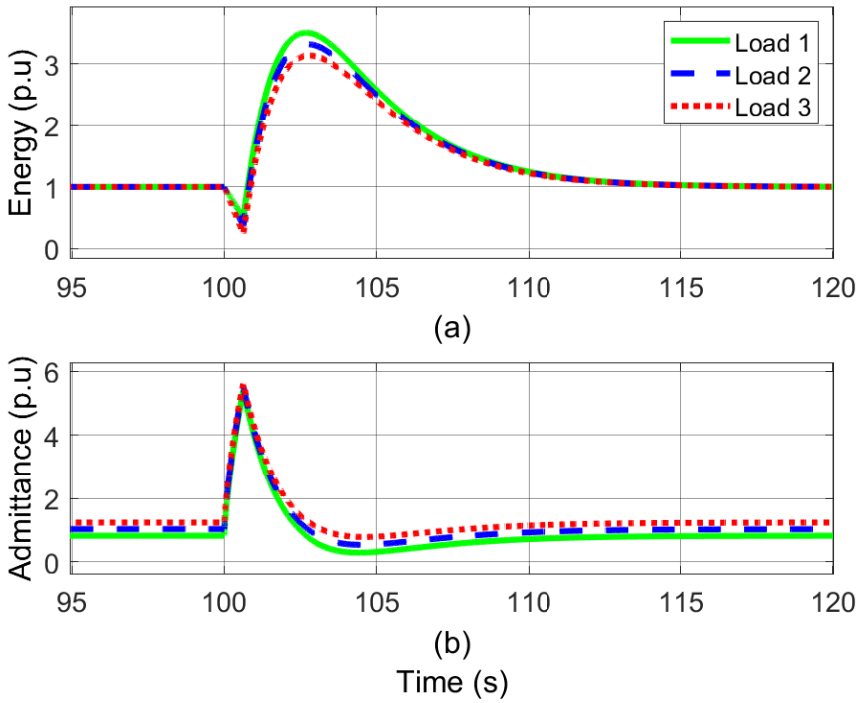

Figure 5.12: Variation of states subjected to a blackout (a) Stored energy and (b) Input admittance.

The adaptive nature of the proposed concept subjected to an insecure voltage which is manifested initially as a slow voltage decay following a sharp decline at the point of collapse is shown in Figure 5.14. In this scenario, the source voltages drop linearly from 1 p.u to 0.9 p.u in 10s and then suddenly collapse to zero. In order to supply the demand during the linear voltage drop, all input admittances increase their values. However, no change can be seen in the stored energy state. After the collapse at 110s, the variation is similar to the complete blackout test case. Within 20s, all the states regain their equilibrium and the demanded powers are delivered to the loads.

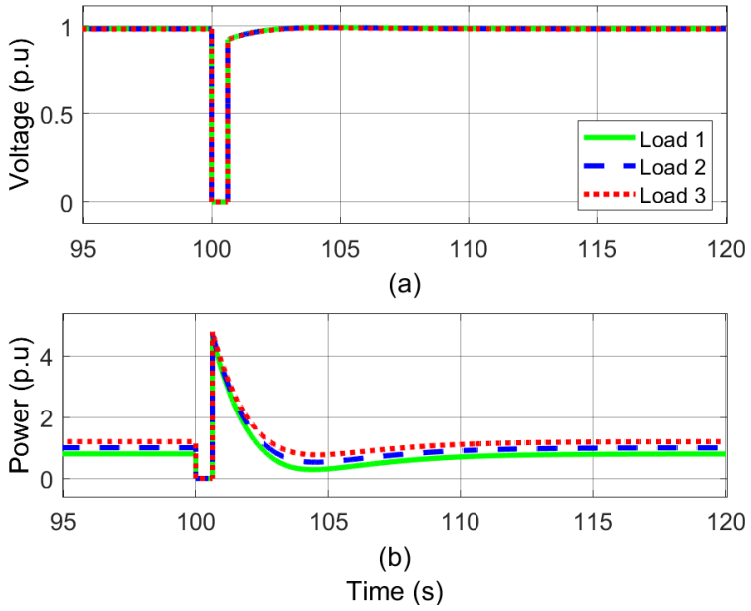

Figure 5.13: Variation of input voltages and powers subjected to a blackout (a) Input voltage and (b) Input power.

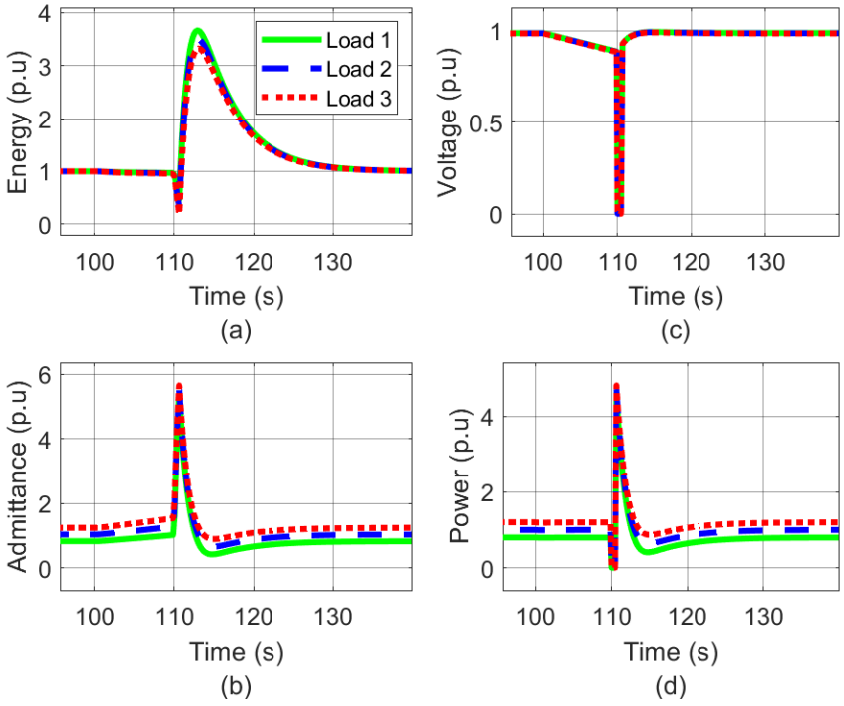

Figure 5.14: Variation of state, input voltages and powers subjected to a voltage collapse (a) Stored energy, (b) Input admittance, (c) Input voltage and (d) Input power.

5.5.5 Distribution Line Disconnection

The performance of the proposed concept under a fault in the distribution network was investigated and results are shown in this section. Suppose the distribution line between bus 8 and 9 in the IEEE 9 bus system was disconnected at t = 100s. Variation in the state, load bus voltages, and input powers are shown in Figure 5.15. Load 3 state and voltage was greatly affected by the line disconnection since it is close to the fault than the others. Stored energy utilization can be seen in load 3 just after the fault and all the energy states regain the desired state value after 8s. New s.s values of the admittances were found as 0.826 p.u, 1.027 p.u, and 1.266 p.u respectively. Load bus 1, 2 and 3 voltages were changed to 0.984 V, 0.988 V and 0.974 V. From the results, it can be inferred that the proposed concept is capable of providing uninterruptible power to the active loads even under a distribution line disconnection.

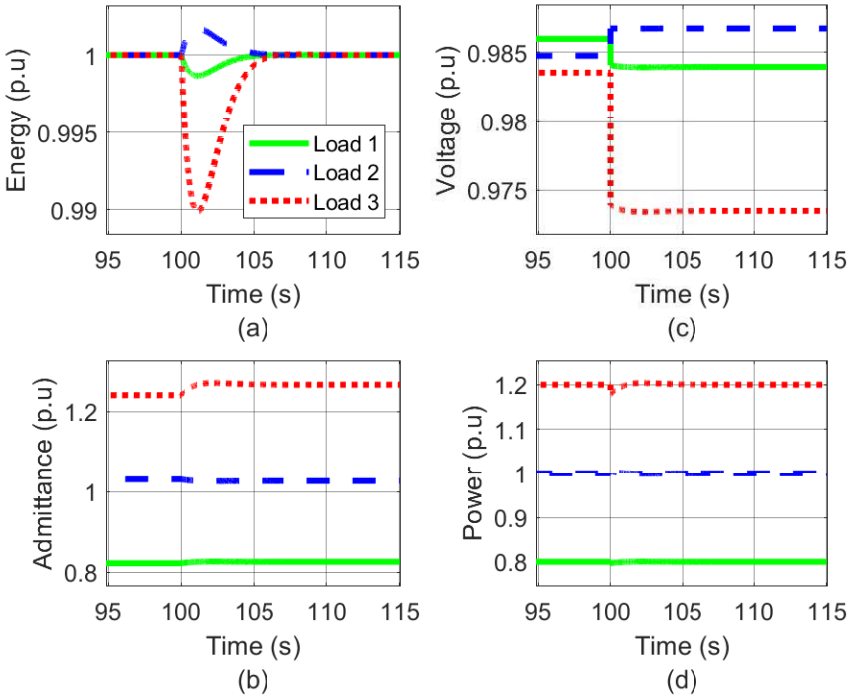

Figure 5.15: Variation of state, input voltages and powers subjected to a line disconnection (a) Stored energy, (b) Input admittance, (c) Input voltage and (d) Input power.

5.6 Optimally Controlled Islanded DCMG

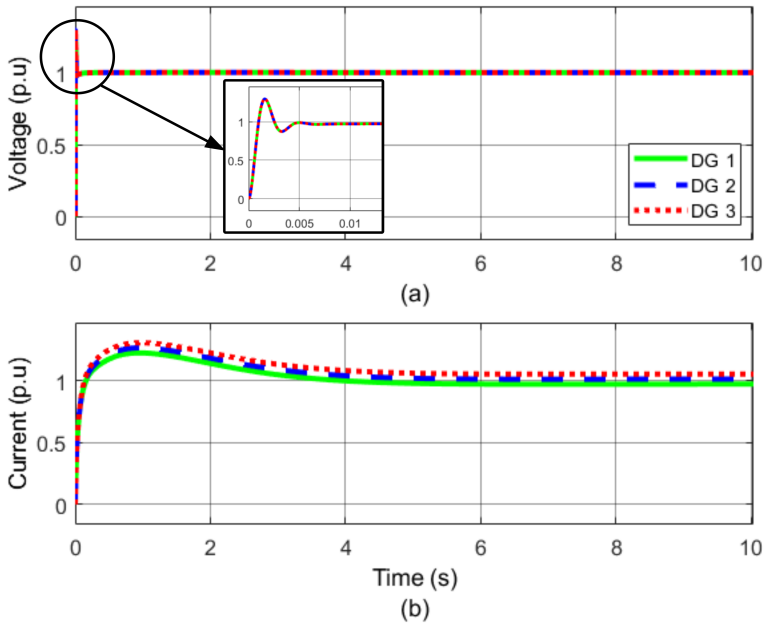

Figure 5.16: Variations in the startup (a) Output voltage, and (b) Output current.

The droop free optimal feedback control of DGs developed in chapter 4 and the decentralized optimal stabilization of active loads discussed in this chapter are combined to achieve a fully optimally controlled islanded DCMG. Simulation results of startup, and load change scenarios with IEEE 9 bus system are given in Figure 5.16 to Figure 5.19. During the startup, the DG output voltages reach the desired 1 p.u in a short time of 20ms. The maximum voltage peak during the transient can be observed as 1.3 p.u. The output currents take 6s to gain the s.s values of 0.97 p.u, 1.02 p.u, and 1.06 p.u respectively. The maximum peak current is observed in DG3 which is 1.31 p.u. Variation of active load states and input powers during the startup are shown in Figure 5.17. These variations are similar to the results shown in Figure 5.2.

Simulations results after the CPL demand change in active load 1 from 0.8 p.u to 1.5 p.u at 20s are shown in Figures 5.18 and 5.19. A slight voltage drop can be seen in all the DG output voltages and after 8s those regain the desired value. Due to the demand change DG 1, 2 and 3 output currents increase to new s.s values of 1.26 p.u, 1.31 p.u, and 1.2 p.u. As in the startup case, active load behavior is similar to the results already discussed in Figure 5.7.

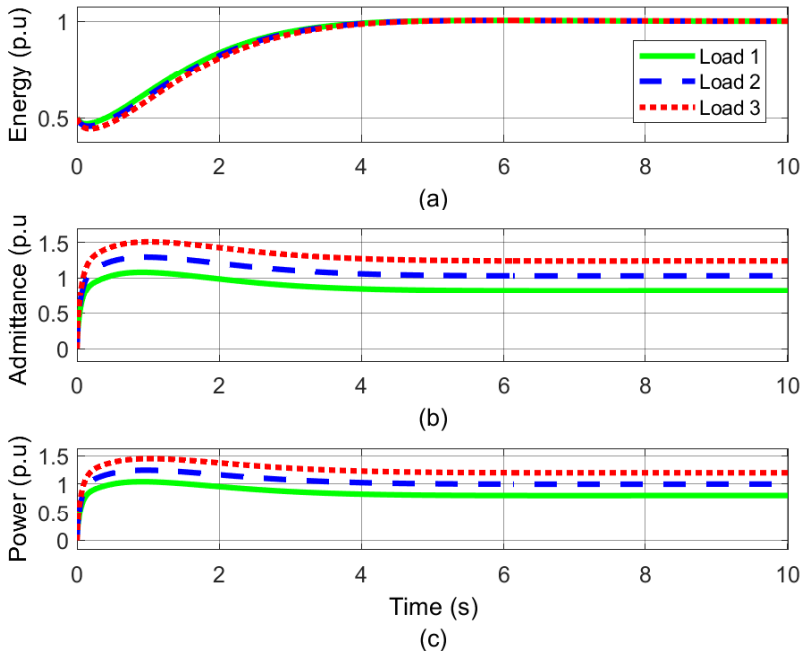

Figure 5.17: Variations in the startup (a) Stored energy, (b) Input admittance, and (c) Input power.

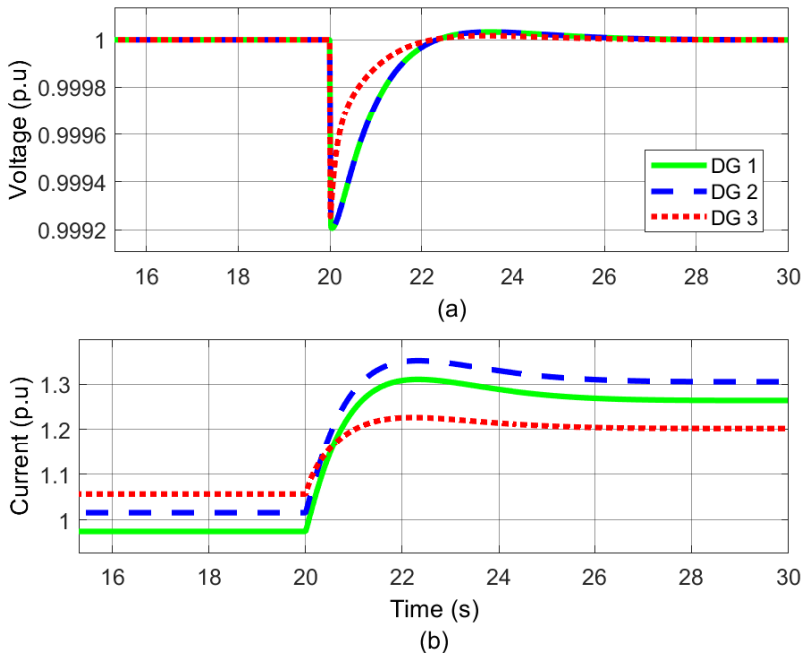

Figure 5.18: Variations in the load change (a) Output voltage, and (b) Output current.

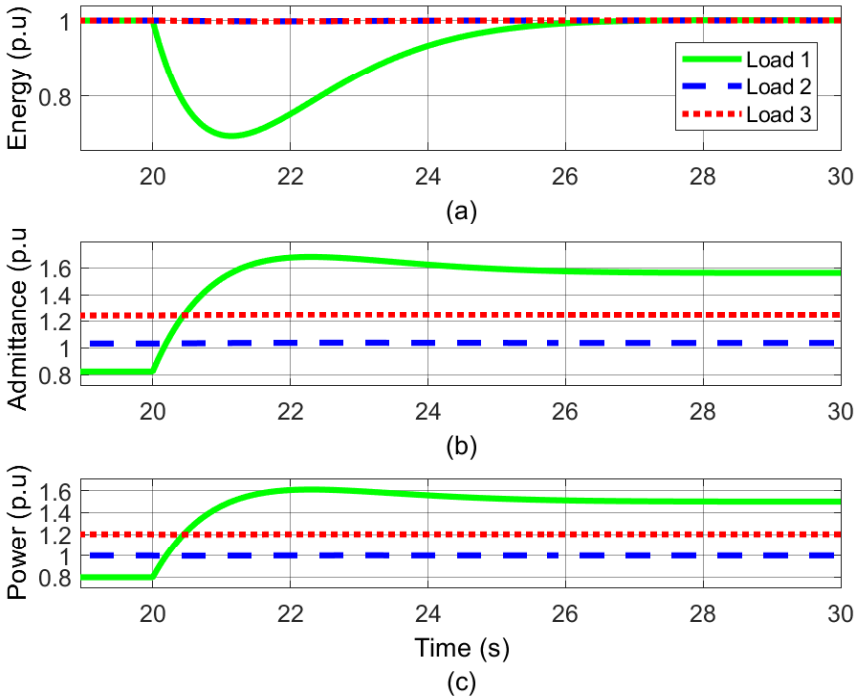

Figure 5.19: Variation of state, and input powers of active loads in the load change (a) Stored energy, (b) Input admittance, and (c) Input power.

5.7 Conclusion

A decentralized, optimal feedback stabilization controller was proposed in this chapter to optimally control active loads in DCMGs. Each active load was modeled as a control affine dynamical system with an interconnected term in the energy and admittance domain. The feedback optimal control actions were generated online via an ADP method inspired by concurrent RL. Two LIP NNs were employed to successively approximate the unknown weights in the actor and critic NNs. Lyapunov stability analysis was given to prove the UUB stability of the system states and the weight estimates. Series of Matlab/Simulink simulations were carried out and results were presented to demonstrate the effectiveness and applicability of the proposed concept. According to the results, the proposed concept shows excellent transient and s.s performances in the startup and subjected to a source, load and network disturbances.

The main limitation of the proposed approach is, this requires complete model knowledge of the dynamical system which includes parameter values of inductance, capacitance,

input voltage and output CPL demand. To overcome this limitation, a fully adaptive decentralized optimal feedback controller can be introduced. With the fully adaptive controller, the optimal active load stabilization controller can be realized with completely unknown active load demand, and PEI parameter information which opens a way to plug and play capability. Also, when there is a constant external disturbance, the proposed controller might fail to deliver the expected results. To handle such constant disturbance issues, a robust ADP approach can be introduced and would be a possible future direction of this work.

CHAPTER VI

TRANSIENT OPTIMIZATION OF ISLANDED AC MICROGRIDS

6.1 Major Objectives

Transient path optimization of inverter based distributed generators (DGs) in islanded ACMGs is proposed in this chapter. Elimination of the voltage and frequency deviations caused by the traditional droop control is the main objective of the proposed approach. Dynamical model of each DG and transmission lines are obtained in d-q rotating reference frame. Then Pontryagin's minimum principle is employed to find the optimal control and state paths which drive the system from the zero initial conditions to the predefined final manifold. The desired steady state of each DG is calculated to have proper nominal voltage and frequency of the power system. Main findings of this chapter are published in [11].

6.2 Dynamic Modeling of Distributed Generators in D-Q reference frame

In a parallel connected inverter based DG system, input side of each inverter is connected to a micro power source and the output terminal is connected to a LC filter as shown in Figure 6.1. The LC filter output is then connected to the main AC bus through a coupling inductor. The combination of input power source, inverter, LC filter and coupling inductor is considered as a DG. For the completeness of the network, a distribution line is shown from node i to node j and a series RL load (resistive and inductive) is connected to the network at node j. Once the initial condition and the steady state desired operating point of a DG are defined, there can be multiple control trajectories which can be utilized to drive the

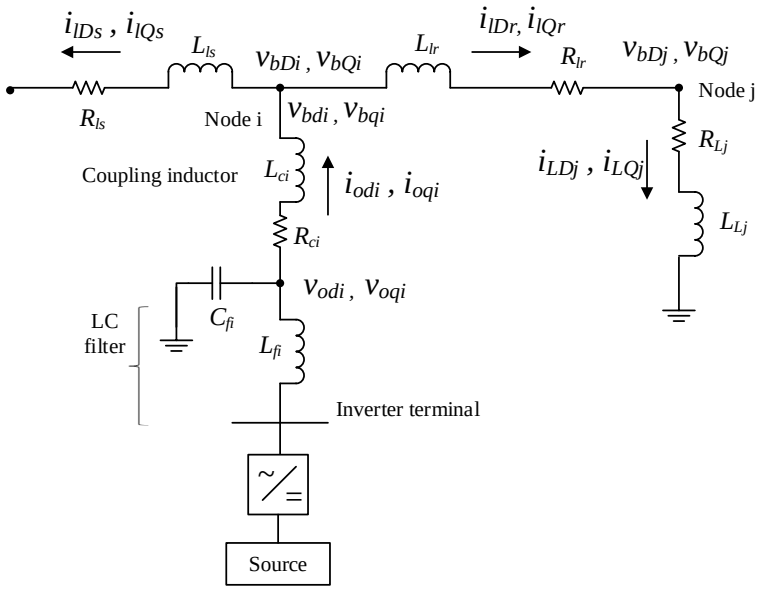

Figure 6.1: Single DG and one load connected to the main bus.

system from the given initial conditions to the preferred final manifold. Among those set of controls, finding the optimum control trajectory which minimizes a predefined performance index is important and will be discussed in this chapter. Further, the main attention will be posed to the startup transient optimization which considers the zero initial conditions. The proposed approach is an alternative to the traditional droop based ACMG control which does not cause any voltage and frequency deviations.

Suppose there are $\mathfrak{n}$ number of DGs in the set $\mathcal{N}$ which are connected to the islanded ACMG. Consider the dynamic model of the i^{th} DG shown in Figure 6.1. Rotating reference frame (d-q domain) dynamic state equations of the i^{th} DG LC filter inductor current can be expressed as,

$$L_{fi}\frac{di_{ld,i}}{dt} = -R_{fi}i_{ld,i} - v_{od,i} + v_{id,i} + L_{fi}i_{lq,i}\omega_i \tag{6.1}$$

$$L_{fi}\frac{di_{lq,i}}{dt} = -R_{fi}i_{lq,i} - v_{oq,i} + v_{iq,i} - L_{fi}i_{ld,i}\omega_i \tag{6.2}$$

where, $i_{ld,i}$, $i_{lq,i}$ are the d and q axis LC filter inductor currents, $v_{od,i}$, $v_{oq,i}$, are the d and q axis LC filter capacitor voltages, L_{fi}, R_{fi} are the filter inductance and series resistance. The inverter terminal d and q axis voltages ($v_{id,i}$, $v_{iq,i}$) and the local reference frame frequency (ω_i) are the control variables. The LC filter capacitor voltage dynamic equations can be given

as,

$$C_{fi}\frac{dv_{od,i}}{dt} = i_{ld,i} - i_{od,i} + C_{fi}v_{oq,i}\omega_i \tag{6.3}$$

$$C_{fi}\frac{dv_{oq,i}}{dt} = i_{lq,i} - i_{oq,i} - C_{fi}v_{od,i}\omega_i \tag{6.4}$$

where, C_{fi}, $i_{od,i}$, $i_{oq,i}$ are the filter capacitance, d and q axis coupling inductor currents. These coupling inductor currents are the output current components of the DG. The dynamic state equations of the coupling inductor current can be expressed as,

$$L_{ci}\frac{di_{od,i}}{dt} = -R_{ci}i_{od,i} + v_{od,i} - v_{bd,i} + L_{ci}i_{oq,i}\omega_i \tag{6.5}$$

$$L_{ci}\frac{di_{oq,i}}{dt} = -R_{ci}i_{oq,i} + v_{oq,i} - v_{bq,i} - L_{ci}i_{od,i}\omega_i \tag{6.6}$$

where, L_{ci} and R_{ci} are the inductance and the resistance of the coupling inductor. Local d and q axis nodal bus bar voltages at the i^{th} DG output are given as $v_{bd,i}$ and $v_{bq,i}$ which are measurable quantities.

The dynamic model of the i^{th} DG is given by the equations (6.1) to (6.6). Since $\mathfrak{n}$ individual DG systems are in the MG, this procedure is repeated from $i = 1$ to $\mathfrak{n}$. Local state of the i^{th} DG is $x_i = \begin{bmatrix} i_{ld,i} & i_{lq,i} & v_{od,i} & v_{oq,i} & i_{od,i} & i_{oq,i} \end{bmatrix}^T \in \mathbb{R}^6; i \in \mathcal{N}$. On the other hand, the control input of the i^{th} DG is defined as $u_i = \begin{bmatrix} \omega_i & v_{id,i} & v_{iq,i} \end{bmatrix}^T \in \mathbb{R}^3; i \in \mathcal{N}$. Concatenating (6.1)-(6.6), the dynamic model of a single DG can be represented in vector form as,

$$\dot{x}_i = f_i(x_i, u_i) \tag{6.7}$$

In order to model the network dynamics, single DG is selected as the common reference frame and all the transmission lines and loads are defined on this reference frame. DG1 frequency is taken as the common reference frame in this study ($\omega_{com} = \omega_1$). In order to well define the bus bar nodal voltages $v_{bd,i}$ and $v_{bq,i}$, a sufficiently large virtual resistor (r) is introduced. Based on this virtual resistance, and referred to the node i in the Figure 6.1, d and q axis bus bar voltages are defined as,

$$v_{bd,i} = r(i_{od,i} - i_{lD,r} - i_{lD,s}) \tag{6.8}$$

$$v_{bq,i} = r(i_{oq,i} - i_{lQ,r} - i_{lQ,s}) \tag{6.9}$$

where, $i_{lD,r}$, $i_{lQ,r}$, $i_{lD,s}$, $i_{lQ,s}$ are the d and q axis line currents defined on the common reference frame. Consider the distribution line segment between node i and j shown in Figure 6.1. Dynamic equations of the d and q axis line currents between these two nodes are derived as,

$$L_{lr}\frac{di_{lD,r}}{dt} = v_{bD,i} - v_{bD,j} - R_{lr}i_{lD,r} + L_{lr}i_{lQ,r}\omega_{com} \tag{6.10}$$

$$L_{lr}\frac{di_{lQ,r}}{dt} = v_{bQ,i} - v_{bQ,j} - R_{lr}i_{lQ,r} - L_{lr}i_{lD,r}\omega_{com} \tag{6.11}$$

where, series inductance and resistance of the line segment are given by L_{lr} and R_{lr}.

In this study, RL loads are considered to demonstrate the proposed concept which could replace with any other type of load models. The state equations of the d and q axis load currents ($i_{LD,j}$ and $i_{LQ,j}$) through the series RL load connected to the node j in the Figure 6.1 are,

$$L_{Lj}\frac{di_{LD,j}}{dt} = v_{bD,j} - R_{Lj}i_{LD,j} + L_{Lj}i_{LQ,j}\omega_{com} \tag{6.12}$$

$$L_{Lj}\frac{di_{LQ,j}}{dt} = v_{bQ,j} - R_{Lj}i_{LQ,j} - L_{Lj}i_{LD,j}\omega_{com} \tag{6.13}$$

where the inductance and the resistance of the RL load connected to the node j are given as L_{Lj} and R_{Lj} respectively. In case of a motor load such as an induction motor, the corresponding RL equivalent model in d-q reference frame can be utilized [166]. This completes the dynamic modeling of the ACMG. Next section introduces the optimal control approach to transient path optimization of the ACMG.

6.3 Proposed Local Optimal Control Approach for AC Microgrids

The objective is to derive optimal control trajectories for each local DG to drive the system from a given initial condition to a desired final manifold. Further, it aims to mitigate the voltage and frequency deviations caused by the traditional droop control mechanism. Consider the state vector of a single DG as $x_i : [t_0, t_f] \rightarrow \mathbb{R}^6$ with the initial condition $x_i(t_0)$, where the initial and final times are t_0 and t_f respectively. Then, finding the admissible control $u_i : [t_0, t_f] \rightarrow \Omega_i \subseteq \mathbb{R}^3$ such that the cost functional given in (6.14) is minimized while satisfying the dynamical constraints (6.7) can be defined as the optimal

control problem [128, 167].

$$J_i(u_i) = \theta_i(x_i(t_f)) + \int_{t_0}^{t_f} \Upsilon_i(x_i, u_i, t)dt \tag{6.14}$$

In (6.14) the fixed cost or the Mayer cost is denoted as $\theta_i(x_i(t_f))$ which is a function of states at the final time [168]. The variable or the transient cost from the initial time t_0 to the final time t_f is given by $\Upsilon(x_i, u_i)$. Since this work mainly focuses on transient optimization, Mayer cost is considered to be zero. Moreover, it is assumed that the initial time and the initial state are specified and the fixed time problem will be considered.

The desired control and state of i^{th} DG is defined as, $\bar{u}_i = \begin{bmatrix} \bar{\omega}_i & \bar{v}_{id,i} & \bar{v}_{iq,i} \end{bmatrix}^T$ and $\bar{x}_i = \begin{bmatrix} \bar{i}_{ld,i} & \bar{i}_{lq,i} & \bar{v}_{od,i} & \bar{v}_{oq,i} & \bar{i}_{od,i} & \bar{i}_{oq,i} \end{bmatrix}^T$. These desired values are computed to ensure the d axis LC filter output voltage equals to the nominal system voltage ($\bar{v}_{od,i} = v_n$), q axis voltage equals to zeros ($\bar{v}_{oq,i} = 0$) and frequency equals to the nominal system frequency ($\bar{\omega}_i = \omega_n$). This makes the output voltage aligned with the d axis and output active and reactive powers become proportional to output d and q axis currents respectively [29]. Steady state desired values of the local DG systems can be found using any numerical method or a power flow solution method developed for MGs [169, 170]. A quadratic transient cost function is constructed as,

$$\Upsilon_i(x_i, u_i, t) = (x_i - \bar{x}_i)^T Q_i (x_i - \bar{x}_i) + (u_i - \bar{u}_i)^T R_i (u_i - \bar{u}_i) \tag{6.15}$$

where, Q_i and R_i are positive definite weight matrices with appropriate dimensions. Now each DG has its local state dynamics and cost functions defined as (6.7), (6.14) and (6.15). Next, these systems need to be solved to obtain the optimal control trajectories which is discussed in the next section.

6.4 Solution of the Local Optimal Control Problem

Solution of the proposed optimal control problem is found using the Pontryagin's minimum principle [128, 167]. The the Pontryagin's minimum principle provides a two point boundary value problem (BVP) [128, 167] and using the solution of BVP, optimal control signals can be extracted. The Pontryagin's minimum principle gives only the necessary

conditions for the optimality and the hence the control signals are open loop [128, 167].
Definition 1 [128, 167]: Hamiltonian function, $\mathcal{H}_i : \mathbb{R}^n \times \Omega_i \times \mathbb{R}^n \times [t_0, t_f] \rightarrow \mathbb{R}$,

$$\mathcal{H}_i(x_i, u_i, \lambda_i, t) = \Upsilon_i(x_i, u_i, t) + \lambda_i^T f_i(x_i, u_i) \tag{6.16}$$

where, $\lambda_i : [t_0, t_f] \rightarrow \mathbb{R}^n$ is the costate vector [128, 167]. In this modeling, dimension of the state vector $n = 6$ and the admissible control space $\Omega_i \in \mathbb{R}^3$.
Theorem 1 [128, 167]: If the control $u_i^* : [t_0, t_f] \rightarrow \Omega_i$ is optimal, then the following conditions hold $\forall t \in [t_0, t_f]$.

$$\dot{x}_i^* = \nabla_{\lambda_i} \mathcal{H}_i^* = f_i(x_i^*, u_i^*) \tag{6.17}$$

$$x_i^*(t_0) = x_i(t_0) \tag{6.18}$$

$$\dot{\lambda}_i^* = -\nabla_{x_i} \mathcal{H}_i^* \tag{6.19}$$

the Hamiltonian has a global minimum with respect to u_i at $u_i = u_i^*$ i.e.,

$$\mathcal{H}_i(x_i^*, u_i^*, \lambda_i^*, t) \leq \mathcal{H}_i(x_i^*, u_i, \lambda_i^*, t) \;\; ; \forall u_i \in \Omega_i \tag{6.20}$$

In a free time problem, the Hamiltonian is zero along the optimal trajectory as in (6.21) while in a fixed time problem Hamiltonian is a constant.

$$\mathcal{H}_i(x_i^*, u_i^*, \lambda_i^*, t) = 0 \tag{6.21}$$

If the final state is specified ($x_i(t_f)$), then the boundary condition at the final time is given by,

$$x_i^*(t_f) = x_i(t_f) \tag{6.22}$$

If the final state is free, then the following holds,

$$\nabla_{x_i} \theta_i(x_i^*(t_f)) - \lambda_i^*(t_f) = 0 \tag{6.23}$$

In the above relationships, ∇ is the gradient operator and the superscript (*) denotes the optimal condition. The proof of this Theorem can be found in [128] and [167]. The optimal

controller u_i^* can be explicitly obtained by evaluating,

$$\nabla_{u_i} \mathcal{H}_i = 0 \tag{6.24}$$

Further, Mayer cost is considered to be zero, and hence (6.23) simplifies to $\lambda_i^*(t_f) = 0$. Evaluation of (6.17) for the i^{th} DG results in (6.7) with optimal state and control signals. The costate dynamic equations of the i^{th} DG given by (6.19) are,

$$\dot{\lambda}_{1,i}^* = \frac{\lambda_{1,i}^* r_f}{L_{fi}} - \frac{\lambda_{3,i}^*}{C_{fi}} - 2k_{ld}(i_{ld,i}^* - \bar{i}_{ld,i}) + \lambda_{2,i}^* w_i^* \tag{6.25}$$

$$\dot{\lambda}_{2,i}^* = \frac{\lambda_{2,i}^* r_f}{L_{fi}} - \frac{\lambda_{4,i}^*}{C_{fi}} - 2k_{lq}(i_{lq,i}^* - \bar{i}_{lq,i}) - \lambda_{1,i}^* w_i^* \tag{6.26}$$

$$\dot{\lambda}_{3,i}^* = \frac{\lambda_{1,i}^*}{L_{fi}} - \frac{\lambda_{5,i}^*}{L_{ci}} - 2k_{vd}(v_{od,i} - \bar{v}_{od,i}) + \lambda_{4,i}^* w_i^* \tag{6.27}$$

$$\dot{\lambda}_{4,i}^* = \frac{\lambda_{2,i}^*}{L_{fi}} - \frac{\lambda_{6,i}^*}{L_{ci}} - 2k_{vq} v_{oq,i} - \lambda_{3,i}^* w_i^* \tag{6.28}$$

$$\dot{\lambda}_{5,i}^* = \frac{\lambda_{5,i}^*(r + r_c)}{L_{ci}} + \frac{\lambda_{3,i}^*}{C_{fi}} - 2k_{od}(i_{od,i}^* - \bar{i}_{od,i}) + \lambda_{6,i}^* w_i^* \tag{6.29}$$

$$\dot{\lambda}_{6,i}^* = \frac{\lambda_{6,i}^*(r + r_c)}{L_{ci}} + \frac{\lambda_{4,i}^*}{C_{fi}} - 2k_{oq}(i_{oq,i}^* - \bar{i}_{oq,i}) - \lambda_{5,i}^* w_i^* \tag{6.30}$$

where, k_{ld}, k_{lq}, k_{vd}, k_{vq}, k_{od}, k_{oq} are the state weight gains in the matrix Q_i. The optimal control is given by,

$$u_i^* = \begin{bmatrix} \dfrac{(\lambda_{2,i}^* i_{ld,i}^* - \lambda_{1,i}^* i_{lq,i}^* + \lambda_{6,i}^* i_{od,i}^* - \lambda_{5,i}^* i_{oq,i}^* + \lambda_{4,i}^* v_{od,i}^* - \lambda_{3,i}^* v_{oq,i}^* + 2k_\omega \omega_n)}{2k_\omega} \\ \dfrac{-(\lambda_{1,i}^* - 2L_{fi} k_{vid} \bar{v}_{id,i})}{2L_{fi} k_{vid}} \\ \dfrac{-(\lambda_{2,i}^* - 2L_{fi} k_{viq} \bar{v}_{iq,i})}{2L_{fi} k_{viq}} \end{bmatrix} \tag{6.31}$$

where, k_ω, k_{vid} and k_{viq} are the control weights. Relations from (6.7), (6.21), (6.25) to (6.31) generates a two point BVP set with the boundary conditions given by (6.18) and (6.22) or (6.23). The overall process is summarized in Figure 6.2. The optimum trajectories are the solution of the generated BVP equation set along with the network and load dynamics. Due

to the high nonlinearities associated with the equations, obtaining a closed form analytical solution is not feasible. Hence, corresponding numerical solution is obtained using the "bvp4c" two point BVP solver in Matlab [171]. The optimum trajectory calculation is an offline process which generates family of optimum trajectories under different system contingencies. Generated optimum trajectories can be used as references to maneuver each DG system along the optimum path.

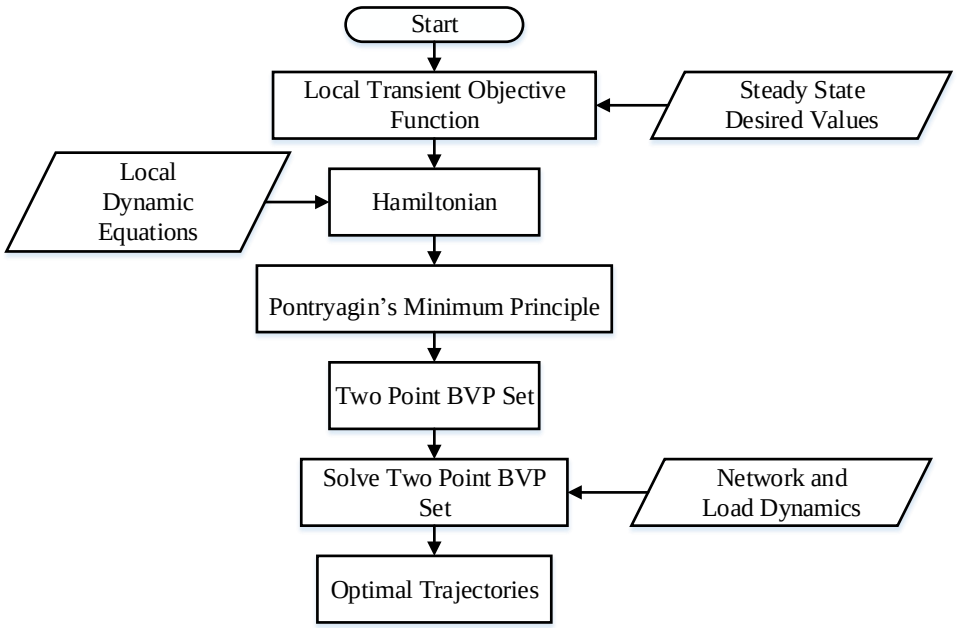

Figure 6.2: Flowchart of the optimal trajectory generation process.

From the generated optimum trajectories, optimal control trajectories can be extracted and stored for the control purpose. The generated d and q axis inverter terminal voltage references ($v^*_{id,i}$ and $v^*_{iq,i}$) are transformed to three phase abc domain voltages utilizing the optimal frequency trajectory (ω^*_i) and the dq0 to abc transformation [164]. These abc domain signals can be used as the modulation signals in the pulse width modulator (PWM) to generate the optimal switching actions to the inverter [172].

6.5 Simulation Results

Example test cases were simulated in Matlab using the bvp4c function. Considered inverter based DG test system is illustrated in Figure 6.3. LC filter parameters of all the

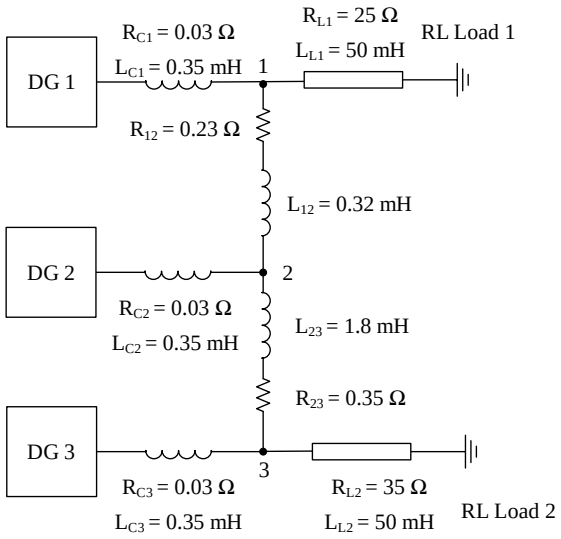

Figure 6.3: Example test system.

DGs were considered same and are given in Table 6.1. DG 1 reference frame was selected as the common reference frame and virtual resistor (r) was selected as 1000 Ω. Nominal rms voltage and the system frequency were considered as 110 V per phase and 60 Hz respectively. Steady state desired operating points given in Table 6.2 were considered when constructing the local objective functions for the startup transient trajectory optimization. State and control weight matrices were considered as identity matrices with appropriate dimensions. The fixed final time problem for $t_f = 0.1$ s was solved with free final state.

Table 6.1: LC Filter Parameters

Parameter	Value
L_{fi}	1.35 mH
r_{fi}	0.1 Ω
C_{fi}	50 μF

Optimal variation of DG frequencies are depicted in Figure 6.4. Based on the results, it can be seen that all the DGs show a similar variation. The maximum and minimum frequencies during the transient are observed as 377.5185 rad/s in DG2 and 375.8494 rad/s in DG1 respectively. All the DGs gain their desired steady state value of 377 rad/s in 0.02 s. Figure 6.5 shows the optimal variations of d and q axis inverter terminal voltages. DG2

Table 6.2: Desired Operating Points

	$\bar{i}_{ld,i}$	$\bar{i}_{lq,i}$	$\bar{v}_{od,i}$	$\bar{v}_{oq,i}$	$\bar{i}_{od,i}$	$\bar{i}_{oq,i}$	$\bar{\omega}_i$	$\bar{v}_{id,i}$	$\bar{v}_{iq,i}$
DG1	3.4875	0.3084	190.5256	0	3.4875	-3.2829	376.9911	190.7174	1.8058
DG2	2.1221	3.0308	190.5256	0	2.1221	-0.5606	376.9911	189.1953	1.3831
DG3	4.0044	1.4932	190.5256	0	4.0044	-2.0981	376.9911	190.1661	2.1873

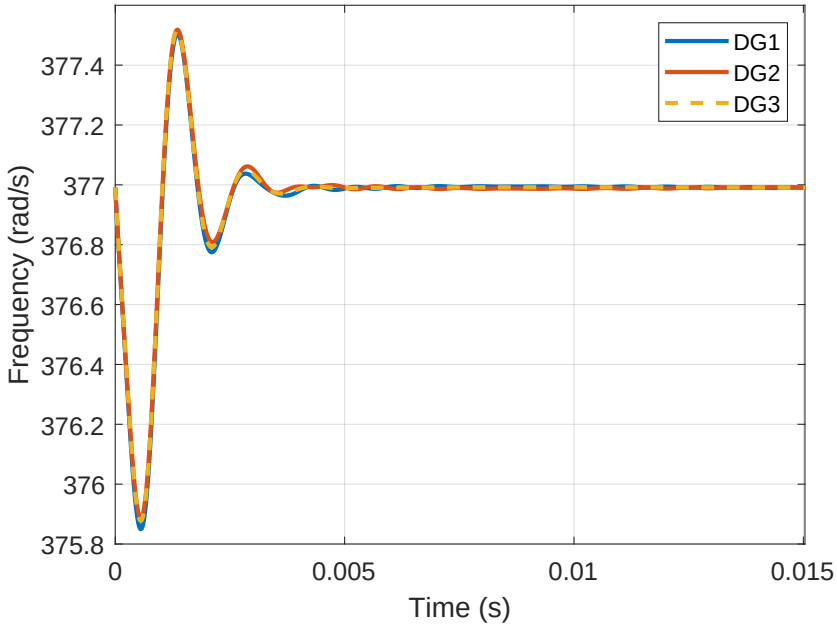

Figure 6.4: Optimal Frequency Variation (ω^*).

d axis voltage shows the minimum voltage of 93.2330 V during the transient while DG1 shows the maximum d axis voltage of 268.1362 V. Maximum and minimum q axis voltages during the transient are observed as 18.2785 V in DG3 and -9.4907 V in DG2. Corresponding voltage profiles in the abc domain are shown in Figure 6.6. These voltages can be used as the modulating signals in the PWM generator.

The optimal d and q axis LC filter output voltage variations are shown in Figure 6.7. All the DGs show similar variation as seen by the results. Maximum d axis transient voltage is observed in DG 2 which is 238.5204 V. Maximum q axis voltage during the transient is observed as 7.5376 V in DG3 and the minimum of -13.2829 V is observed in DG2. Both d and q axis output voltages reach desired values in 0.02 s.

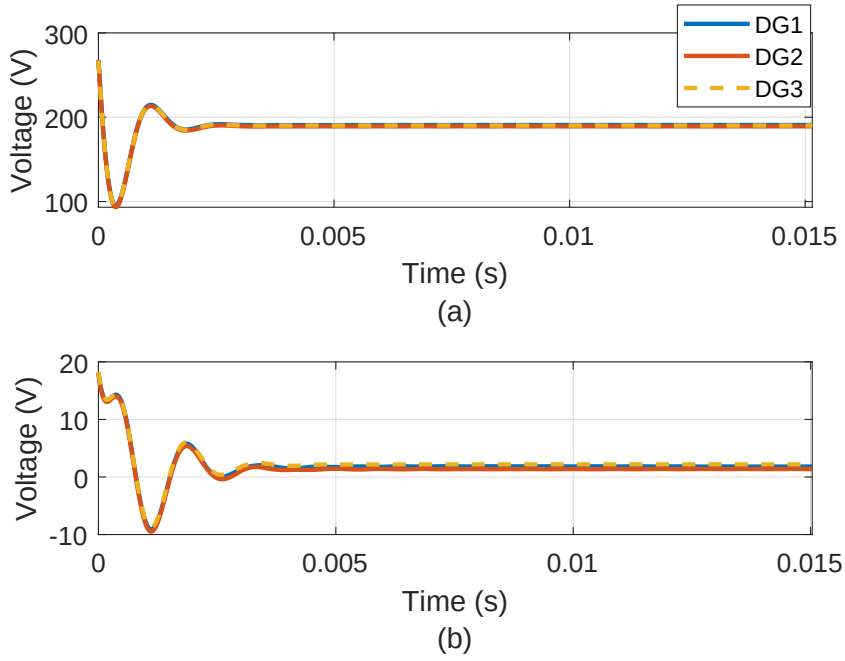

Figure 6.5: Optimal Inverter Terminal Voltage Variation. (a) v_{id}^* and (b) v_{iq}^*

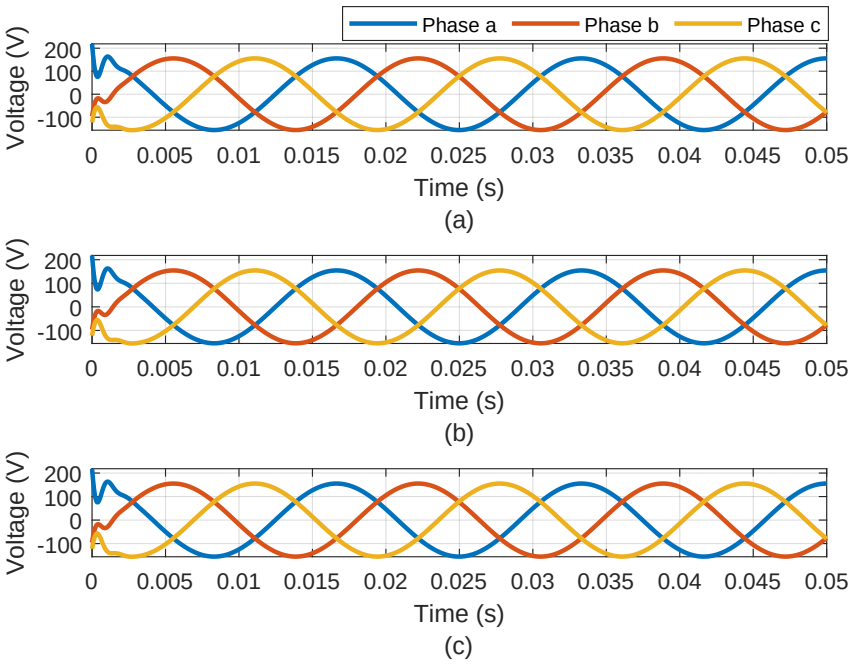

Figure 6.6: Optimal Inverter Terminal Voltages in abc Domain. (a) DG1, (b) DG2 and (b) DG3

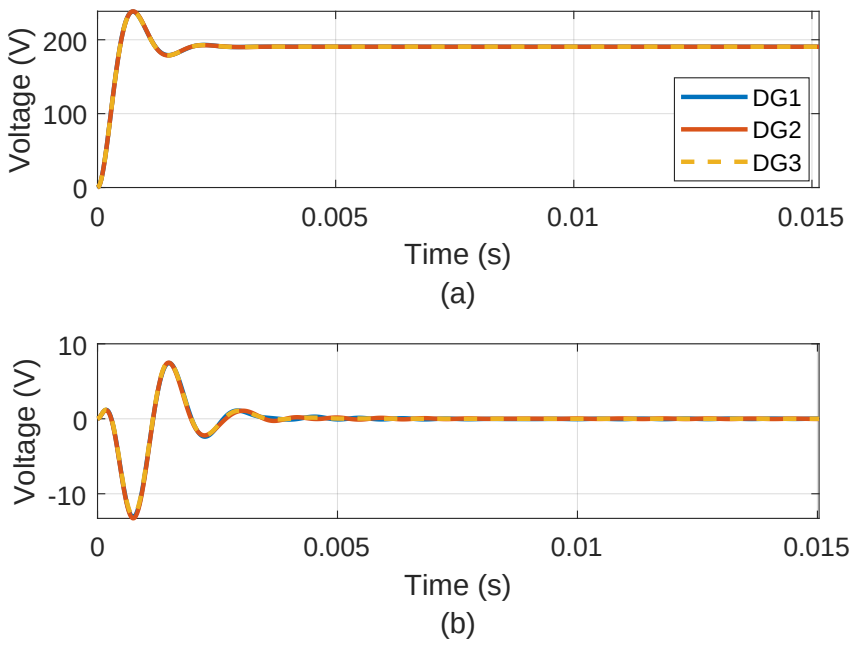

Figure 6.7: Optimal LC Filter Output Voltage Variation. (a) v_{od}^* and (b) v_{oq}^*

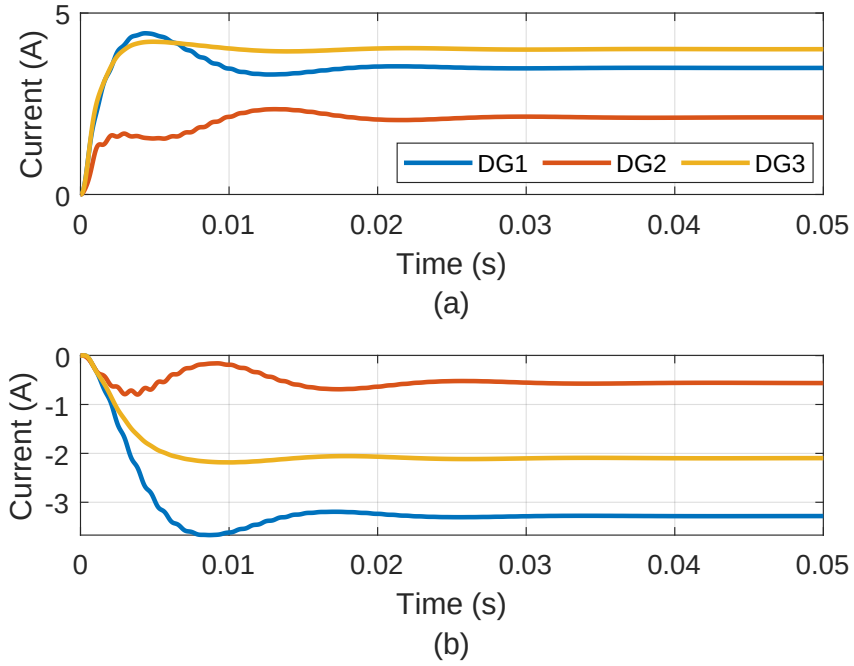

Figure 6.8: Optimal DG Output Current Variation. (a) i_{od}^* and (b) i_{oq}^*

Figure 6.8 depicts the optimal variations of d and q axis output currents. Maximum d axis and minimum q axis currents are observed in DG1 which are 4.4424 A and -3.6715 A. According to the results, two axis currents reach desired values within 0.04 s.

The variations in optimal output active and reactive powers are shown in Figure 6.9. The DG1 depicts both maximum active and reactive powers during the transient which are 846.4406 W and 699.2405 var. Steady state active powers of DG1, DG2 and DG3 are 664.4 W, 404.5 W and 762.8 W. The reactive power productions of DG1, DG2 and DG3 are 625.4 var, 107 var and 399.6 var.

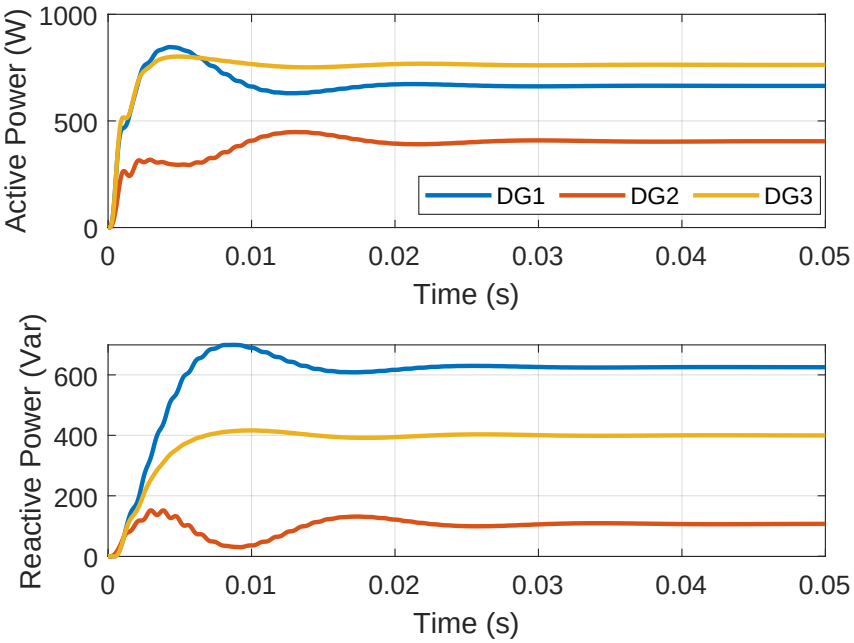

Figure 6.9: Optimal DG Output Power Variation. (a) Active Power and (b) Reactive Power

6.6 Conclusion

In this chapter, an optimal control frame work was proposed to obtain the optimal transient response of parallel connected inverter based DGs in an islanded MG. Main objective of the proposed approach is to replace the traditional droop control in ACMG in order to mitigating the voltage and frequency deviations. Parallel connected DGs were defined as local subsystems in the islanded MG system. The dynamic model of the system and the individual DG objective functions were modeled in the d-q reference frame. The Pontryagin's minimum

principle was employed to obtain the optimal transient trajectories. Simulations were carried out to investigate the performance of the proposed concept. Startup optimal transient trajectory generation was presented with fixed final time and free final state. Implementation of the proposed algorithm requires all the system parameters. In case of a parameter change, the model need to be recomputed and new BVP set has to be obtained accordingly. Typically, adaptive controllers are employed for the systems with uncertain parameters. Development of an adaptive controller would be a possible future direction of this work.

CHAPTER VII

CONCLUSION

In order to enhance the performances of the traditional droop control in MG, to mitigate the major drawbacks of the droop control, and to enhance the active load operations in MG domain, advance control and optimization methodologies have been proposed in this dissertation. First, a NSGA II MOO based optimal droop coefficient computation methodology was proposed to improve the traditional droop relationship. In this approach, Pareto optimal front of the constructed MOO problem was obtained and a fuzzy membership function approach was introduced to select a best compromise solution which is set of optimal virtual resistances and reference voltage set points for the DGs in the MG. Further, a state feedback linearized controller was proposed to replace the PI control loops in traditional droop control to facilitate the control actions with the derived optimal droop relationships. Both simulation and experimental results were given to validate the proposed concept. According to the results it can be inferred that the proposed optimal droop relationships have better performance than the traditional droop. Inclusion of a dynamic MOO technique to make the droop coefficient calculation process online would be exciting future directions of this work.

Secondly, in order to mitigate the voltage degradation cased by the traditional droop control, and to eliminate the issues with the PI control, a droop free approximate optima feedback strategy was proposed for islanded MGs. This methodology replaces the conventional droop control and PI control loops in MG and hence it eliminates the issues related to the PI based droop control. A concurrent RL method has been employed to generate the solution to the constrained input infinite horizon optimal control problem online. In the modeling the

optimal value function and the optimal control law of each DG were approximated by two separate LIP NNs. With these optimal control actions, DGs operations can be improved and the simulation and experimental validations were presented to demonstrate the applicability of the proposed concept. The results demonstrate excellent performances in both transient and steady-state. Development of an advanced adaptive learning algorithm that does not require exact knowledge of internal parameters or exact model of the system would be the main future direction of this study.

Next, a decentralized feedback optimal control methodology was proposed to control active loads in islanded DCMGs. The variable admittance representation of DC-DC converter was employed to model the constant power load and the PEI attached to it. The desired input admittance and internal energy storage of each load is computed and a decentralized optimal feedback controller is proposed to regulate the input admittance to the desired value online. A concurrent RL based approximate dynamic programming approach with constrained input has been employed to solve the infinite horizon optimal regulation problem. As in the optimal feedback control of DGs, two LIP NNs were used to approximate the optimal value function and the control input. Several simulations were carried out to demonstrate the performance of the proposed concept and results show better responses compared to the existing methods. Improvement of the developed method to achieve plug and play capability with completely unknown active load demand, and PEI parameter information would be an interesting future direction of this work.

Finally, to eliminate the voltage and frequency deviations caused by the droop control, a transient path optimization methodology for inverter-based DGs operate in islanded ACMGs was presented. The dynamic model of the system and the individual DG objective functions were modeled in the d-q reference frame. The Pontryagin's minimum principle was employed to obtain the optimal transient trajectories. Simulations were carried out and results were given to demonstrate the performance of the proposed concept. Development of an adaptive feedback controller would be a possible future direction of this work.

The proposed concepts are introduced to improve the control operations of MGs by introducing advance control architectures, enhancing the traditional droop and introducing alternatives to the droop control. The simulation and experimental results demonstrate the expected outcomes and superior performances compared to the existing methods.

REFERENCES

[1] Baoquan Liu, Fang Zhuo, Yixin Zhu, and Hao Yi. System operation and energy management of a renewable energy-based dc micro-grid for high penetration depth application. *IEEE Trans. Smart Grid.*, 6(3):1147–1155, 2015.

[2] Seyed Mahdi Ashabani and Yasser Abdel-rady I Mohamed. New family of microgrid control and management strategies in smart distribution grids—analysis, comparison and testing. *IEEE Trans. Power Syst.*, 29(5):2257–2269, 2014.

[3] Nishantha C Ekneligoda and Wayne W Weaver. Game-theoretic cold-start transient optimization in dc microgrids. *IEEE Trans. Ind. Electron.*, 61(12):6681–6690, 2014.

[4] Wayne W Weaver and Philip T Krein. Game-theoretic control of small-scale power systems. *IEEE Trans. Power Del.*, 24(3):1560–1567, 2009.

[5] Nishantha C Ekneligoda and Wayne W Weaver. A game theoretic bus selection method for loads in multibus dc power systems. *IEEE Trans. Ind. Electron.*, 61(4):1669–1678, 2014.

[6] Nikos Hatziargyriou, Hiroshi Asano, Reza Iravani, and Chris Marnay. Microgrids. *IEEE Power Energy Mag.*, 5(4):78–94, 2007.

[7] Xiongfei Wang, Josep M Guerrero, and Zhe Chen. Control of grid interactive ac microgrids. In *2010 IEEE International Symposium on Industrial Electronics*, pages 2211–2216. IEEE, 2010.

[8] J. M. Guerrero, M. Chandorkar, T. Lee, and P. C. Loh. Advanced control architectures for intelligent microgrids part i: Decentralized and hierarchical control. *IEEE Trans. Ind. Electron.*, 60(4):1254–1262, April 2013.

[9] Josep M Guerrero, Mukul Chandorkar, Tzung-Lin Lee, and Poh Chiang Loh. Advanced control architectures for intelligent microgrids—part i: Decentralized and hierarchical control. *IEEE Trans. Ind. Electron.*, 60(4):1254–1262, 2013.

[10] Shaghayegh Kazemlou and Shahab Mehraeen. Novel decentralized control of power systems with penetration of renewable energy sources in small-scale power systems. *IEEE Trans. Energy Convers.*, 29(4):851–861, 2014.

[11] A. M. Dissanayake and N. C. Ekneligoda. Transient optimization of parallel connected inverters in islanded ac microgrids. *IEEE Trans. Smart Grid.*, 10(5):4951–4961, 2018.

[12] Ayman B Eltantawy and MMA Salama. Management scheme for increasing the connectivity of small-scale renewable dg. *IEEE Trans. Sustain. Energy*, 5(4):1108–1115, 2014.

[13] Magdi S Mahmoud and M Fouad. *Control and optimization of distributed generation systems*, volume 19. Springer, 2015.

[14] Magdi S Mahmoud. *Microgrid: advanced control methods and renewable energy system integration*. Elsevier, 2016.

[15] Huang Jiayi, Jiang Chuanwen, and Xu Rong. A review on distributed energy resources and microgrid. *Renewable and Sustainable Energy Reviews*, 12(9):2472–2483, 2008.

[16] Robert H Lasseter. Microgrids and distributed generation. *Journal of Energy Engineering*, 133(3):144–149, 2007.

[17] Robert H Lasseter. Microgrids. In *2002 IEEE Power Engineering Society Winter Meeting. Conference Proceedings (Cat. No. 02CH37309)*, volume 1, pages 305–308. IEEE, 2002.

[18] Dan T Ton and Merrill A Smith. The us department of energy's microgrid initiative. *The Electricity Journal*, 25(8):84–94, 2012.

[19] Daniel E Olivares, Ali Mehrizi-Sani, Amir H Etemadi, Claudio A Cañizares, Reza Iravani, Mehrdad Kazerani, Amir H Hajimiragha, Oriol Gomis-Bellmunt, Maryam

Saeedifard, Rodrigo Palma-Behnke, et al. Trends in microgrid control. *IEEE Trans. Smart Grid.*, 5(4):1905–1919, 2014.

[20] David Moskovitz, Cheryl Harrington, and John W Rowe. *Profits and progress through distributed resources*. Regulatory Assistance Project, 2000.

[21] Adam Hirsch, Yael Parag, and Josep Guerrero. Microgrids: A review of technologies, key drivers, and outstanding issues. *Renewable and Sustainable Energy Reviews*, 90:402–411, 2018.

[22] Paolo Tenti, Alessandro Costabeber, Paolo Mattavelli, and Daniela Trombetti. Distribution loss minimization by token ring control of power electronic interfaces in residential microgrids. *IEEE Trans. Ind. Electron.*, 59(10):3817–3826, 2012.

[23] Sijo Augustine, Mahesh K Mishra, and N Lakshminarasamma. Adaptive droop control strategy for load sharing and circulating current minimization in low-voltage standalone dc microgrid. *IEEE Trans. Sustain. Energy*, 6(1):132–141, 2015.

[24] Nikos Hatziargyriou. *Microgrids: architectures and control*. John Wiley & Sons, 2014.

[25] Josep M Guerrero, Juan C Vasquez, José Matas, Luis García De Vicuña, and Miguel Castilla. Hierarchical control of droop-controlled ac and dc microgrids—a general approach toward standardization. *IEEE Trans. Ind. Electron.*, 58(1):158–172, 2011.

[26] Faik Tekin Asal and Mert COŞGUN. Pi, pd, pid controllers. *Middle East Technical University Electrical & Electronics Engineering*.

[27] T. Sreekumar and K. S. Jiji. Comparison of proportional-integral (p-i) and integral-proportional (i-p) controllers for speed control in vector controlled induction motor drive. In *2012 2nd International Conference on Power, Control and Embedded Systems*, pages 1–6, Dec 2012.

[28] Avisha Tah and Debapriya Das. An enhanced droop control method for accurate load sharing and voltage improvement of isolated and interconnected dc microgrids. *IEEE Trans. Sustain. Energy*, 7(3):1194–1204, 2016.

[29] Nagaraju Pogaku, Milan Prodanovic, and Timothy C Green. Modeling, analysis and testing of autonomous operation of an inverter-based microgrid. *IEEE Transactions on power electronics*, 22(2):613–625, 2007.

[30] A. Maulik and D. Das. Optimal operation of droop-controlled islanded microgrids. *IEEE Trans. Sustain. Energy*, 9(3):1337–1348, July 2018.

[31] Ruben Barros Godoy, Joao OP Pinto, Carlos Alberto Canesin, Ernane Antonio Alves Coelho, and Alexandra MAC Pinto. Differential-evolution-based optimization of the dynamic response for parallel operation of inverters with no controller interconnection. *IEEE Trans. Ind. Electron.*, 59(7):2859–2866, 2012.

[32] Kai Yu, Qian Ai, Shiyi Wang, Jianmo Ni, and Tianguang Lv. Analysis and optimization of droop controller for microgrid system based on small-signal dynamic model. *IEEE Trans. Smart Grid.*, 7(2):695–705, 2016.

[33] MA Hassan and MA Abido. Optimal design of microgrids in autonomous and grid-connected modes using particle swarm optimization. *IEEE Trans. Power Electron.*, 26(3):755–769, 2011.

[34] Il-Yop Chung, Wenxin Liu, David A Cartes, Emmanuel G Collins, and Seung-Il Moon. Control methods of inverter-interfaced distributed generators in a microgrid system. *IEEE Trans. Ind. Appl.*, 46(3):1078–1088, 2010.

[35] Fatih Cingoz, Ali Elrayyah, and Yilmaz Sozer. Optimized settings of droop parameters using stochastic load modeling for effective dc microgrids operation. *IEEE Trans. Ind. Appl.*, 53(2):1358–1371, 2017.

[36] Ali Elrayyah, Fatih Cingoz, and Yilmaz Sozer. Construction of nonlinear droop relations to optimize islanded microgrid operation. *IEEE Trans. Ind. Appl.*, 51(4):3404–3413, 2015.

[37] Lexuan Meng, Tomislav Dragicevic, Juan C Vasquez, and Josep M Guerrero. Tertiary and secondary control levels for efficiency optimization and system damping in droop controlled dc–dc converters. *IEEE Trans. Smart Grid.*, 6(6):2615–2626, 2015.

[38] Salman A Khan and Shafiqur Rehman. Iterative non-deterministic algorithms in on-shore wind farm design: A brief survey. *Renewable and Sustainable Energy Reviews*, 19:370–384, 2013.

[39] Kalyanmoy Deb. *Multi-objective optimization using evolutionary algorithms*, volume 16. John Wiley & Sons, 2001.

[40] Xiaonan Lu, Josep M Guerrero, Kai Sun, and Juan C Vasquez. An improved droop control method for dc microgrids based on low bandwidth communication with dc bus voltage restoration and enhanced current sharing accuracy. *IEEE Trans. Power Electron.*, 29(4):1800–1812, 2013.

[41] Vahidreza Nasirian, Seyedali Moayedi, Ali Davoudi, and Frank L Lewis. Distributed cooperative control of dc microgrids. *IEEE Trans. Power Electron.*, 30(4):2288–2303, 2014.

[42] Tuyen V Vu, Dallas Perkins, Fernand Diaz, David Gonsoulin, Chris S Edrington, and Touria El-Mezyani. Robust adaptive droop control for dc microgrids. *Electric Power Systems Research*, 146:95–106, 2017.

[43] Panbao Wang, Xiaonan Lu, Xu Yang, Wei Wang, and Dianguo Xu. An improved distributed secondary control method for dc microgrids with enhanced dynamic current sharing performance. *IEEE Trans. Power Electron.*, 31(9):6658–6673, 2015.

[44] A. Maknouninejad, Z. Qu, F. L. Lewis, and A. Davoudi. Optimal, nonlinear, and distributed designs of droop controls for dc microgrids. *IEEE Trans. Smart Grid.*, 5(5):2508–2516, Sep. 2014.

[45] M. B. Shadmand, R. S. Balog, and H. Abu-Rub. Model predictive control of pv sources in a smart dc distribution system: Maximum power point tracking and droop control. *IEEE Trans. Energy Convers.*, 29(4):913–921, Dec 2014.

[46] K. G. Vamvoudakis and J. P. Hespanha. Online optimal operation of parallel voltage-source inverters using partial information. *IEEE Trans. Ind. Electron.*, 64(5):4296–4305, May 2017.

[47] G. K. Venayagamoorthy, R. K. Sharma, P. K. Gautam, and A. Ahmadi. Dynamic energy management system for a smart microgrid. *IEEE Trans. Neural Netw. Learn. Syst.*, 27(8):1643–1656, Aug 2016.

[48] D. Wang, H. He, C. Mu, and D. Liu. Intelligent critic control with disturbance attenuation for affine dynamics including an application to a microgrid system. *IEEE Trans. Ind. Electron.*, 64(6):4935–4944, June 2017.

[49] J. Han, S. Khushalani-Solanki, J. Solanki, and J. Liang. Adaptive critic design-based dynamic stochastic optimal control design for a microgrid with multiple renewable resources. *IEEE Trans. Smart Grid.*, 6(6):2694–2703, Nov 2015.

[50] Q. Wei, D. Liu, F. L. Lewis, Y. Liu, and J. Zhang. Mixed iterative adaptive dynamic programming for optimal battery energy control in smart residential microgrids. *IEEE Trans. Ind. Electron.*, 64(5):4110–4120, May 2017.

[51] L. Fan, V. Nasirian, H. Modares, F. L. Lewis, Y. Song, and A. Davoudi. Game-theoretic control of active loads in dc microgrids. *IEEE Trans. Energy Convers.*, 31(3):882–895, Sep. 2016.

[52] Petros A Ioannou and Jing Sun. *Robust adaptive control*, volume 1. PTR Prentice-Hall Upper Saddle River, NJ, 1996.

[53] Frank L Lewis and Derong Liu. *Reinforcement learning and approximate dynamic programming for feedback control*, volume 17. John Wiley & Sons, 2013.

[54] Derong Liu, Qinglai Wei, Ding Wang, Xiong Yang, and Hongliang Li. *Adaptive dynamic programming with applications in optimal control*. Springer, 2017.

[55] Rushikesh Kamalapurkar, Patrick Walters, Joel Rosenfeld, and Warren Dixon. *Reinforcement Learning for Optimal Feedback Control: A Lyapunov-Based Approach*. Springer, 2018.

[56] Alexis Kwasinski and Chimaobi N Onwuchekwa. Dynamic behavior and stabilization of dc microgrids with instantaneous constant-power loads. *IEEE Trans. Power Electron.*, 26(3):822–834, 2011.

[57] Ali Emadi, Alireza Khaligh, Claudio H Rivetta, and Geoffrey A Williamson. Constant power loads and negative impedance instability in automotive systems: definition, modeling, stability, and control of power electronic converters and motor drives. *IEEE Trans. Veh. Technol.*, 55(4):1112–1125, 2006.

[58] Santiago Sanchez and Marta Molinas. Degree of influence of system states transition on the stability of a dc microgrid. *IEEE Trans. Smart Grid.*, 5(5):2535–2542, 2014.

[59] Mei Su, Zhangjie Liu, Yao Sun, Hua Han, and Xiaochao Hou. Stability analysis and stabilization methods of dc microgrid with multiple parallel-connected dc–dc converters loaded by cpls. *IEEE Trans. Smart Grid.*, 9(1):132–142, 2016.

[60] Claudio H Rivetta, Ali Emadi, Geoffrey A Williamson, Ranjit Jayabalan, and Babak Fahimi. Analysis and control of a buck dc-dc converter operating with constant power load in sea and undersea vehicles. *IEEE Trans. Ind. Appl.*, 42(2):559–572, 2006.

[61] Robert S Balog, Wayne W Weaver, and Philip T Krein. The load as an energy asset in a distributed architecture. In *IEEE Electric Ship Technologies Symposium*, volume 1, pages 261–267, 2005.

[62] Pisit Liutanakul, Ahmed-Bilal Awan, Serge Pierfederici, Babak Nahid-Mobarakeh, and Farid Meibody-Tabar. Linear stabilization of a dc bus supplying a constant power load: A general design approach. *IEEE Trans. Power Electron.*, 25(2):475–488, 2010.

[63] Chimaobi N Onwuchekwa and Alexis Kwasinski. Analysis of boundary control for buck converters with instantaneous constant-power loads. *IEEE Trans. Power Electron.*, 25(8):2018–2032, 2010.

[64] Luis Benadero, Rony Cristiano, Daniel J Pagano, and Enrique Ponce. Nonlinear analysis of interconnected power converters: A case study. 5(3):326–335, 2015.

[65] Yue Zhao, Wei Qiao, and Daihyun Ha. A sliding-mode duty-ratio controller for dc/dc buck converters with constant power loads. *IEEE Trans. Ind. Appl.*, 50(2):1448–1458, 2013.

[66] Daniel Logue and Philip T Krein. The power buffer concept for utility load decoupling. In *2000 IEEE 31st Annual Power Electronics Specialists Conference. Conference Proceedings (Cat. No. 00CH37018)*, volume 2, pages 973–978. IEEE, 2000.

[67] Wayne W Weaver and Philip T Krein. Optimal geometric control of power buffers. *IEEE Trans. Power Electron.*, 24(5):1248–1258, 2009.

[68] Vahidreza Nasirian, Ajay Pratap Yadav, Frank L Lewis, and Ali Davoudi. Distributed assistive control of power buffers in dc microgrids. *IEEE Trans. Energy Convers.*, 32(4):1396–1406, 2017.

[69] Bibaswan Banerjee and Wayne W Weaver. Generalized geometric control manifolds of power converters in a dc microgrid. *IEEE Trans. Energy Convers.*, 29(4):904–912, 2014.

[70] Josep M Guerrero, L Garcia De Vicuna, José Matas, Miguel Castilla, and Jaume Miret. A wireless controller to enhance dynamic performance of parallel inverters in distributed generation systems. *IEEE Trans. Power Electron.*, 19(5):1205–1213, 2004.

[71] Yajuan Guan, Josep M Guerrero, Xin Zhao, Juan C Vasquez, and Xiaoqiang Guo. A new way of controlling parallel-connected inverters by using synchronous-reference-frame virtual impedance loop—part i: Control principle. *IEEE Trans. Power Electron.*, 31(6):4576–4593, 2016.

[72] Kalyanmoy Deb, Amrit Pratap, Sameer Agarwal, and TAMT Meyarivan. A fast and elitist multiobjective genetic algorithm: Nsga-ii. *IEEE Trans. Evol. Comput.*, 6(2):182–197, 2002.

[73] Gregory M Vosters and Wayne W Weaver. Energy and impedance space modeling of power electronic converters. In *2011 IEEE Energy Conversion Congress and Exposition*, pages 1265–1272. IEEE, 2011.

[74] Michael Angelo Pedrasa and Ted Spooner. A survey of techniques used to control microgrid generation and storage during island operation. In *Proceedings of the 2006 Australasian Universities Power Engineering Conference (AUPEC'06)*, pages 1–6, 2006.

[75] Ali Bidram and Ali Davoudi. Hierarchical structure of microgrids control system. *IEEE Trans. Smart Grid.*, 3(4):1963–1976, 2012.

[76] CN Papadimitriou, EI Zountouridou, and ND Hatziargyriou. Review of hierarchical control in dc microgrids. *Electric Power Systems Research*, 122:159–167, 2015.

[77] M. M. A. Abdelaziz, M. F. Shaaban, H. E. Farag, and E. F. El-Saadany. A multistage centralized control scheme for islanded microgrids with pevs. *IEEE Trans. Sustain. Energy*, 5(3):927–937, July 2014.

[78] Gang Yao, Yu Lu, Tianhao Tang, Mohamed Benbouzid, Yukai Zheng, and Tianzhen Wang. A central control strategy of parallel inverters in ac microgrid. In *IECON 2013-39th Annual Conference of the IEEE Industrial Electronics Society*, pages 7112–7117. IEEE, 2013.

[79] N. L. Díaz, A. C. Luna, J. C. Vasquez, and J. M. Guerrero. Centralized control architecture for coordination of distributed renewable generation and energy storage in islanded ac microgrids. *IEEE Trans. Power Electron.*, 32(7):5202–5213, July 2017.

[80] KT Tan, XY Peng, Ping Lam So, Yun Chung Chu, and MZQ Chen. Centralized control for parallel operation of distributed generation inverters in microgrids. *IEEE Trans. Smart Grid.*, 3(4):1977–1987, 2012.

[81] M Karimi, P Wall, H Mokhlis, and V Terzija. A new centralized adaptive underfrequency load shedding controller for microgrids based on a distribution state estimator. *IEEE Trans. Power Del.*, 32(1):370–380, 2017.

[82] Amir Khorsandi, Mojtaba Ashourloo, and Hossein Mokhtari. A decentralized control method for a low-voltage dc microgrid. *IEEE Trans. Energy Convers.*, 29(4):793–801, 2014.

[83] Saeed Peyghami, Hossein Mokhtari, and Frede Blaabjerg. Decentralized load sharing in a low-voltage direct current microgrid with an adaptive droop approach based on a superimposed frequency. *IEEE J. Emerging Sel. Topics Power Electron.*, 5(3):1205–1215, 2017.

[84] Wei Gu, Guannan Lou, Wen Tan, and Xiaodong Yuan. A nonlinear state estimator-based decentralized secondary voltage control scheme for autonomous microgrids. *IEEE Trans. Power Syst.*, 32(6):4794–4804, 2017.

[85] Jie Yang, Xinmin Jin, Xuezhi Wu, Pablo Acuna, Ricardo P Aguilera, Thomas Morstyn, and Vassilios G Agelidis. Decentralised control method for dc microgrids with improved current sharing accuracy. *IET Generation, Transmission & Distribution*, 11(3):696–706, 2017.

[86] Yasser Abdel-Rady Ibrahim Mohamed and Ehab F El-Saadany. Adaptive decentralized droop controller to preserve power sharing stability of paralleled inverters in distributed generation microgrids. *IEEE Transactions on Power Electronics*, 23(6):2806–2816, 2008.

[87] Vito Calderaro, Gaspare Conio, Vincenzo Galdi, Giovanni Massa, and Antonio Piccolo. Optimal decentralized voltage control for distribution systems with inverter-based distributed generators. *IEEE Transactions on Power Systems*, 29(1):230–241, 2014.

[88] V. Nasirian, Q. Shafiee, J. M. Guerrero, F. L. Lewis, and A. Davoudi. Droop-free distributed control for ac microgrids. *IEEE Trans. Power Electron.*, 31(2):1600–1617, Feb 2016.

[89] Jingang Lai, Hong Zhou, Xiaoqing Lu, Xinghuo Yu, and Wenshan Hu. Droop-based distributed cooperative control for microgrids with time-varying delays. *IEEE Trans. Smart Grid.*, 7(4):1775–1789, 2016.

[90] Wayne W Weaver, Rush D Robinett III, Gordon G Parker, and David G Wilson. Distributed control and energy storage requirements of networked dc microgrids. *Control Engineering Practice*, 44:10–19, 2015.

[91] Nima Mahdian Dehkordi, Nasser Sadati, and Mohsen Hamzeh. Distributed robust finite-time secondary voltage and frequency control of islanded microgrids. *IEEE Trans. Power Syst.*, 32(5):3648–3659, 2017.

[92] Kwang Y Lee and Mohamed A El-Sharkawi. *Modern heuristic optimization techniques: theory and applications to power systems*, volume 39. John Wiley & Sons, 2008.

[93] Mohammad Ali Abido. Multiobjective evolutionary algorithms for electric power dispatch problem. *IEEE Trans. Evol. Comput.*, 10(3):315–329, 2006.

[94] J Hazra and AK Sinha. A multi-objective optimal power flow using particle swarm optimization. *International Transactions on Electrical Energy Systems*, 21(1):1028–1045, 2011.

[95] MA Abido and NA Al-Ali. Multi-objective optimal power flow using differential evolution. *Arabian Journal for Science and Engineering*, 37(4):991–1005, 2012.

[96] M Varadarajan and K Shanty Swarup. Solving multi-objective optimal power flow using differential evolution. *IET Generation, Transmission & Distribution*, 2(5):720–730, 2008.

[97] T Niknam, MR Narimani, J Aghaei, and R Azizipanah-Abarghooee. Improved particle swarm optimisation for multi-objective optimal power flow considering the cost, loss, emission and voltage stability index. *IET generation, transmission & distribution*, 6(6):515–527, 2012.

[98] Mohammad H Moradi, Mohamad Abedini, and S Mahdi Hosseinian. A combination of evolutionary algorithm and game theory for optimal location and operation of dg from dg owner standpoints. *IEEE Trans. Smart Grid.*, 7(2):608–616, 2016.

[99] Hossein Farzin, Mahmud Fotuhi-Firuzabad, and Moein Moeini-Aghtaie. A stochastic multi-objective framework for optimal scheduling of energy storage systems in microgrids. *IEEE Trans. Smart Grid.*, 8(1):117–127, 2017.

[100] Mohammad B Shadmand and Robert S Balog. Multi-objective optimization and design of photovoltaic-wind hybrid system for community smart dc microgrid. *IEEE Trans. Smart Grid.*, 5(5):2635–2643, 2014.

[101] WANG Panbao, WANG Wei, MENG Nina, and XU Dianguo. Multi-objective energy management system for dc microgrids based on the maximum membership degree principle. *Journal of Modern Power Systems and Clean Energy*, pages 1–11, 2017.

[102] Peng Li, Duo Xu, Zeyuan Zhou, Wei-Jen Lee, and Bo Zhao. Stochastic optimal operation of microgrid based on chaotic binary particle swarm optimization. *IEEE Trans. Smart Grid.*, 7(1):66–73, 2016.

[103] Morad Mohamed Abdelmageed Abdelaziz, Hany E Farag, and Ehab F El-Saadany. Optimum reconfiguration of droop-controlled islanded microgrids. *IEEE Trans. Power Syst.*, 31(3):2144–2153, 2016.

[104] J Jithendranath and Debapriya Das. Scenario-based multi-objective optimisation with loadability in islanded microgrids considering load and renewable generation uncertainties. *IET Renewable Power Generation*, 2019.

[105] Zehuai Liu, Jiahao Yang, Yongjun Zhang, Tianyao Ji, Junhuang Zhou, and Zexiang Cai. Multi-objective coordinated planning of active-reactive power resources for decentralized droop-controlled islanded microgrids based on probabilistic load flow. *IEEE Access*, 6:40267–40280, 2018.

[106] Avirup Maulik and Debapriya Das. Optimal power dispatch considering load and renewable generation uncertainties in an ac-dc hybrid microgrid. *IET Generation, Transmission & Distribution*, 2019.

[107] Christian Blum and Xiaodong Li. Swarm intelligence in optimization. In *Swarm Intelligence*, pages 43–85. Springer, 2008.

[108] Kaisa Miettinen. *Nonlinear multiobjective optimization*, volume 12. Springer Science & Business Media, 2012.

[109] J David Schaffer. Multiple objective optimization with vector evaluated genetic algorithms. In *Proceedings of the First International Conference on Genetic Algorithms and Their Applications, 1985*. Lawrence Erlbaum Associates. Inc., Publishers, 1985.

[110] Prabhat Hajela, E Lee, and C-Y Lin. Genetic algorithms in structural topology optimization. In *Topology design of structures*, pages 117–133. Springer, 1993.

[111] Tadahiko Murata and Hisao Ishibuchi. Moga: Multi-objective genetic algorithms. In *IEEE international conference on evolutionary computation*, volume 1, pages 289–294, 1995.

[112] Carlos M Fonseca, Peter J Fleming, et al. Genetic algorithms for multiobjective optimization: Formulationdiscussion and generalization. In *Icga*, volume 93, pages 416–423. Citeseer, 1993.

[113] Nidamarthi Srinivas and Kalyanmoy Deb. Muiltiobjective optimization using nondominated sorting in genetic algorithms. *Evolutionary computation*, 2(3):221–248, 1994.

[114] Je rey Horn, Nicholas Nafpliotis, and David E Goldberg. A niched pareto genetic algorithm for multiobjective optimization. In *Proceedings of the first IEEE conference on evolutionary computation, IEEE world congress on computational intelligence*, volume 1, pages 82–87. Citeseer, 1994.

[115] Andrzej Osyczka and Sourav Kundu. A new method to solve generalized multicriteria optimization problems using the simple genetic algorithm. *Structural optimization*, 10(2):94–99, 1995.

[116] Eckart Zitzler and Lothar Thiele. An evolutionary algorithm for multiobjective optimization: The strength pareto approach. *TIK-report*, 43, 1998.

[117] Kalyanmoy Deb et al. Evolutionary algorithms for multi-criterion optimization in engineering design. *Evolutionary algorithms in engineering and computer science*, 2:135–161, 1999.

[118] Fernando Jiménez, José L Verdegay, et al. Evolutionary techniques for constrained multiobjective optimization problems. 1999.

[119] Yonas Gebre Woldesenbet, Gary G Yen, and Biruk G Tessema. Constraint handling in multiobjective evolutionary optimization. *IEEE Trans. Evol. Comput.*, 13(3):514–525, 2009.

[120] T Ray, K Tai, and C Seow. An evolutionary algorithm for multiobjective optimization. *Eng. Optim*, 33(3):399–424, 2001.

[121] Quanyuan Jiang, Meidong Xue, and Guangchao Geng. Energy management of microgrid in grid-connected and stand-alone modes. *IEEE Trans. Power Syst.*, 28(3):3380–3389, 2013.

[122] Nimish Soni, Suryanarayana Doolla, and Mukul C Chandorkar. Improvement of transient response in microgrids using virtual inertia. *IEEE transactions on power delivery*, 28(3):1830–1838, 2013.

[123] Augustine M Egwebe, Meghdad Fazeli, Petar Igic, and Paul M Holland. Implementation and stability study of dynamic droop in islanded microgrids. *IEEE Transactions on energy conversion*, 31(3):821–832, 2016.

[124] Hongtao Shi, Fang Zhuo, Hao Yi, Feng Wang, Dong Zhang, and Zhiqing Geng. A novel real-time voltage and frequency compensation strategy for photovoltaic-based microgrid. *IEEE Transactions on Industrial Electronics*, 62(6):3545–3556, 2015.

[125] Xiao Sun, Lik-Kin Wong, Yim-Shu Lee, and Dehong Xu. Design and analysis of an optimal controller for parallel multi-inverter systems. *IEEE Transactions on Circuits and Systems II: Express Briefs*, 53(1):56–61, 2006.

[126] RB Godoy, CA Canesin, and JOP Pinto. Optimized dynamic response of parallel operation of two single phase inverters based on evolutionary theory. In *SPEEDAM 2010*, pages 1135–1140. IEEE, 2010.

[127] Mahdi Kohansal, Javad S Moghani, Matin Rahmatian, and Gevorg B Gharehpetian. Multi-objective optimization to improve transient performance of vsi in an off-grid micro-gird using imperialist competitive algorithm. In *The 2nd International Conference on Control, Instrumentation and Automation*, pages 536–541. IEEE, 2011.

[128] Donald E Kirk. *Optimal control theory: an introduction*. Dover, 2004.

[129] Frank L Lewis, Hongwei Zhang, Kristian Hengster-Movric, and Abhijit Das. *Cooperative control of multi-agent systems: optimal and adaptive design approaches*. Springer Science & Business Media, 2013.

[130] Guillermo Owen. *Game Theory*. Emerald Group Publishing Limited, 2013.

[131] Tamer Basar and Geert Jan Olsder. *Dynamic noncooperative game theory*, volume 23. Siam, 1999.

[132] Zubair Md Fadlullah, Yousuke Nozaki, Akira Takeuchi, and Nei Kato. A survey of game theoretic approaches in smart grid. In *2011 International Conference on Wireless Communications and Signal Processing (WCSP)*, pages 1–4. IEEE, 2011.

[133] Hamidreza Nazaripouya and Shahab Mehraeen. Modeling and nonlinear optimal control of weak/islanded grids using facts device in a game theoretic approach. *IEEE Transactions on Control Systems Technology*, 24(1):158–171, 2016.

[134] Quanyan Zhu, Jiangmeng Zhang, Peter W Sauer, Alejandro Domínguez-García, and Tamer Başar. A game-theoretic framework for control of distributed renewable-based energy resources in smart grids. In *2012 American Control Conference (ACC)*, pages 3623–3628. IEEE, 2012.

[135] Haoyong Chen, Rong Ye, Xiaodong Wang, and Runge Lu. Cooperative control of power system load and frequency by using differential games. *IEEE Transactions on Control Systems Technology*, 23(3):882–897, 2015.

[136] Pirathayini Srikantha and Deepa Kundur. A game theoretic approach to real-time robust distributed generation dispatch. *IEEE Transactions on Industrial Informatics*, 13(3):1006–1016, 2017.

[137] Eduardo Mojica-Nava, Carlos Andrés Macana, and Nicanor Quijano. Dynamic population games for optimal dispatch on hierarchical microgrid control. *IEEE Transactions on Systems, Man, and Cybernetics: Systems*, 44(3):306–317, 2014.

[138] Amir-Hamed Mohsenian-Rad, Vincent WS Wong, Juri Jatskevich, Robert Schober, and Alberto Leon-Garcia. Autonomous demand-side management based on game-theoretic energy consumption scheduling for the future smart grid. *IEEE transactions on Smart Grid*, 1(3):320–331, 2010.

[139] Frank L Lewis and Draguna Vrabie. Reinforcement learning and adaptive dynamic programming for feedback control. *IEEE Circuits Syst. Mag.*, 9(3), 2009.

[140] Patryk Deptula, Joel A Rosenfeld, Rushikesh Kamalapurkar, and Warren E Dixon. Approximate dynamic programming: Combining regional and local state following approximations. *IEEE Trans. Neural Netw. Learn. Syst.*, 29(6):2154–2166, 2018.

[141] Christian Kirches. The direct multiple shooting method for optimal control. In *Fast Numerical Methods for Mixed-integer Nonlinear Model-Predictive control*, pages 13–29. Springer, 2011.

[142] Charles R Hargraves and Stephen W Paris. Direct trajectory optimization using nonlinear programming and collocation. *Journal of Guidance, Control, and Dynamics*, 10(4):338–342, 1987.

[143] VR Anil, AB David, D Christopher, et al. Gpops, a matlab software for solving multiple-phase optimal control problems using the gauss pseudospectral method. *ACM T Math Software*, 37:22–39, 2010.

[144] Frank L Lewis, Draguna Vrabie, and Vassilis L Syrmos. *Optimal control*. John Wiley & Sons, 2012.

[145] Miroslav Krstic and Zhong-Hua Li. Inverse optimal design of input-to-state stabilizing nonlinear controllers. *IEEE Trans. Autom. Control*, 43(3):336–350, 1998.

[146] Wencheng Luo, Yun-Chung Chu, and Keck-Voon Ling. Inverse optimal adaptive control for attitude tracking of spacecraft. *IEEE Transactions on Automatic Control*, 50(11):1639–1654, 2005.

[147] Ali Bidram, Vahidreza Nasirian, Ali Davoudi, and Frank L Lewis. *Cooperative synchronization in distributed microgrid control*, pages 211–235. Springer, 2017.

[148] Anushka M Dissanayake and Nishantha C Ekneligoda. Multi-objective optimization of droop controlled distributed generators in dc microgrids. *IEEE Trans. Ind. Informat.*, 16(4):2423–2435, 2020.

[149] Andre Pires Nobrega Tahim, Daniel J Pagano, Eduardo Lenz, and Vinicius Stramosk. Modeling and stability analysis of islanded dc microgrids under droop control. *IEEE Trans. Power Electron.*, 30(8):4597–4607, 2015.

[150] Dragutin Ščap, Matija Hoić, and Andrej Jokić. Determination of the pareto frontier for multiobjective optimization problem. *Transactions of FAMENA*, 37(2):15–28, 2013.

[151] Martin T Hagan, Howard B Demuth, Mark H Beale, and Orlando De Jesús. *Neural network design*, volume 20. Pws Pub. Boston, 1996.

[152] M Varadarajan and K Shanty Swarup. Solving multi-objective optimal power flow using differential evolution. *IET Generation, Transmission & Distribution*, 2(5):720–730, 2008.

[153] Hebertt J Sira-Ramirez and Ramón Silva-Ortigoza. *Control design techniques in power electronics devices*. Springer Science & Business Media, 2006.

[154] Caisheng Wang and M Hashem Nehrir. Analytical approaches for optimal placement of distributed generation sources in power systems. *IEEE Trans. Power Syst.*, 19(4):2068–2076, 2004.

[155] Fengji Luo, Yingying Chen, Zhao Xu, Gaoqi Liang, Yu Zheng, and Jing Qiu. Multiagent-based cooperative control framework for microgrids' energy imbalance. *IEEE Trans. Ind. Informat.*, 13(3):1046–1056, 2017.

[156] Anushka M Dissanayake and Nishantha C Ekneligoda. Droop free optimal feedback control of distributed generators in islanded dc microgrids. *IEEE J. Emerging Sel. Topics Power Electron.*, 2019.

[157] Murad Abu-Khalaf and Frank L Lewis. Nearly optimal control laws for nonlinear systems with saturating actuators using a neural network hjb approach. *Automatica*, 41(5):779–791, 2005.

[158] H. Modares, F. L. Lewis, and M. Naghibi-Sistani. Adaptive optimal control of unknown constrained-input systems using policy iteration and neural networks. *IEEE Trans. Neural Netw. Learn. Syst.*, 24(10):1513–1525, Oct 2013.

[159] FW Lewis, Suresh Jagannathan, and A Yesildirak. *Neural network control of robot manipulators and non-linear systems*. CRC Press, 1998.

[160] Richard S Sutton and Andrew G Barto. *Reinforcement learning: An introduction*. MIT press, 2018.

[161] Girish Chowdhary and Eric Johnson. Concurrent learning for convergence in adaptive control without persistency of excitation. In *Decision and Control (CDC), 2010 49th IEEE Conference on*, pages 3674–3679. IEEE, 2010.

[162] Kyriakos Vamvoudakis and Sarangapani Jagannathan. *Control of Complex Systems: Theory and Applications*. Butterworth-Heinemann, 2016.

[163] Hassan K Khalil and JW Grizzle. *Nonlinear systems*, volume 3. Prentice hall Upper Saddle River, NJ, 2002.

[164] Prabha Kundur, Neal J Balu, and Mark G Lauby. *Power system stability and control*, volume 7. McGraw-hill New York, 1994.

[165] Kyriakos G Vamvoudakis and Frank L Lewis. Online actor–critic algorithm to solve the continuous-time infinite horizon optimal control problem. *Automatica*, 46(5):878–888, 2010.

[166] Paul Krause, Oleg Wasynczuk, Scott D Sudhoff, and Steven Pekarek. *Analysis of electric machinery and drive systems*, volume 75. John Wiley & Sons, 2013.

[167] Hans P Geering. *Optimal control with engineering applications*. Springer, 2007.

[168] Daniel Liberzon. *Calculus of variations and optimal control theory: a concise introduction*. Princeton University Press, 2011.

[169] Faisal Mumtaz, MH Syed, Mohamed Al Hosani, and HH Zeineldin. A novel approach to solve power flow for islanded microgrids using modified newton raphson with droop control of dg. *IEEE transactions on sustainable energy*, 7(2):493–503, 2016.

[170] Morad Mohamed Abdelmageed Abdelaziz, Hany E Farag, Ehab F El-Saadany, and Yasser Abdel-Rady I Mohamed. A novel and generalized three-phase power flow algorithm for islanded microgrids using a newton trust region method. *IEEE Transactions on Power Systems*, 28(1):190–201, 2013.

[171] Lawrence F Shampine, Jacek Kierzenka, and Mark W Reichelt. Solving boundary value problems for ordinary differential equations in matlab with bvp4c. *Tutorial notes*, 2000:1–27, 2000.

[172] Amirnaser Yazdani and Reza Iravani. *Voltage-sourced converters in power systems: modeling, control, and applications*. John Wiley & Sons, 2010.

VITA

Anushka Madushan Dissanayake Ralalage

Candidate for the Degree of

Doctor of Philosophy

Dissertation: OPTIMAL ENERGY MANAGEMENT AND CONTROL OF MICRO-GRIDS IN MODERN ELECTRICAL POWER SYSTEMS

Major Field: Electrical Engineering

Biographical:

Education:

Completed the requirements for the Doctor of Philosophy in Electrical Engineering at Oklahoma State University, Stillwater, Oklahoma in May, 2020.

Completed the requirements for the Bachelor of Science in Electrical and Electronic Engineering at University of Peradeniya, Peradeniya, Sri Lanka in 2014.

Experience:

Employed by Oklahoma State Univeristy in the position of Research and Teaching Assistant in Stillwater, Oklahoma from August 2015 to May 2020.

Employed by Univeristy of Peradeniya in the position of Engineering Lab Instructor in Peradeniya, Sri Lanka from October 2014 to July 2015.

Professional Memberships:

Student Member of IEEE as of 2018.